

Light Pulse Atom Interferometry at Short Interrogation Times for Inertial Navigation

by

David L. Butts

S.M., Massachusetts Institute of Technology (2008)

B.A., Williams College (2006)

Submitted to the Department of Aeronautics and Astronautics

in partial fulfillment of the requirements for the degree of
Doctor of Philosophy in Aeronautics and Astronautics

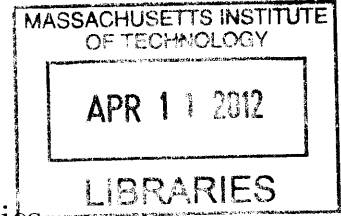
at the

MASSACHUSETTS INSTITUTE OF TECHNOLOGY

February 2012

© David L. Butts, 2011. All rights reserved.

The author hereby grants to MIT and Draper Laboratory permission to reproduce and distribute publicly paper and electronic copies of this thesis document in whole or in part.



ARCHIVES

Author

Department of Aeronautics and Astronautics

December 20, 2011

Certified by

Dr. Richard Stoner

Principal Member of the Technical Staff, C.S. Draper Laboratory

Thesis Supervisor

Certified by

Prof. Shaoul Ezekiel

Professor of Aeronautics & Astronautics and
Electrical Engineering and Computer Science

Thesis Supervisor

Certified by

Prof. Wolfgang Ketterle

John D. MacArthur Professor of Physics

Thesis Supervisor

Accepted by

Prof. Eytan H. Modiano

Professor of Aeronautics & Astronautics

Chair, Graduate Program Committee

Light Pulse Atom Interferometry at Short Interrogation Times for Inertial Navigation

by

David L. Butts

Submitted to the Department of Aeronautics and Astronautics
on December 20, 2011, in partial fulfillment of the
requirements for the degree of
Doctor of Philosophy in Aeronautics and Astronautics

Abstract

Light pulse atom interferometry with cold atoms is a promising inertial sensing technology for high accuracy navigation. At present, laboratory atom interferometers match or surpass state of the art mechanical and optical inertial sensors in terms of sensitivity and long term stability. Conventional laboratory systems, however, do not achieve sufficient bandwidth or dynamic range to operate in a dynamic environment; furthermore, the size, weight and power of laboratory sensors are unsuitable for many applications. In this thesis, atom interferometry is realized at shorter interrogation times (<15 ms as opposed to >100 ms), in which the required sensitivity, bandwidth and dynamic range of navigation systems becomes feasible. A cold atom gravimeter testbed using atom interferometry with stimulated Raman transitions was developed, which executed the entire measurement cycle in a compact vacuum cell (≈ 80 cc). The system demonstrated an inferred sensitivity of $2 \mu g/\sqrt{\text{Hz}}$ for an interrogation time of $2T = 10$ ms (based on measured phase SNR, scale factor, and repetition rate). With realistic improvements to the apparatus, it could achieve a sensitivity of $<1 \mu g/\sqrt{\text{Hz}}$, advancing toward the realization of a compact, atom-based inertial measurement unit with unprecedented performance. In addition, a method for increasing the momentum splitting of Raman pulse interferometers with sequential Raman pulses was demonstrated, and interferometer area was increased by up to a factor of nine without altering the interrogation time (corresponding to a momentum splitting of $18\hbar k$, the largest reported for Raman pulse interferometry). Composite Raman pulses were implemented to improve population transfer efficiency, which limits the achievable increase in precision. Finally, the effect of coherent population trapping (CPT) induced by Raman pulse atom optics was identified as a source of systematic phase shifts in the $\pi/2 - \pi - \pi/2$ interferometer used for sensing acceleration and rotation. CPT effects were modeled in a three-level (Λ) atom, and were experimentally characterized using atom interferometry. Based on the magnitude of measured coherences induced by Raman pulse atom optics, phase shifts of several milliradians should occur for a typical GHz-scale laser detuning. A method for suppressing this bias in realistic operation by Raman beam propagation direction reversal is proposed.

Thesis Supervisor: Dr. Richard Stoner

Title: Principal Member of the Technical Staff, C.S. Draper Laboratory

Thesis Supervisor: Prof. Shaoul Ezekiel
Title: Professor of Aeronautics & Astronautics and
Electrical Engineering and Computer Science

Thesis Supervisor: Prof. Wolfgang Ketterle
Title: John D. MacArthur Professor of Physics

Acknowledgments

I am grateful to the cold atom sensing and electro-optics group at the Draper Laboratory for mentoring me during my graduate school career. Most of all, I am indebted to Rick Stoner, who advised me as a Draper fellow throughout all of my graduate work and invested an enormous amount of time and effort to make my research a success. I learned so much from his deep knowledge of experimental physics and talent for problem-solving, and benefited from his sharing and supporting of my work at Draper. I am thankful for the guidance of Prof. Shaoul Ezekiel, who also advised my research during my time at MIT. His enthusiasm for the challenges of making precise measurements and for technical writing made a large impact on my work and my interest in sensors (I also appreciated the tough squash matches).

I was incredibly fortunate to work with a talented team in the cold atom inertial sensing lab, who contributed to my work in many ways and made the long hours in the lab a blast. Thanks to Brian Timmons, who started at Draper the same summer and basically taught me how to build cold atom experiments. Thanks to Joe Kinast for helping to engineer an apparatus with enough flexibility to support all of my thesis projects, and for providing valuable feedback on publications. Thanks to Krish Kotru for being an awesome lab/officemate, for enthusiastically helping with the experiments, and for continuing the work (as well as the occasional jam session). Thanks to Paul Jones, who helped me find my way around the lab when I was new to Draper, and provided great tunes for the long days in lab. I am also indebted to Nicole Byrne for her help in designing and rebuilding the system with the compact vacuum cell. Thanks to Dave Johnson, who joined the group late in my work, but made many helpful suggestions for my final experiments and this thesis. Throughout my program, many Draper staff persistently showed interest in my work, which was a major source of inspiration. I am grateful to Neil Barbour for answering my many random questions about inertial navigation, and what applications *really* demand of inertial sensors. Many thanks to Tony Radojevic, Steve Smith and Phil Keating for championing cold atom technology at Draper and abroad, and for bringing so many interested visitors to check out what we were up to in the lab.

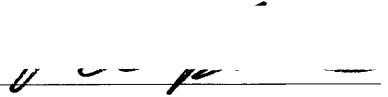
I am grateful for the opportunities and support provided by the Draper Laboratory during my graduate school career, especially through the Draper Laboratory Fellowship program. I greatly benefited from the flexibility and independence to pursue academic research, but

also from the opportunity to be exposed to the planning and management of real-world R&D programs. In addition to the financial support from the Education Office, the sincere encouragement and dedication of the Education Office staff, including George Schmidt, Linda Fuhrman, Stephan Kolitz, and Gail DiDonato, always made me feel welcome at Draper.

Finally, I am extremely thankful to have a supportive family and network of friends. Most of all, I am grateful for the love and support of my wife, Erika, who shared the journey of graduate school with me.

This thesis was prepared at the Charles Stark Draper Laboratory, Inc., under the Internal Research and Development Program. Project ID 26556 Activity ID 001.

Publication of this thesis does not constitute approval by Draper or the sponsoring agency of the findings or conclusions contained herein. It is published for the exchange and stimulation of ideas.

A handwritten signature in black ink, appearing to read 'David Butts', is written over a horizontal line.

David Butts

For Erika and my family.

Contents

1	Introduction	21
1.1	High Accuracy Inertial Navigation	21
1.2	Inertial Sensing with Atom Interferometry	25
1.3	Light Pulse Atom Interferometry	29
1.3.1	Cold Atoms	29
1.3.2	State of the Art Atom Interferometric Inertial Sensors	31
1.4	Practical Atom Interferometric Sensor Technology	33
1.4.1	Enhanced Sensitivity	35
1.4.2	Guided Atom Interferometry	36
1.4.3	Remaining Problems	37
1.5	Thesis Contributions	38
1.6	Thesis Outline	39
2	Atom Interferometer Theory	41
2.1	Stimulated Raman Transitions	41
2.1.1	Pseudospin Representation	45
2.2	Interferometer Theory	47
2.2.1	Interferometer Phase Shifts	48
2.2.2	Laser Interaction Phase Shifts	48
2.2.3	Free Propagation Phase	50
2.2.4	Separation Phase	51
2.2.5	Finite Pulse Duration Effects	52
2.3	Interferometer Frequency Response	53

3	Apparatus	55
3.1	Vacuum System	55
3.2	Magnetic Field Control	57
3.3	Optical System	58
3.3.1	Tapered Amplifiers	61
3.4	Control Electronics	63
3.5	Raman Beam Generation	65
3.5.1	Microwave Frequency Generation	68
4	Short Interrogation Time Atom Interferometry	71
4.1	Atom Trapping and State Preparation	71
4.2	Interferometry	73
4.3	State Detection	76
4.4	Gravity Measurement	78
4.4.1	Systematics	81
4.5	Raman Pulse Dephasing	84
4.6	Summary	87
5	Composite Raman Pulses and Large Area Atom Interferometry	89
5.1	Large Momentum Transfer with Raman Pulses	90
5.1.1	Composite Pulse Techniques	91
5.2	Composite Raman Pulses	95
5.2.1	Experiment	96
5.3	Large Area Atom Interferometry with Composite Raman Pulses	99
5.3.1	Experiment	101
5.4	Summary and Improvements	105
6	Coherent Population Trapping in Raman Pulse Atom Interferometry	107
6.1	Background	108
6.2	Raman Pulse Theory including Spontaneous Emission	111
6.3	Experiment	117
6.3.1	Doppler Insensitive Raman pulses	118

6.3.2	Doppler Sensitive Raman pulses	124
6.3.3	Impact of CPT on a $\pi/2 - \pi - \pi/2$ Interferometer, Summary	126
7	Conclusion	131
7.1	Future Steps	132
A	Cesium D2 Transition Data	135
B	Modeling of Large Area Atom Interferometry	137

THIS PAGE INTENTIONALLY LEFT BLANK

List of Figures

1-1	Mach-Zehnder light pulse atom interferometer	26
1-2	Acceleration measured by a three-pulse atom interferometer	28
1-3	Diagram of a magneto-optic trap	30
1-4	Examples of compact atom interferometers	34
2-1	Energy level diagram of a stimulated Raman transition	42
2-2	Bloch sphere representation of population transfer by a Raman pulse	46
2-3	Trajectory of interferometer paths for a gravimeter	48
2-4	Free propagation phase calculated by the Feynman path integral approach	50
2-5	Frequency response of the $\pi/2 - \pi - \pi/2$ interferometer to acceleration	54
3-1	Octagonal vacuum cell design and photograph of the finished cell.	56
3-2	Fast MOT coil shutoff circuit schematic	58
3-3	Atomic energy level diagram with trapping and detection optical frequencies	59
3-4	Diagram of optics for generating trapping, state preparation and detection light	60
3-5	Diagram of optics for state preparation	61
3-6	Diagram of optics for splitting the trapping, probe, and pushing beams	62
3-7	Design for the tapered amplifier modules.	62
3-8	Vacuum cell and optics mounting design.	64
3-9	Diagram of optics for Raman beam generation.	65
3-10	Phase modulation spectrum produced by the Raman EOM.	67
3-11	Diagram of microwave frequency generation for the Raman beams.	69
4-1	Drawing of vacuum cell and optical configuration for interferometry experiments	72
4-2	Interferometer pulse and laser frequency difference timing diagram	74

4-3	Raman detuning scan with $\approx 5 \mu\text{K}$ and $\approx 0.5 \mu\text{K}$ ensembles	75
4-4	Interference fringes for $T = 1 \text{ ms}$	75
4-5	Time series for determination of detection SNR	77
4-6	Allan deviation of an 11 hour gravity measurement	80
4-7	Allan deviation of gravity measurements at different interrogation times . . .	81
4-8	Transfer function of the three-pulse interferometer for laser phase noise . . .	82
4-9	Raman pulse dephasing due to the Gaussian laser beam profile	85
4-10	Diagram for the Raman pulse dephasing diagnostic ($n\pi_{0^\circ} - n\pi_{0^\circ/180^\circ}$)	86
4-11	Raman pulse dephasing measured by two-pulse ($n\pi_{0^\circ} - n\pi_{0^\circ/180^\circ}$) interferometers	87
5-1	Large momentum transfer with sequential Raman pulses	91
5-2	Large area Raman interferometer diagram	92
5-3	Bloch sphere evolution of a $\pi/2_{0^\circ} - \pi_{90^\circ} - \pi/2_{0^\circ}$ composite pulse in the presence of drive field inhomogeneities	94
5-4	Theoretical comparison of frequency responses of a π pulse and composite Raman pulses	94
5-5	Bloch sphere representation of population inversion by a $\pi/2_{0^\circ} - \pi_{180^\circ} - 3\pi/2_{0^\circ}$ composite pulse with large detuning	96
5-6	Measured detuning profiles of Doppler sensitive composite Raman pulses . . .	97
5-7	Detuning profiles of Doppler insensitive composite Raman pulses	99
5-8	Contrast versus N for large area interferometers using π pulses and composite pulses as augmentation pulses	102
5-9	Scale factor measurement for $6 - 14\hbar k$ ($N = 1 - 3$) large area atom interfer- ometers	103
5-10	Interference fringes for an $18\hbar k$ ($N = 4$) atom interferometer	103
5-11	Scale factor measurement for the $18\hbar k$ ($N = 4$) interferometer	104
6-1	Diagram of the three-level (Λ) atom and laser fields considered for coherent population trapping	109
6-2	Steady-state excited state population as a function of Raman detuning, ex- hibiting a CPT resonance	110

6-3	Bloch sphere representation of the experiment for measuring CPT effects induced by Doppler insensitive Raman pulses	118
6-4	Dark state population observed with Doppler insensitive $75\pi - \pi/2$ interferometers at positive and negative laser detuning	119
6-5	Dark state population induced by resonant, Doppler insensitive Raman pulses	120
6-6	Phase of dark state coherences induced by Doppler insensitive Raman pulses	121
6-7	Induced dark state population obtained with several Raman laser detunings	121
6-8	Off-resonant Raman pulse CPT experiment	123
6-9	Measurements of dark state population differences induced by off-resonant Raman pulses	124
6-10	Experimental sequence for measuring CPT effects induced by Doppler sensitive Raman pulses	125
6-11	Dark state population induced by Doppler sensitive Raman pulses	126
6-12	Contrast achieved with a Doppler sensitive (non-overlapping) $\pi/2 - \pi/2$ interferometer with and without velocity selection	127
6-13	Illustration of systematic phase shift induced by CPT in a $\pi/2 - \pi - \pi/2$ interferometer	128
B-1	Diagrammatic representation of the Raman pulse operator	138
B-2	Diagrammatic representation of probability amplitudes for a two-pulse sequence	139
B-3	Diagrammatic representation of probability amplitudes for a three-pulse sequence	140

THIS PAGE INTENTIONALLY LEFT BLANK

List of Tables

1.1	Characteristic performance metrics of inertial sensors in the highest performance class for flight navigation systems	23
5.1	Large area atom interferometer phase shifts induced by a constant acceleration	101
A.1	Relevant constants of ^{133}Cs and the D2 ($6^2S_{1/2} \rightarrow 6^2P_{3/2}$) transition	135

THIS PAGE INTENTIONALLY LEFT BLANK

Nomenclature

AOM Acousto-optic modulator

ASE Amplified spontaneous emission

AWG Arbitrary waveform generator

BEC Bose-Einstein condensate

CPT Coherent population trapping

EOM Electro-optic modulator

GPS Global Positioning System

IMU Inertial measurement unit

LIF Laser-induced fluorescence

LMT Large momentum transfer (atom optics)

MOT Magneto-optic trap

NMR Nuclear magnetic resonance

RF Radio frequency

SNR Signal-to-Noise Ratio

TA Tapered amplifier

THIS PAGE INTENTIONALLY LEFT BLANK

Chapter 1

Introduction

Inertial sensing technology plays a pivotal role in modern navigation and science. High performance inertial sensors enable technology such as self-contained, precise navigation systems, spacecraft that can survey the gravity field of a planet, or laboratory systems that test fundamental physical principles such as the universality of free fall. New sensing modalities, such as atom-based technology, are poised to revolutionize many of these engineering and scientific applications.

1.1 High Accuracy Inertial Navigation

Inertial sensors with high sensitivity and long term stability are critical for demanding navigation applications in which external references such as the Global Positioning System (GPS) are unavailable or may be unreliable. Typical inertial navigation applications include air and space flight, long duration submarine navigation, precise satellite pointing, and GPS-denied land navigation. In these circumstances, a suite of instruments measuring linear acceleration and rotation (accelerometers and gyroscopes) are of central importance in providing accurate position and heading estimates, and reducing the dependence on external aiding.

In an inertial navigation system, data from accelerometers and gyroscopes are integrated to estimate vehicle position over time—essentially a mechanized form of dead reckoning. However, sensor errors quickly integrate to large position errors. For example, an accelerometer with sensitivity σ_a (quoted as a velocity random walk, specified in units of $g/\sqrt{\text{Hz}}$) leads to a position error over duration T scaling as $\Delta x \simeq \sigma_a T^{3/2}$. A constant acceleration bias Δa

leads to a position error growing faster as $\Delta x \simeq \frac{1}{2}\Delta a T^2$. Likewise, angular rate errors from noise in gyroscopes (specified as angle random walk in units of deg/ $\sqrt{\text{hr}}$) or biases also leads to a rapidly accumulating position error. Other limiting error sources include initial alignment and uncertainty in compensation for local gravity, which individual accelerometers do not measure directly (accelerometers measure specific force, the difference between inertial and gravitational acceleration). While sophisticated gravity models mitigate this problem to some level, measurements of gravity gradients by onboard, high precision gradiometers may yet provide a more robust solution [1].

At present, the highest performance class of inertial navigation systems achieve position accuracy at the level of ~ 100 m/hr. Table 1.1 summarizes the approximate performance specifications for the individual sensors that would constitute the three-axis inertial measurement unit (IMU) in such a system. These performance levels are currently met by state of the art mechanical and optical inertial sensors. For accelerometers, the Pendulous Integrating Gyroscopic Accelerometer (PIGA) has demonstrated high sensitivity and linearity over a large dynamic range, making it suitable for a variety of flight applications. A PIGA senses acceleration by measuring displacements of a pendulous mass and rebalancing this motion with gyroscopic forces exerted by a separate rotating mass. These sensors, however, require inertially-stabilized platforms that are large, costly to manufacture, and have limited bandwidth (<30 Hz). Ultimately, the long term stability of mechanical sensors is limited by the precision of their machining, which can be prohibitively expensive and challenging to reproduce, and wear over the sensor lifetime. For gyroscopes, optical instruments such as the ring laser gyroscope and fiber optic gyroscope are beginning to replace their mechanical counterparts in some precision navigation systems. Optical gyroscopes measure rotation rate by the Sagnac effect, which introduces relative path differences between laser light traveling around counter-propagating paths on a rotating platform. These path differences are observable via power variations produced by interference of the laser beams at the interferometer loop output. Optical gyroscopes offer high sensitivity, large dynamic range, and compact, solid state design (no moving parts). For these reasons, they may be suitable for strapdown inertial systems (non-gimbaled) which require low noise, high bandwidth and high dynamic range sensors, but trade costly, complicated machining for increased computational complexity.

Table 1.1: Characteristic performance metrics of inertial sensors in the highest performance class for flight navigation systems [2].

Sensor Metrics	100 m/hr	5 m/hr (Future)
Accelerometer		
Sensitivity ($\mu g/\sqrt{\text{Hz}}$)	50	2
Bias stability (μg)	1	< 0.1
Scale factor stability (ppm)	1-10	<0.1
Gyroscope (strapdown)		
Sensitivity (mdeg/ $\sqrt{\text{hr}}$)	0.1	<0.05
Bias stability (mdeg/hr)	0.5	<0.02
Scale factor stability (ppm)	1-10	<0.1
Size, weight, and power		
Volume (cc)	100-600	Similar
Power (W)	5-35	Similar
Weight (g)	300-2200	Similar

Future high accuracy navigation applications, however, may demand inertial systems to achieve at or below 5 m/hr position drift. At this level of performance, a completely-inertial navigation system would approach GPS-levels of accuracy ($\approx 1 - 2$ meters) for missions under one hour in duration, allowing a vehicle to navigate without external aiding. As the sensor specifications in Table 1.1 indicate, however, this requires improvements in sensing performance of at least an order of magnitude. This increase in performance, particularly in bias stability and scale factor stability¹, has been difficult to achieve in ‘bulk media’ sensing technologies (e.g., MEMS).

Since the early 1990s, inertial sensing with atoms has proven a promising technology. The most successful atomic sensors use laser-cooled atoms as a proof mass, and precisely measure the motion of the atoms with atom interferometry. Atom interferometry exploits the wave properties of matter to make sensitive measurements of inertial forces, providing the exquisite accuracy possible with atomic measurements. Consider a comparison between optical and atom gyroscopes. As mentioned above, optical Sagnac gyroscopes measure rotation rate as a phase shift between two counter-propagating laser beams that enclose an area A :

$$\Delta\phi_{light} = \frac{4\pi\mathbf{\Omega} \cdot \mathbf{A}}{\lambda c} \quad (1.1)$$

¹Bias stability is a measure of the stability of the sensor output for zero input. Scale factor stability is a measure of the stability of the ratio of sensor output to input.

where Ω is the rotation rate, λ is the optical wavelength, and c is the speed of light. In an atom interferometer, matter waves are split and recombined in a similar geometry, resulting in a phase shift with a similar form,

$$\Delta\phi_{atom} = \frac{2m}{\hbar}\boldsymbol{\Omega} \cdot \mathbf{A}, \quad (1.2)$$

where m is the atomic mass and \hbar is the reduced Planck constant. The phase shift measured by the atom interferometer is larger by a factor of $mc^2/(\hbar\omega) \approx 10^{10}$ for the same enclosed area (interestingly, this is the ratio of the atom rest energy to the photon energy). While optical interferometers enclose more area than atom interferometers in practice, the expected sensitivity for an atom interferometer is still orders of magnitude better. At present, laboratory atom interferometers already compete with or surpass the sensitivity of state of the art sensors in each sensor class [3–6].

Atom-based sensors also offer several technological advantages. Like optical sensors, they have no moving parts and exploit major advances in laser, electro-optic, and vacuum technologies. Atoms also provide exceptional long term stability because they are ideal, inertially-free proof masses. Unlike proof masses in mechanical accelerometers, atoms in an interferometer are not directly coupled to the sensor case, which is typically a source of nonlinear response and drift. Moreover, all atoms in an ensemble are identical (of one species), and their physical properties are well-known and unchanging (as far as we know). As a sensing technology for navigation, atom interferometry is appealing because a single measurement technique provides both high precision acceleration and rotation rate, as well as other useful information like precise timekeeping. This fact has important implications for integrating sensors in an IMU, as well as simplifying the industrial base that would provide the sensors.

While the raw sensing capability demonstrated in laboratory systems underscores the potential for high accuracy, atom-based IMUs, these systems fall far short in other critical performance metrics—namely, dynamic range, bandwidth, and robustness to real-world environmental factors. Laboratory systems use large vacuum volumes, weigh tens to hundreds of kilograms and require hundreds or thousands of Watts to power lasers, electro-optic components, and radio-frequency (RF) electronics. Typical measurement cycles of >100 ms fall

short of the 100-500 Hz bandwidths demanded for many navigation systems, in addition to the difficulty in achieving continuous operation (during the dead time in which cold atom samples are prepared, there is no inertial sensitivity). Large scale factors (e.g., $> 10^5$ radians of phase per g of acceleration) pose a challenge for operation in a dynamic environment, where large changes in acceleration could result in errors due to the ambiguity of which interferometer fringe is registered. While early laboratory demonstrations were certainly not designed with the intention of serving such dynamic applications, the engineering challenges faced in transitioning atom interferometer technology from the laboratory to field-deployable platforms are clearly significant.

The following sections provide a more in-depth conceptual and historical background of inertial sensing with atom interferometry, and summarize important technological advancements relevant to the development of practical atomic inertial sensors. The chapter concludes with an outline of this thesis and a brief summary of the main contributions.

1.2 Inertial Sensing with Atom Interferometry

Before discussing state of the art in experimental atom interferometry, it is worthwhile to describe an atom interferometer at a basic level (the next chapter describes the theory of atom interferometry in more detail). In broad scope, atom interferometry is the coherent manipulation of an atom such that its quantum mechanical wavefunction is spatially split and recombined, creating interference between wavepackets that have accrued relative phase differences along their respective paths. These manipulations are implemented by atom optics, which are either laser light pulses or physical gratings that serve functions similar to optical beam splitters and mirrors [7]. In an interferometer, the atoms are deBroglie waves with a wavelength inversely proportional to their momentum ($\lambda_{dB} = h/p$). Interference is manifested in the distribution of atoms at the output ports of the interferometer. At present, light pulse atom optics have been most successful for making inertial measurements. Since light pulse atom interferometry is the subject of this thesis, the scope of the remaining discussion is restricted to this approach.

Fig. 1-1 depicts the simplest inertially-sensitive atom interferometer, a Mach-Zehnder interferometer. Initially, a sample of atoms in free space is prepared in one state, represented

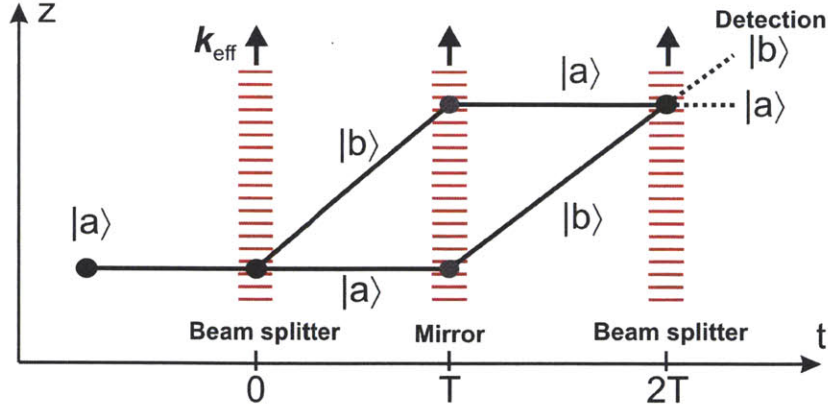


Figure 1-1: A Mach-Zehnder light pulse atom interferometer. \mathbf{k}_{eff} is the effective wavevector of the interferometer beams, which is proportional to the momentum transferred to the wavepackets by the light pulses, $\hbar\mathbf{k}_{\text{eff}}$. Interference produces a population difference between the output ports, corresponding to atoms in states $|a\rangle$ and $|b\rangle$.

by the notation $|a\rangle$, which includes both the internal state and external momentum state (for generality, it is denoted here by a single letter). A beam splitter pulse splits the wavepacket into a coherent superposition of two states, $|a\rangle$ and $|b\rangle$, typically with a two-photon transition that allows for long coherence times (e.g., a stimulated Raman transition). By energy conservation, the component of the wavefunction that makes a transition experiences a change in momentum $\hbar\mathbf{k}_{\text{eff}}$. The definition of the effective wavevector \mathbf{k}_{eff} of the interferometer beams depends on the particular transition driven by the light pulses. For instance, stimulated Raman transitions driven by two counter-propagating laser beams impart two photon recoils of momenta, $\hbar\mathbf{k}_{\text{eff}} \approx 2\hbar\mathbf{k}$, where k is the wavenumber of one laser beam (a more detailed description of Raman transitions is the subject of Chapter 2).

Following free propagation for a time T , the two wavepackets are deflected back toward each other by a ‘mirror’ pulse, which flips the state of each packet with certainty (from $|a\rangle$ to $|b\rangle$ or vice versa). When the wavepackets recombine at a time T later, a final beam splitter pulse mixes the wavepackets and creates interference. The relative phase of the two arms of the interferometer can be related to the relative populations of atoms in the two output ports of the interferometer, which respectively correspond to atoms in states $|a\rangle$ and $|b\rangle$. The population in $|b\rangle$ (the upper interferometer output port) is related to the interferometer phase $\Delta\phi$ by $P = \frac{1}{2} - \frac{1}{2} \cos \Delta\phi$.

Inertial sensitivity is introduced when the atoms are displaced relative to the inertial

reference (e.g., a mirror fixed to the vehicle platform) by inertial forces. The principle of the measurement is simple: acceleration can be determined by measuring the curvature of a particle's trajectory. With three position measurements, $\{z_i\}$, acquired at equal intervals in time, T , the average acceleration is

$$a = \frac{(z_3 - z_2) - (z_2 - z_1)}{T^2} \quad (1.3)$$

With a three pulse sequence like the one shown in Fig. 1-2, the local laser phases, $\phi_j = \mathbf{k}_{\text{eff}} \cdot \mathbf{z}_j - \omega_{\text{eff}} t + \phi_j^0$, sampled by the particle center of mass at each pulse encode this position information:

$$a = \frac{(\phi_3 - \phi_2) - (\phi_2 - \phi_1)}{k_{\text{eff}} T^2} = \frac{\phi_1 - 2\phi_2 + \phi_3}{k_{\text{eff}} T^2} = \frac{\Delta\phi}{k_{\text{eff}} T^2}, \quad (1.4)$$

for constant laser frequency and $\{\phi_j^0\}$. In this regard, it is illustrative to consider the optical phase fronts as a 'ruler' for the motion of the atom along the laser propagation axis, \mathbf{k}_{eff} . The Mach-Zehnder interferometer shown in Fig. 1-2(ii) measures acceleration along \mathbf{k}_{eff} through this differential phase shift, $\Delta\phi$, because the interaction of the atom with the light imprints the light phase on the wavefunction of the atom. The scale factor for the acceleration measurement is $|\mathbf{k}_{\text{eff}}|T^2$, meaning that precision can be improved by either increasing the interrogation time or transferring more momentum to the atoms with the atom optics. There is a clear trade between sensitivity and bandwidth; in other words, higher bandwidth sensors must resolve smaller displacements to achieve the same sensitivity.

By a similar argument, it can be shown that a rotation of the reference frame of the interferometer beams displaces the atoms by the Coriolis force. As mentioned above, the Sagnac phase shift measured by the three-pulse interferometer enclosing area A is

$$\Delta\phi_{gyro} = \frac{2m}{\hbar} \boldsymbol{\Omega} \cdot \mathbf{A} = -2\mathbf{k}_{\text{eff}} \cdot (\boldsymbol{\Omega} \times \mathbf{v}_0) T^2 \quad (1.5)$$

where \mathbf{v}_0 is the initial velocity of the atom. Therefore, the three-pulse interferometer provides acceleration and rotation rate measurements² [7]. A second interferometer is required, however, to discriminate between these quantities. Both the phase shifts in Eqs. (1.4) and

²This assumes zero linear acceleration. Chapter 2 discusses a higher-order phase shift coupling acceleration and rotation, with scaling $\sim (\boldsymbol{\Omega} \times \mathbf{a})T^3$.

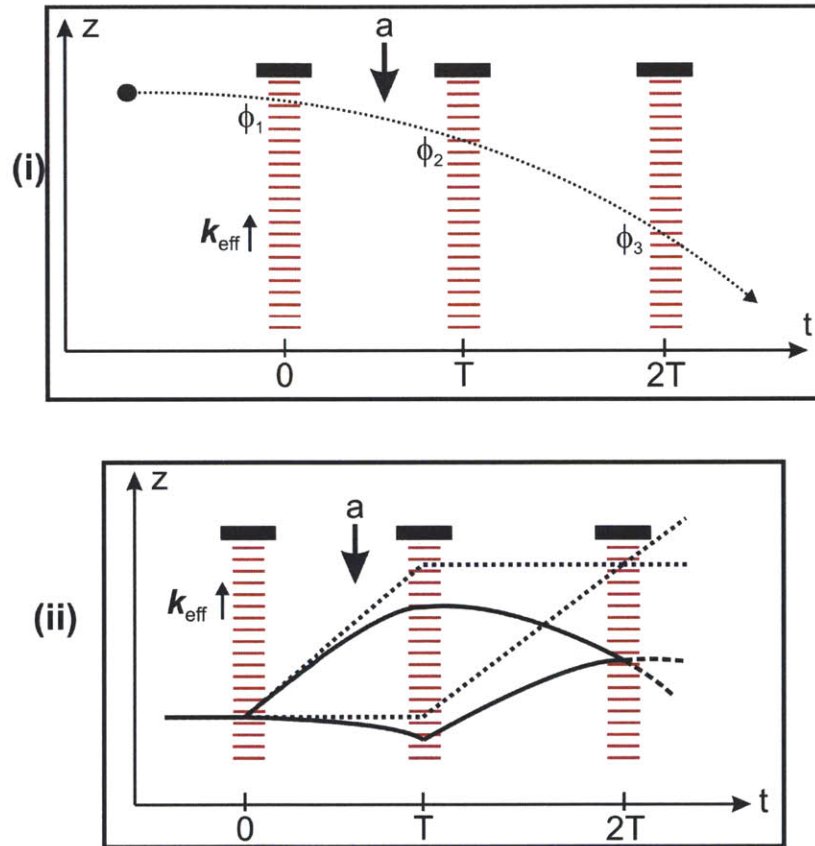


Figure 1-2: (i) Simple three-pulse acceleration measurement that measures the curvature of the particle's trajectory relative to the laser phase fronts (ϕ_1 , ϕ_2 , ϕ_3). (ii) The same interferometer shown in Fig. 1-1, but with atoms undergoing acceleration \mathbf{a} , as viewed in the laboratory frame. The phase difference measured at the output of this interferometer is proportional to \mathbf{a} , analogous to the simple scheme depicted in (i).

(1.5) state that the motion of the atom is measured on the scale of the wavelength of the interferometer beams, confirming the notion that the light pulses act as high resolution ‘rulers.’ The following sections review important developments in atom interferometry.

1.3 Light Pulse Atom Interferometry

The conceptual and experimental origins of light pulse atom interferometry can be traced back to seminal experiments by Rabi *et al.* [8] in atomic RF resonances, and Ramsey [9] in the method of separated oscillatory fields. Matter wave interference was first observed in 1975 with neutrons by Colella *et al.* [10]. In 1991, interference of neutral atoms was observed with very different approaches. Two experiments used nano-fabricated gratings as atom optics [11, 12]. Other successful techniques used momentum transfer from absorption and stimulated emission of photons, including stimulated Raman transitions in cesium [13] and an optical Ramsey excitation in calcium [14]³. Light pulse atom interferometry has been the most successful approach for inertial sensing because of the high achievable phase contrast and availability of longer interrogation times. Nevertheless, from the demonstration of the neutron interferometer onward, inertial sensing was recognized as a promising application of matter wave interferometry.

1.3.1 Cold Atoms

Cold atoms have become important tools in atomic physics for high precision spectroscopy, atom-based sensor technology, and quantum information science. At μK temperatures, an ensemble of atoms can be interrogated for >100 ms, availing very high precision in a variety of measurements including inertial sensors and clocks. In 1970, Ashkin demonstrated that laser light exerts a substantial scattering force, called radiation pressure, on microscopic particles and atoms [16, 17]. The basic principle of laser cooling is that atoms can be made to scatter photons with more energy than the incoming photon (at the laser frequency), and thereby transfer kinetic energy from the atom to the light field. Each scattering event imparts one photon recoil of momentum, $\hbar\mathbf{k}$, along the laser beam propagation direction, plus a momentum kick from the spontaneous emission of a photon in a random direction.

³A comprehensive review of atom interferometry is given by Berman (ed.) [15] and Cronin *et al.* [7].

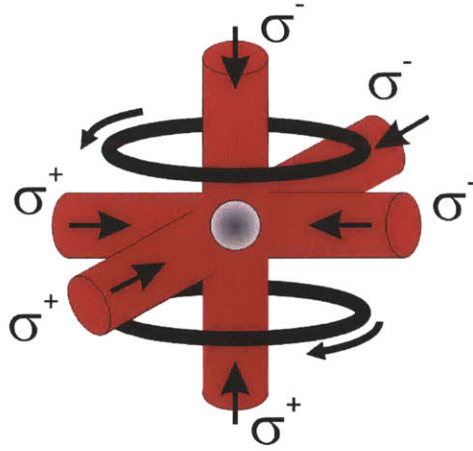


Figure 1-3: Diagram of a magneto-optic trap (MOT), with labeled light polarizations and magnetic coil current directions.

On average, scattering decelerates an atom moving towards the laser beam. Ashkin later proposed methods for trapping atoms in three dimensions with focused laser beams, which provide both a scattering force from radiation pressure and a transverse force from intensity gradients (analogous to the methods used to trap macroscopic dielectric spheres) [18]. The first three-dimensional cooling of an alkali vapor was reported in 1985 by Chu *et al.* [19], and is commonly known as ‘optical molasses.’

A major extension of this work was the development of the magneto-optic trap (MOT), in which a quadrupole magnetic field and three orthogonal pairs of off-resonant, circularly-polarized laser beams exert both a cooling, friction-like force and a position-dependent trapping force (see Fig. 1-3). The first MOT was demonstrated with sodium atoms by Raab *et al.* [20] in 1987, and has since become a ubiquitous tool for cold atom experiments. Typical MOTs trap $\sim 10^9$ atoms at μK temperatures in millimeter-scale clouds, and are robust to small beam misalignments and polarization errors. It was also noted in early trapping experiments that counter-propagating beams with crossed polarizations (e.g., $\sigma^+ - \sigma^-$) cooled atoms to temperatures far below the Doppler limit predicted for optical molasses [21]. The Doppler temperature is $T_D = \hbar\Gamma/2k_B$, for natural linewidth Γ and Boltzmann constant k_B (for cesium, the atom used in this work, $T_D \approx 126 \mu\text{K}$). This limit is reached when the diffusive nature of light scattering competes with the cooling rate of the molasses. The subtle physics underlying polarization gradient cooling, in which the crossed polarization of the beams contributes to extra cooling, are beyond the scope of this discussion; a useful treat-

ment is given in [22]. With such sub-Doppler cooling, the limiting temperature is reduced to several recoils ($\sim 1 \mu\text{K}$ for cesium). Finally, long interrogation times in a $1 g$ environment are made possible by cooling atoms in an atomic fountain [23], in which counter-propagating laser beams with slightly different detunings, $\pm\Delta\omega$, both cool and accelerate atoms to a reference frame moving at velocity $v = \Delta\omega/k$.

1.3.2 State of the Art Atom Interferometric Inertial Sensors

Since the first atom interferometry experiments, orders of magnitude improvements in sensitivity to acceleration, rotation, and gravity gradients have been made. A summary of the current state of the art for each instrument class is given below.

Accelerometers

The best reported acceleration measurement by an atom interferometer is an atomic fountain experiment by Peters which measured gravitational acceleration with a sensitivity of $20 \text{ ng}/\sqrt{\text{Hz}}$ [24, 25]. After two days of averaging, the interferometer resolved local gravity to 0.1 ng . The interferometer interrogation time was $T = 160 \text{ ms}$, resulting in an induced phase shift of $\approx 3.8 \times 10^6 \text{ rad}$. Time series data from the experiment exhibit higher-order variations in gravity due to tidal effects, at the level where the data could test geophysical models; in addition, it has more recently been identified as providing the best measurement of the gravitational red shift predicted by general relativity, improving upon the previously achieved resolution of this effect by a factor of $\sim 10^4$ [26]. The accuracy of the gravity measurement was confirmed by comparison with an on-site, high accuracy falling corner-cube gravimeter (FG5, [27]) at the level of $7 \pm 7 \text{ ng}$. Extensions of this experiment could in principle achieve sensitivities at the level of $\sim 10^{-13} g/\sqrt{\text{Hz}}$ by using advanced atom optics and a larger baseline- such an experiment has been proposed in [28] for a test of the Einstein equivalence principle.

Gravity Gradiometers

Gravity gradiometers are useful for inertial navigation because individual accelerometers are unable to discriminate inertial acceleration from gravitational acceleration. As mentioned

above, this uncertainty in local vertical is a source of position error. The high sensitivity achieved by a suite of atom interferometric gravity gradiometers, however, could provide on-board gravity compensation [1]. Light pulse atom interferometry avails an elegant method for measuring gradients. The gradient is measured as the difference in gravitational acceleration between two cold atom interferometers separated along a baseline defined by a common interferometer beam. As a result, large sources of noise such as spurious platform motion or laser phase noise are common mode and consequently are highly suppressed in the differential measurement. Such an experiment by Fixler *et al.* reported a differential acceleration sensitivity at the level of $4 \text{ ng}/\sqrt{\text{Hz}}$, implying an individual accelerometer sensitivity of $2.8 \text{ ng}/\sqrt{\text{Hz}}$ and a gradient resolution of 0.65 E over a 1 m baseline⁴ [6, 29]. This system measured the Newtonian gravitational constant G with a precision of 4×10^{-4} , approaching the currently accepted uncertainty of 1.2×10^{-4} [30]. More recently, a portable cold atom gravity gradiometer demonstrated a similar differential acceleration sensitivity [31] as well as the capability for making mobile gravity gradient measurements [32].

Gyroscopes

The best reported atom interferometric gyroscope, built by Gustavson *et al.* [33], achieved a sensitivity of $69 \mu\text{deg}/\sqrt{\text{hr}}$ with a sodium atomic beam interrogated by a 2 m -baseline interferometer using stimulated Raman transitions. The sensitivity of this system was later improved to $3 \mu\text{deg}/\sqrt{\text{hr}}$ by overlapping a counter-propagating atomic beam in the same interrogation region [4, 5]. The bias stability of the apparatus was reported to be $< 70 \text{ deg/hr}$. An atomic beam was used instead of cold atoms because the rotation phase shift effectively scales as $L^2/v \propto T$, for baseline L and atom velocity v , rather than T^2 . The sensitivity of atomic beam gyroscopes, however, do not scale favorably at smaller form factors because of the factor of L^2 , and additionally suffer from phase dispersion from the longitudinal velocity distribution of the atomic beam.

The best reported cold atom gyroscope yielded a measured sensitivity of $8 \text{ mdeg}/\sqrt{\text{hr}}$ with $T = 52 \text{ ms}$, which was limited by high frequency environmental vibrations; measurements with a second, simultaneous interferometer implied a sensitivity of $295 \mu\text{deg}/\sqrt{\text{hr}}$ [34, 35]. Since the interrogation occurred in an atomic fountain, the volume of the interrogation region

⁴The traditional unit for gravity gradients is the Eotvos. $1 \text{ E} = 10^{-9} \text{ s}^{-2} \approx 0.1 \text{ ng/m}$

was substantially smaller ($\sim 0.1 \text{ m}^3$) than that of the atomic beam gyroscope.

1.4 Practical Atom Interferometric Sensor Technology

This section reviews advancements in atom interferometric inertial sensing with the overarching goal of operation outside of a laboratory. The first mobile atomic inertial sensor, called the Mobile Atomic Gravity Gradiometer Prototype Instrument (MAGGPI) was demonstrated in 2002 at Yale University [36]. A gravity gradiometer similar to that of McGuirk [29] was constructed on a truck platform with a portable laser, electronic control, ultra-high vacuum (UHV) chamber, and vibration isolation system. Subsequent work by this group produced a new generation of mobile atomic inertial sensors at Stanford University, starting with a gravity gradiometer in 2007 [31]. Two of these sensors, pictured in Fig. 1-4(i), include beam delivery and detection optics, vacuum cells and pumps, and multiple layers of magnetic shielding in a cube of $\sim 50 \text{ cm}$ per side. Within one enclosure, two independent atomic fountains could be interrogated simultaneously. In addition, the laser sources and electro-optics were engineered to withstand multiple- g shocks, but were housed on a separate cart. This sensor was installed in a truck and demonstrated an accurate gravity gradient mapping capability [32]. This system was also extended by Takase to perform multiple sensing functions as a gyroscope, accelerometer and gradiometer (with a pair of the sensors). The gyroscope sensitivity was noted in the previous section; a bias stability of 6.6 mdeg/hr was reported (again, the measured performance was limited by high frequency vibrations in the laboratory) [34]. This system presently represents the publicly-reported state of the art in mobile atomic inertial sensing. It is worth noting, however, that a private company, AOSense, Inc., is currently developing proprietary, deployable atom-based sensors and has likely made substantial improvements in raw sensing performance, and in size, weight, and power reduction.

Research by several groups in Europe has also made advances in engineering practical atom interferometers. Stern *et al.* made the first demonstration of atom interferometry in microgravity, in which a non-inertially sensitive interferometer was operated onboard an aircraft flying a parabolic ‘zero-G’ trajectory [38]. More recently, an accelerometer was demonstrated in a similar flight experiment, achieving a sensitivity of $20 \mu\text{g}/\sqrt{\text{Hz}}$ [39]. An important tech-

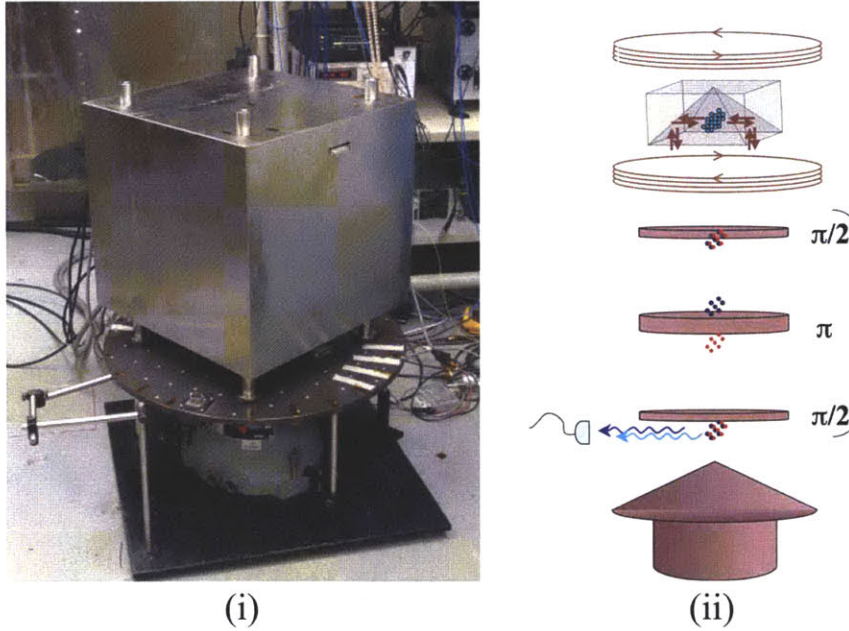


Figure 1-4: (i) Compact inertial sensor built at Stanford. The laser sources and electro-optics are housed externally. (Credit: [34]) (ii) Pyramidal cold atom gravimeter (Credit: [37]). Atoms are trapped in a pyramidal MOT and interrogated along the same axis as they fall.

nological development in this work involved transitioning from free-space, external cavity diode lasers to more robust fiber-based, telecommunications-wavelength components. Rubidium is a convenient atom, in this case, because frequency-doubled 1560 nm light produces the 780 nm transition used for trapping and interferometry [40]. Advances in fiber-coupled waveguides for frequency-doubling, as well as high power erbium-doped fiber amplifiers have enabled this work.

An interesting compact cold atom gravimeter by Bodart *et al.*, shown in Fig. 1-4(ii) used a pyramidal retroreflector to reduce the cooling, detection and interferometer optics to a single beam axis (with all the appropriate polarizations), and achieved a sensitivity of $0.2 \mu\text{g}/\sqrt{\text{Hz}}$ with $T = 40 \text{ ms}$ [37]. High bandwidth was not possible in the closed retroreflector geometry, however, because the interferometer could not be initiated until the atoms dropped out of the chamber by free fall. Another portable sensor launched two cold rubidium ensembles in counter-propagating trajectories in order to share interferometer beams and permit discrimination of both acceleration and rotation in one measurement (the vacuum chamber is $\approx 90 \text{ cm}$ long) [41]. In this configuration, one axis of acceleration and rotation are available since only the rotation phase shift changes sign with atom velocity (see Section 1.2). Efforts

to design high flux atom sources for rapid cold atom sample preparation have achieved MOT loading rates of 5×10^9 atoms/s [42] by increasing atom flux in the 3D MOT region with a 2D MOT.

Interest in designing completely atom-based IMUs has prompted schemes for multi-sensor concepts which measure all six degrees of freedom. Canuel *et al.* [43] demonstrated a proof-of-concept interferometer which provides complete six degree of freedom information (not simultaneously) by using two counter-propagating cold atom clouds and three spatially-separated laser beams. Kasevich and Dubetsky have also proposed methods for integrating data from a suite of atom interferometers to produce position estimates [44].

1.4.1 Enhanced Sensitivity

An important area of current research for developing high performance sensors involves enhancing sensitivity with large momentum transfer (LMT) atom optics, which do not constrain bandwidth or dynamic range (as is the case for longer interrogation times). As shown in Section 1.2, the precision of an atom interferometer increases linearly with the momentum transfer of the beam splitter, or equivalently, the area enclosed by the interferometer. A large momentum splitting was first proposed and demonstrated with Raman transitions, achieving up to $6\hbar k$ of momentum splitting by applying extra Raman pulses with alternating \mathbf{k}_{eff} , which can improve acceleration sensitivity by up to a factor of three [45]. In Chapter 5, this method is extended to up to $18\hbar k$, increasing the interferometer area by a factor of nine. Multi-order Bragg diffraction has also proven an effective method for large momentum transfer, with a current record of $24\hbar k$ for a single beam splitter pulse [46], and $102\hbar k$ for a sequential-pulse beam splitter [47]. Multi-order Bragg pulses, however, demand ultracold atom ensembles and higher laser power than used for driving Raman transitions. For low bandwidth, ultra-high precision applications, however, this approach could offer dramatic increases in sensitivity.

Another promising advance in sensing performance was the demonstration of a zero dead time (ZDT) interferometer measurement scheme. Dead time occurs in an atom interferometer while an atom sample is being prepared, and inertial sensitivity is lost. Since typical measurement schemes involve updating a reference oscillator with interferometer data, os-

illator phase noise accumulates during the dead time between measurements (for clocks, this phenomenon is known as the Dick effect [48]). Biedermann [31] demonstrated an interleaved pair of microwave clock interferometers that eliminated dead time and substantially improved ($\sim 15\times$) the long term stability over that of the individual clocks. This is primarily due to the fact that constant monitoring of the reference oscillator phase noise suppresses a phase random walk between the reference oscillator and the atoms. As a result, this technique yields averaging statistics with a $1/\tau$ scaling, where τ is measurement interval. By comparison, an individual clock is limited by $1/\sqrt{\tau}$ statistics. Subsequently, Takase proposed an inertially-sensitive ZDT interferometer that interleaves two four-pulse Raman interferometers [34]. These interleaved measurements provide a continuous measurement of velocity with similarly high suppression of oscillator phase noise, a factor that has important implications for improving the accuracy of an inertial navigation system.

1.4.2 Guided Atom Interferometry

Atom chip technology and guided atom interferometry, as opposed to the ‘free space’ interferometry approach described above, represent another rapidly developing field of relevance to inertial sensing. Atom chips have already demonstrated the capability to guide atoms above MEMS-fabricated magnetic guides [49] as well as produce, manipulate, and interfere Bose-Einstein condensates (BEC) [50,51]. Area-enclosing guided atom interferometers were demonstrated by Jo *et al.* [52] and Wu *et al.* [53], which achieved long coherence times with atoms confined by magnetic fields (the former achieved ~ 200 ms coherence times with BECs). In principle, the latter system could provide a large area atomic gyroscope in a compact sensor by translating the guide back and forth over the same area (this allows wavepacket paths to be reciprocal, which could reduce several systematic errors). In practice, coherence times are limited by the smoothness of magnetic fields close to the chip surfaces.

Finally, atom interferometers using BECs have attracted interest because of the longer coherence times available with a colder, denser ensemble of atoms. While the initially colder temperature permits longer interrogation times, condensates require significantly longer preparation time than for thermal ensembles of cold atoms, and result in lower atom numbers. The most common method for producing BECs involves evaporative cooling, which is

limited by fundamental atomic collisional rates. BECs are typically created on ~ 1 second time scales, rather than the millisecond time scales that are possible with higher flux MOT-based sources. For instance, a state of the art, portable rubidium BEC system ($\approx 0.4 \text{ m}^3$) achieved a repetition rate of 0.3 Hz [54]. In addition, density-dependent atom-atom interactions can lead to systematic phase shifts and dephasing [55]. Nevertheless, for applications with less stringent bandwidth requirements, ultracold atoms could avail unprecedented sensitivity with longer interrogation times and large momentum transfer atom optics [47].

While presently a less mature technology than free space interferometry, chip-based atom interferometers might provide a competitive sensor architecture for some applications in the future.

1.4.3 Remaining Problems

In summary, the development of atomic inertial sensors for navigation applications is in an early but rapidly growing stage. Building on the current wealth of successful laboratory demonstrations, there is increasing interest in engineering compact, high performance, atom interferometric instruments. As the previous discussion motivates, many notable achievements have already been made in this field, but many important engineering challenges remain. In addition, as scientific advances continue to be made in atom interferometry, considerable room remains for defining the physics-level design of these sensors.

This thesis focuses both on the design of the interferometer as well as technical factors affecting sensor performance, such as vacuum cell and optical design. The contributions of this thesis, listed below, take steps toward realizing an atom interferometric accelerometer with the accuracy, bandwidth, dynamic range, and size, weight and power required for inertial sensors in flight navigation systems. The approach of this work is to design and build a laboratory atom interferometric gravimeter as a testbed for investigating performance at short interrogation times, including methods for improving sensitivity and characterizing error sources.

1.5 Thesis Contributions

1. The first contribution of this thesis is the demonstration of a short interrogation time ($2T < 15$ ms) gravimeter in a compact (≈ 80 cc) vacuum cell. This approach is different from previous work in that the entire measurement cycle is completed in a single, small volume. High contrast interference was observed, which improved interferometer phase sensitivity. The system achieved an inferred acceleration sensitivity of $2 \mu\text{g}/\sqrt{\text{Hz}}$ for an interrogation time of $2T = 10$ ms, with a repetition rate of 2 Hz. With realistic expectations for improvements in atom count, detection SNR, and repetition rate, a high bandwidth (~ 100 Hz) accelerometer meeting the specifications of high performance flight navigation systems should be feasible.
2. A second contribution of this thesis is the demonstration of large area Raman pulse atom interferometry, using sequential Raman pulses to achieve large momentum transfer. The inertial phase shift measured by an atom interferometer is proportional to the enclosed area of the atomic wavepackets. The implementation of composite Raman pulses, analogous to composite pulse techniques developed for nuclear magnetic resonance (NMR) spectroscopy, significantly improved Raman pulse transfer efficiency, which ultimately limits the gain in precision. The area of a Raman pulse interferometer was increased by up to a factor of nine, which is the largest reported to date. Large area interferometry is well-suited to a high bandwidth inertial sensor design because it improves precision without increasing interrogation time, which is constrained in practice by sensor bandwidth and size. Moreover, the method implemented here does not require colder atoms or significantly different interferometer beam parameters to increase sensitivity over the conventional three-pulse interferometer. Other large momentum transfer atom optics (e.g., multi-photon Bragg transitions) require samples with sub-recoil temperatures, which limits atom count or repetition rate (in the case of ultracold atoms). Finally, composite Raman pulses were demonstrated to improve the robustness of the atom optics to realistic factors such as large detunings (e.g., due to impulses) and a non-uniform Raman beam; such robustness could be beneficial for sensor performance in dynamic sensing applications.

3. The third major contribution of this thesis is the identification and experimental characterization of the impact of coherent population trapping (CPT) on Raman pulse atom interferometers. It is argued that these interferometers, including the common three-pulse interferometer used for measuring acceleration and rotation rate, experience a systematic phase offset as a consequence of CPT effects. In an inertial measurement, this effect is a source of bias. While CPT is a well-understood physical effect, its impact on atom interferometry has not been considered in previous work. A method for suppressing this effect in realistic operation is also discussed. In addition to the primary relevance of this work in understanding the performance of atom interferometric inertial sensors, the experimental approach for studying transient CPT effects in cold atoms is scientifically novel.

1.6 Thesis Outline

The next chapter presents a summary of the theory of Raman pulse atom interferometry, the sensing modality used in this work. This discussion describes the physics of inertially-sensitive interferometry and provides a conceptual framework for the experimental results discussed in later chapters. Chapter 3 describes the experimental apparatus developed for this thesis. Chapter 4 presents an investigation of atom interferometry at short interrogation times, focusing on design factors affecting performance as an inertial sensor for dynamic applications. The apparatus is used to measure gravity as a test. Chapter 5 presents a method for increasing the precision of Raman pulse interferometers by large momentum transfer with sequential Raman pulses. Composite Raman pulses are proposed as a robust atom optic, and demonstrated to improve the performance of large area interferometers. Chapter 6 describes the impact of coherent population trapping (CPT) on Raman pulse atom interferometers. Both theoretical and experimental results are presented, along with a method for suppressing the effect. Finally, Chapter 7 summarizes the results of the thesis and suggests areas for future work.

THIS PAGE INTENTIONALLY LEFT BLANK

Chapter 2

Atom Interferometer Theory

This chapter describes the theory of stimulated Raman transitions, which comprise the atom optics used for interferometry in this thesis. In addition, the phase and frequency response of a three-pulse $\pi/2 - \pi - \pi/2$ interferometer are analyzed. Systematic effects relevant to short interrogation time interferometry, such as finite pulse length effects, are also discussed.

2.1 Stimulated Raman Transitions

Light pulse atom interferometers employ the kinematic effects of light to split atomic wavepackets. In this work, cesium atoms are coherently manipulated by stimulated Raman transitions. Figure 2-1 shows an energy diagram for a stimulated Raman transition, in which two ground states, $|g\rangle$ and $|e\rangle$, of a three-level atom are coupled via an intermediate excited state $|i\rangle$ by two off-resonant, coherent optical fields with frequencies ω_1 and ω_2 . The two ground states are typically hyperfine ground states in an alkali atom, with \sim GHz separations.

Raman transitions provide a useful atom optic for several reasons. When the two fields are counter-propagating (Doppler sensitive, $\mathbf{k}_1 \approx -\mathbf{k}_2$) and their frequency difference, $\omega_1 - \omega_2$, is equal to the hyperfine splitting ω_{HF} , the atom makes a transition from one ground state to the other, and experiences a change in momentum $\hbar\mathbf{k}_{\text{eff}} = \hbar(\mathbf{k}_1 - \mathbf{k}_2) \approx 2\hbar\mathbf{k}_1$. The atom absorbs a photon from one field and stimulates emission into the other, yielding two photon recoils of momentum. For example, a cesium atom acquires a velocity of $v_r = \hbar k_{\text{eff}}/m \approx 7$ mm/s. This is a factor of $\sim 10^5$ larger than the velocity kick from a microwave transition between the ground states (≈ 92 nm/s). By detuning the individual frequencies from optical resonance

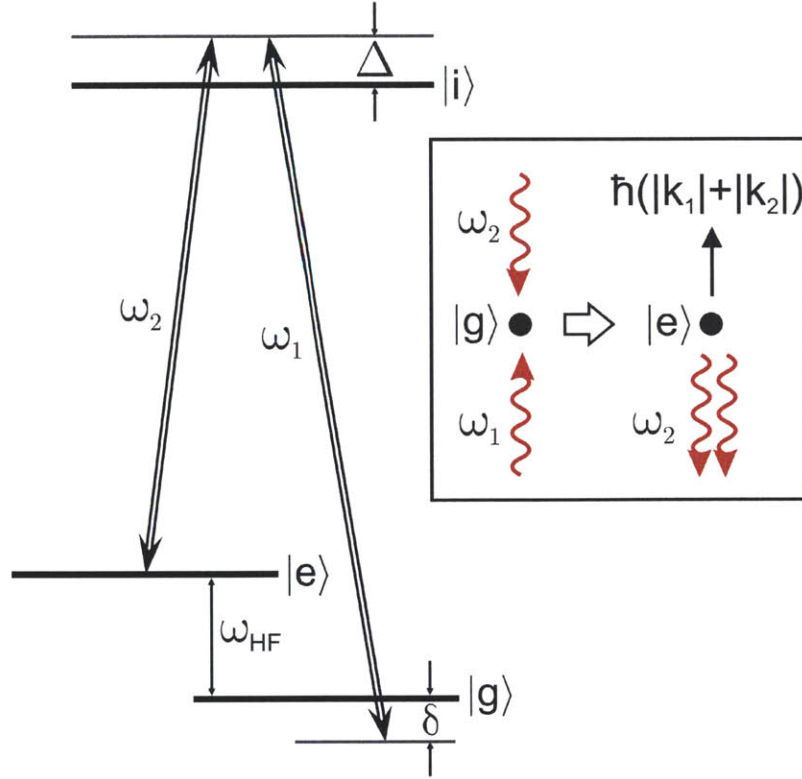


Figure 2-1: Energy level and momentum transfer diagrams of a stimulated Raman transition.

(Δ), decoherence from spontaneous emission can be suppressed. As a result, the atom can be prepared in a coherent superposition of the two hyperfine ground states. In principle, metastable optical transitions can achieve both coherent transfer and large momentum transfer; however, ultra-stable lasers are required to excite these transitions (such lasers do exist, but are currently at the state of the art; e.g., [56]). Raman transitions do not require this level of optical frequency stability. Instead, the two-photon resonance depends on the difference between the two optical frequencies ($\omega_{HF} \approx 9.2$ GHz in cesium), meaning that only the frequency difference needs to be highly stable for precise interferometry. The appropriate frequency difference can easily be produced by phase-modulating a single laser beam with an electro-optic modulator (EOM), using a low noise RF signal generator stabilized to an atomic reference.

The theory of stimulated Raman transitions has been treated in great detail in previous work [57–60]. This section provides a basic, semi-classical treatment of coherent population transfer, and a derivation of the resonance condition. The analysis is carried out in the laboratory frame where the ground state, $|g\rangle$, initially has momentum p . The Hamiltonian

for the three-level atom, H_0 and atom-light interaction is

$$H = H_0 + V = \frac{\mathbf{p}^2}{2m} + \hbar\omega_g^A |g\rangle\langle g| + \hbar\omega_e^A |e\rangle\langle e| + \hbar\omega_i^A |i\rangle\langle i| + V \quad (2.1)$$

where \mathbf{p} is the momentum operator, $\hbar\omega_j^A$ is the energy of internal state $|j\rangle$, and V is an operator describing the atom-light interaction. This interaction occurs between the atom and two optical fields (the Raman fields)

$$\mathbf{E} = \mathbf{E}_1 \cos(\mathbf{k}_1 \cdot \mathbf{z} - \omega_1 t + \phi_1^0) + \mathbf{E}_2 \cos(\mathbf{k}_2 \cdot \mathbf{z} - \omega_2 t + \phi_2^0), \quad (2.2)$$

where field \mathbf{E}_1 couples $|g\rangle \rightarrow |i\rangle$ and field \mathbf{E}_2 couples $|e\rangle \rightarrow |i\rangle$, as shown in Fig. 2-1. This simplifying assumption neglects cross-coupling (e.g., field \mathbf{E}_1 coupling $|e\rangle \rightarrow |i\rangle$), which is reasonable since typically $\omega_{HF} > \Delta$. In the electric dipole approximation, the interaction Hamiltonian can be written as

$$V = -\mathbf{e}\mathbf{r} \cdot \mathbf{E} \quad (2.3)$$

where $-\mathbf{e}\mathbf{r}$ is the dipole moment. Spontaneous emission from single photon excitation of the atom to level $|i\rangle$ is neglected by assuming that the detuning from optical resonance is sufficiently large compared to the average decay rate, Γ ($\Delta \gg \Gamma$). Importantly, Raman transitions create a correlation between the internal state of the atom and its momentum. The atomic state is denoted $|j, p\rangle$, where j refers to the internal energy state and p is the momentum state of the atom. The Schrödinger equation is solved by assuming eigenstates of the form

$$|\psi\rangle = \int dp \sum_j c_{j,p}(t) \exp[-i(\omega_j^A + \mathbf{p}^2/2m)t] |j, p\rangle \quad (2.4)$$

where the time-dependent population in state $|j, p\rangle$ is represented by probability amplitude $c_{j,p}(t)$. For a particular momentum p and effective wavevector $\mathbf{k}_{\text{eff}} = \mathbf{k}_1 - \mathbf{k}_2$, the Schrödinger equation reduces to coupled equations of motion between the populations $c_{g,p}(t)$, $c_{e,p+\hbar\mathbf{k}_{\text{eff}}}(t)$, and $c_{i,p+\hbar\mathbf{k}_1}(t)$:

$$\begin{cases} \dot{c}_{g,p}(t) &= \frac{i}{2}\Omega_{gi}^* e^{i\Delta_1 t} c_{i,p+\hbar\mathbf{k}_1} \\ \dot{c}_{e,p+\hbar\mathbf{k}_{\text{eff}}}(t) &= \frac{i}{2}\Omega_{ei}^* e^{i\Delta_2 t} c_{i,p+\hbar\mathbf{k}_1} \\ \dot{c}_{i,p+\hbar\mathbf{k}_1}(t) &= \frac{i}{2}(\Omega_{gi} e^{-i\Delta_1 t} c_{g,p} + \Omega_{ei} e^{-i\Delta_2 t} c_{e,p+\hbar\mathbf{k}_{\text{eff}}}) \end{cases} \quad (2.5)$$

where Ω_{ji} are single photon Rabi frequencies between states $|j\rangle$ and $|i\rangle$,

$$\Omega_{gi} = \frac{e}{\hbar} \langle i | \mathbf{r} \cdot \mathbf{E}_1 | g \rangle e^{i\phi_1}, \quad \Omega_{ei} = \frac{e}{\hbar} \langle i | \mathbf{r} \cdot \mathbf{E}_2 | e \rangle e^{i\phi_2} \quad (2.6)$$

with position-dependent phases $\phi_j = \mathbf{k}_j \cdot \mathbf{z} + \phi_j^0$. Laser detunings are defined as

$$\begin{aligned} \Delta_1 &\equiv [\omega_1 - (\omega_i^A - \omega_g^A)] + \frac{p^2}{2m} - \frac{(p + \hbar k_1)^2}{2m}, \\ \Delta_2 &\equiv [\omega_2 - (\omega_i^A - \omega_e^A)] + \frac{[p + \hbar k_{\text{eff}}]^2}{2m} - \frac{(p + \hbar k_1)^2}{2m} \end{aligned} \quad (2.7)$$

The rotating wave approximation has also been made in the equations of motion, to eliminate terms with high frequency dependencies $\sim (\omega_1 + (\omega_i^A - \omega_g^A))$ or $\sim (\omega_2 + (\omega_i^A - \omega_e^A))$.

The evolution of the three-level system in Eq. (2.5) can be reduced to an effective two-level system by performing adiabatic elimination on the excited state. In this approximation, it is assumed that the excited state population is small ($c_{i,p+\hbar k_1}(t) \ll 1$) and slowly varying compared to the ground states ($\dot{c}_{i,p+\hbar k_1}(t) \approx 0$) as a consequence of large detuning Δ . After integrating the equation of motion for the excited state and substituting into the other equations, the resulting equations of motion are

$$\begin{cases} \dot{c}_{g,p}(t) &\approx -i\Omega_{AC,g} c_{g,p} - \frac{i}{2} e^{i\delta t} \Omega_{\text{eff}} c_{e,p+\hbar k_{\text{eff}}} \\ \dot{c}_{e,p+\hbar k_{\text{eff}}}(t) &\approx -i\Omega_{AC,e} c_{e,p+\hbar k_{\text{eff}}} - \frac{i}{2} e^{-i\delta t} \Omega_{\text{eff}} c_{g,p} \end{cases} \quad (2.8)$$

where

$$\delta \equiv \Delta_1 - \Delta_2 = (\omega_1 - \omega_2) - \left[\omega_{HF} + \mathbf{k}_{\text{eff}} \cdot \mathbf{v} + \frac{\hbar k_{\text{eff}}^2}{2m} \right] \quad (2.9)$$

$$\Omega_{AC,j} \equiv \frac{|\Omega_{ji}|^2}{4\Delta} \quad (2.10)$$

$$\Omega_{\text{eff}} \equiv \frac{\Omega_{gi}^* \Omega_{ie}}{2\Delta} = \frac{|\Omega_{gi}| |\Omega_{ei}| e^{i\phi_{\text{eff}}}}{2\Delta} \quad (2.11)$$

$\Omega_{AC,j}$ is the AC Stark shift of level j , and Ω_{eff} is the effective (two-photon) Rabi frequency (it has been assumed in these definitions that $\Delta_1 \approx \Delta_2$). Note that the effective Rabi frequency is complex, with an associated phase $\phi_{\text{eff}} = \phi_2 - \phi_1$. The interaction of the Raman fields with the atom imprints this phase on the atomic wavefunction. The Raman detuning (δ)

includes detunings from the hyperfine splitting frequency, Doppler shifts, and the recoil shift of $|e\rangle$. The differential AC Stark shift,

$$\delta_{AC} \equiv \Omega_{AC,e} - \Omega_{AC,g} \quad (2.12)$$

also contributes to the detuning, but is typically tuned to zero in experiment.

Finally, these equations can be easily solved for Raman-resonant fields ($\delta = 0$). Assuming the atom is initially in state $|g\rangle$, $|\psi(t_0)\rangle = |g\rangle$, the final state of the atom after a Raman pulse starting at time t_0 and having duration τ is

$$|\psi(t_0 + \tau)\rangle = \cos\left(\frac{\Omega_{\text{eff}}\tau}{2}\right) |g\rangle - ie^{i\phi_{\text{eff}}} \sin\left(\frac{\Omega_{\text{eff}}\tau}{2}\right) |e\rangle \quad (2.13)$$

For an atom initially in state $|e\rangle$, the state of the atom after the Raman pulse is

$$|\psi(t_0 + \tau)\rangle = \cos\left(\frac{\Omega_{\text{eff}}\tau}{2}\right) |e\rangle - ie^{-i\phi_{\text{eff}}} \sin\left(\frac{\Omega_{\text{eff}}\tau}{2}\right) |g\rangle \quad (2.14)$$

The results in Eqs. (2.8), (2.13), and (2.14) are equivalent to the standard equations of motion for a two-level atom driven by an oscillating electric field (see, e.g., [61]). As a result, similar terminology is used to describe Raman pulse atom optics. An atom beam splitter is achieved with a pulse of duration

$$t_{\pi/2} \equiv \frac{\pi}{2\Omega_{\text{eff}}}, \quad (2.15)$$

which prepares the atom in a balanced, coherent superposition of the two ground states (a $\pi/2$ pulse). A mirror, which flips the state of the atom with certainty, is accomplished by a π pulse. In both cases, the wavefunction of the atom is imprinted with the effective laser phase ϕ_{eff} . The following sections show that this phase is one of the dominant contributions to an atom interferometer.

2.1.1 Pseudospin Representation

Several of the results in this thesis are intuitively presented by recasting the two-level dynamics derived above into the Bloch sphere, where the atomic state is represented as a pseudospin vector on a Bloch sphere. It can be shown that for this two-level system (typi-

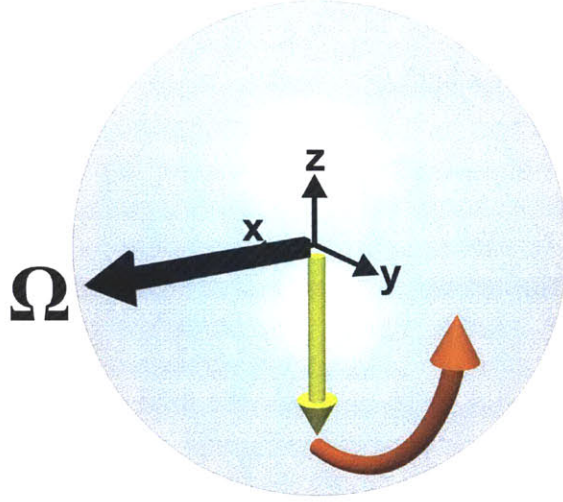


Figure 2-2: Rotation of the atomic pseudospin (yellow) by a Raman pulse. The effective drive field produced by the Raman fields is represented by Ω .

cally two hyperfine ground states of the atom), a Raman pulse acts to rotate the pseudospin about an effective drive field vector, analogous to a classical magnetization precessing about an oscillating magnetic field (for a complete derivation, see [60]).

The atomic wavefunction can be expressed as a spin vector $\mathbf{P}(t)$ on the Bloch sphere by projecting the two-level density matrix

$$\rho(t) = |\psi(t)\rangle\langle\psi(t)| = \sum_{m,n} c_m^*(t)c_n(t)|m\rangle\langle n|, \{m,n\} = e,g \quad (2.16)$$

onto the Pauli spin matrices, $\{\sigma_x, \sigma_y, \sigma_z\}$. The resulting components are defined as

$$P_j(t) \equiv \text{Tr}[\rho(t) \cdot \sigma_j], \quad j = x, y, z$$

$$\mathbf{P}(t) = \begin{bmatrix} P_x(t) \\ P_y(t) \\ P_z(t) \end{bmatrix} = \begin{bmatrix} 2\text{Re}[r_{eg}] \\ -2\text{Im}[r_{eg}] \\ \rho_{ee} - \rho_{gg} \end{bmatrix} \quad (2.17)$$

where σ_j are the Pauli spin matrices, ρ_{ee} and ρ_{gg} are the ground state populations, and r_{eg} is the coherence between the ground states. One sees that $P_z(t)$ captures the population difference between the two ground states, and that the equatorial components $P_x(t)$ and $P_y(t)$ describe the coherence formed by the Raman fields between the two states.

As shown in [62], the equation of motion for the pseudospin in the presence of the Raman

fields, neglecting spontaneous emission, is

$$\frac{d}{dt}\mathbf{P}(t) + \mathbf{P}(t) \times \boldsymbol{\Omega} = \mathbf{0} \quad (2.18)$$

where $\boldsymbol{\Omega} = \Omega[\hat{z} \cos \theta + \sin \theta(\hat{x} \cos \phi + \hat{y} \sin \phi)]$ is the effective drive field vector, and $\Omega = \sqrt{|\Omega_{\text{eff}}|^2 + (\delta_{AC} - \delta)^2}$ is the generalized Rabi frequency. The variable θ determines the detuning-dependent polar angle of the drive field vector, and is defined by

$$\cos \theta = \frac{\delta_{AC} - \delta}{\Omega}, \quad \sin \theta = \frac{|\Omega_{\text{eff}}|}{\Omega} \quad (2.19)$$

Figure 2-2 depicts the action of a Raman pulse on an atom initially in $|g\rangle$ ($\mathbf{P}(0) = -\hat{z}$). Interestingly, the dynamics in Eq. (2.18) are isomorphic to the dynamics of magnetic resonance [63]– the pseudospin precesses about a drive field vector at a generalized Rabi frequency. Many of the results presented in this work are intuitively described in this framework, which is of great utility for understanding both theoretical and experimental aspects of light pulse atom interferometry.

2.2 Interferometer Theory

The simplest light pulse interferometer for measuring acceleration is the three-pulse $\pi/2 - \pi - \pi/2$ sequence. Figure 2-3 shows the trajectory of free-falling atoms interrogated by this sequence. The first $\pi/2$ pulse acts as a beam splitter that divides the atoms into two coherent wavepackets, separating by $\Delta z = \hbar k_{\text{eff}} T / m$ over the free evolution period, or dwell time, T . When the Raman fields are Doppler sensitive, Δz is much greater than the coherence length of the atoms, $\Delta x_C = \hbar / \Delta p$, where Δp is width of the momentum distribution. For cesium, the two-photon recoil velocity is ≈ 7 mm/s and the coherence length for atoms with $\sim \mu\text{K}$ temperature is $\sim 10^{-8}$ m. Unlike in a microwave or co-propagating (Doppler insensitive) Raman interferometer, overlap is not guaranteed for arbitrary pulse sequences. To achieve overlap, the wavepackets are deflected toward each other by a mirror (π) pulse, recombining another interval T later. A second beam splitter pulse then recombines the wavepackets and interferes them.

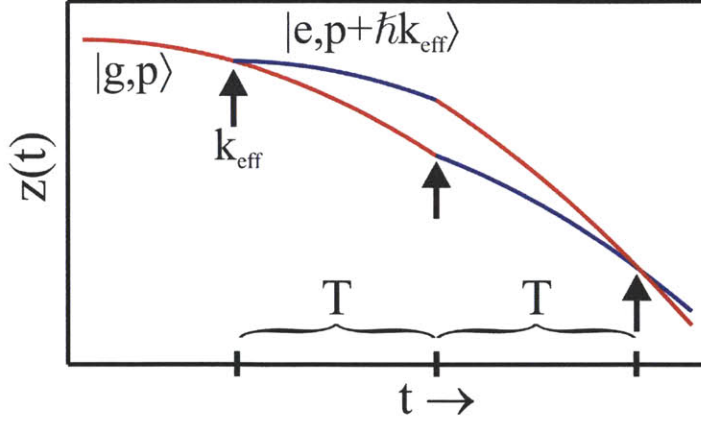


Figure 2-3: Trajectory of the $\pi/2 - \pi - \pi/2$ interferometer paths for a gravimeter ($\mathbf{a} = -g\hat{z}$). The arrows represent the three Raman pulses interrogating the free-falling atoms. The color of the arms represent the internal states of the atom along each path.

2.2.1 Interferometer Phase Shifts

This section describes sources of phase shifts in the $\pi/2 - \pi - \pi/2$ interferometer, including several higher-order effects relevant to inertial sensing applications. The interferometer phase can be determined by calculating the evolution of the wavefunction through the three Raman pulses and two free evolution periods. Several good references present approaches to calculating interferometer phase for a variety of fields and inertial forces (accelerometer, gyroscope, etc.) [57, 59, 64]. The interferometer measures differential phase shifts accrued between the two arms, which can be divided into

$$\Delta\phi = \Delta\phi_{\text{light}} + \Delta\phi_{\text{prop}} + \Delta\phi_{\text{sep}} \quad (2.20)$$

where $\Delta\phi_{\text{light}}$ is the phase resulting from the interaction with the Raman fields, $\Delta\phi_{\text{prop}}$ is the differential phase accrued during the free propagation between light pulses, and $\Delta\phi_{\text{sep}}$ is the phase shift introduced by spatially-separated wavepackets during the final pulse. Each phase shift is summarized below.

2.2.2 Laser Interaction Phase Shifts

In the $\pi/2 - \pi - \pi/2$ interferometer, the dominant phase shift for inertial sensing is produced by the Raman pulse manipulations of the atoms. As noted in Section 2.1, the relative phase

of the Raman fields is imprinted on the atomic wavepackets by each pulse. The total phase shift due to the three pulses is

$$\Delta\phi_{\text{light}} = \phi(z_1, t_1) - [\phi(z_2^u, t_2) + \phi(z_2^l, t_2)] + \phi(z_3, t_3) \quad (2.21)$$

where $\phi(z, t) = \mathbf{k}_{\text{eff}} \cdot \mathbf{z} - (\omega_1 - \omega_2)t + \phi_{\text{eff}}^0$ is the effective laser phase at location z and time t , and $\phi_{\text{eff}}^0 = \phi_2^0 - \phi_1^0$. The position superscript distinguishes the local phases sampled by the upper and lower wavepackets during the second pulse. For an atom accelerating under gravity along \mathbf{z} , the resulting phase is

$$\Delta\phi_{\text{light}} = \mathbf{k}_{\text{eff}} \cdot \mathbf{g}T^2 + (\phi_{\text{eff},1}^0 - 2\phi_{\text{eff},2}^0 + \phi_{\text{eff},3}^0) \quad (2.22)$$

In this equation, it has been assumed that the pulse durations are negligible compared to T , and that the laser frequency difference is held constant in all three pulses. In this case, the frequency-dependent terms cancel. If a constant rotation $\boldsymbol{\Omega}$ occurs as well, additional phase terms are introduced:

$$\Delta\phi_{\text{rot}} = \frac{2m}{\hbar}\boldsymbol{\Omega} \cdot \mathbf{A} - \mathbf{k}_{\text{eff}} \cdot (\boldsymbol{\Omega} \times \mathbf{g})T^3, \quad (2.23)$$

where \mathbf{A} is the area enclosed by the wavepackets. Since this work focuses on measuring acceleration, a derivation of these shifts is beyond the scope of this chapter. A useful derivation is provided in [34]. It is worth noting that, in addition to the familiar Sagnac phase shift, there is a term scaling as $\sim T^3$ that introduces cross-coupling of acceleration and rotation. This phase shift must be carefully accounted for in calibrating the scale factor of individual sensors in an inertial measurement unit.

The intuitive inertial phase shift expression in Eq. (2.22) illustrates the role of the Raman fields as a ‘ruler’ for the motion of the atom, with resolution scaled by the effective wavelength $\lambda_{\text{eff}} = 2\pi/k_{\text{eff}}$. For Doppler sensitive Raman transitions in cesium, $\lambda_{\text{eff}} \approx 426$ nm. It is also notable that the inertial input can be measured by chirping the laser frequency difference at a rate α , producing a net phase $\Delta\phi_{\text{light}} = (\mathbf{k}_{\text{eff}} \cdot \mathbf{g} - \alpha)T^2$. For the obvious choice of $\alpha = \mathbf{k}_{\text{eff}} \cdot \mathbf{g}$, the inertial phase shift is canceled for any T (this is useful for preserving resonance during the pulses, and for fringe disambiguation in a static measurement). The scale factor of the acceleration measurement is $|\mathbf{k}_{\text{eff}}|T^2$, meaning that precision increases linearly with the

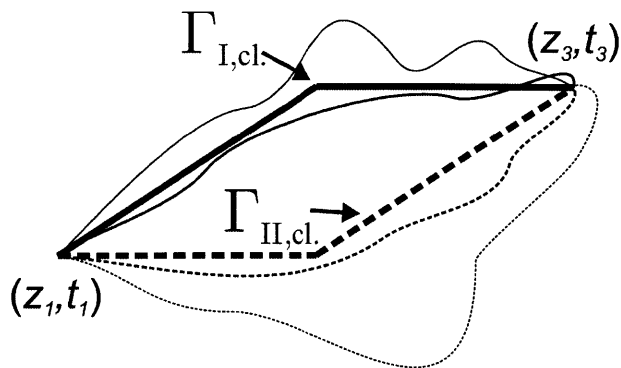


Figure 2-4: Free propagation along paths $\Gamma_{I,cl.}$ and $\Gamma_{II,cl.}$ contributes a phase difference if the wavepackets do not experience the same potential along their respective paths (e.g., a spatially-varying magnetic field). A rigorous calculation sums over the contribution of all possible paths, but including only the contribution of the classical paths provides a very good approximation.

momentum splitting of the beam splitter and quadratically with the interrogation time.

Constant detunings from resonance, due to unaccounted magnetic or AC Stark shifts, do not contribute to a net phase difference if the fields are spatially and temporally uniform. This fact makes sense when considering that a $\pi/2 - \pi - \pi/2$ sequence is essentially two consecutive Ramsey ($\pi/2 - \pi/2$) sequences. One also observes that the initial velocity of the atom does not contribute to a phase shift. This is critical for achieving high phase contrast, even with a narrow velocity distribution. Other light-induced phase shifts can result from processes such as coherent population trapping (CPT) [62] or higher-order light shifts from off-resonant Raman processes [65]. Chapter 6 presents a characterization of CPT effects on Raman pulse atom interferometers.

2.2.3 Free Propagation Phase

During the periods between Raman pulses, the wavepackets accrue phase along their respective paths. The free propagation phase $\Delta\phi_{\text{prop}}$ is typically calculated with the Feynman path integral approach. A general overview of this method is presented in [66], and a practical tutorial for calculating these integrals in typical atom interferometers is given by [67]. The Feynman path integral formulation is also useful because it provides an intuitive way of estimating phase shifts introduced by systematic effects such as spatially-inhomogeneous or time-varying magnetic fields.

The free propagation phase shift between the two arms of the interferometer is

$$\Delta\phi_{\text{prop}} = \frac{1}{\hbar} (S_{\Gamma_I} - S_{\Gamma_{II}}) = \frac{1}{\hbar} \left(\int_{\Gamma_I} L(z, \dot{z}) dt - \int_{\Gamma_{II}} L(z, \dot{z}) dt \right) \quad (2.24)$$

where S_Γ is the classical action integral for path Γ , $L(z, \dot{z}) = \frac{1}{2}m\dot{z}^2 - V(z)$ is the Lagrangian of the atom, $V(z)$ is the potential energy (e.g., a gravitational field), and Γ is the path taken by the wavepacket along each arm of the interferometer, as shown in Fig. 2-4. A rigorous calculation of these action integrals in quantum mechanics requires summing over the contributions of all paths between $z(t_1)$ and $z(t_3)$. However, evaluating along the classical trajectories of the wavepackets provides a very good approximation ($\Delta g \approx 10^{-20}g$, [68]).

For the case of equal dwell times between pulses and no gravity gradients, the net phase from free propagation cancels. This is a result of the fact that the wavepackets spend equal time in the two hyperfine ground states, and overlap at the time of the third pulse. The presence of gravity gradients introduces a differential phase shift because the interferometer arms experience different gravitational potentials while spatially-separated. Considering a linear vertical gravity gradient γ , the phase shift can be calculated with the Lagrangian

$$L(z, \dot{z}) = \frac{1}{2}m\dot{z}^2 - mgz + \frac{1}{2}m\gamma z^2 \quad (2.25)$$

and by evaluating the integral in Eq. (2.24). The resulting phase shift is

$$\Delta\phi_{\text{prop}} = k_{\text{eff}}\gamma T^2 \left(\frac{7}{12}gT^2 - \dot{z}(0)T - z(0) \right) \quad (2.26)$$

where $\dot{z}(0) = \dot{z}(0) + \frac{1}{2}v_r$ is the mean velocity of the two wavepackets after the beam splitter pulse. At short interrogation times, this phase shift is small.

2.2.4 Separation Phase

In a uniform gravitational field, the atom wavepackets overlap perfectly when the Raman pulses are equally spaced. The introduction of gravity gradients and rotation, however, can lead to spatial separation at the time of the final pulse. For a relative separation of Δz at

the time of the final beam splitter pulse, the phase shift introduced is

$$\Delta\phi_{\text{sep}} = \frac{\bar{\mathbf{p}} \cdot \Delta\mathbf{z}}{\hbar} \quad (2.27)$$

In this equation, $\bar{\mathbf{p}}$ is the mean classical canonical momentum of the wavepackets at the output of the interferometer. This phase shift essentially accounts for the extra phase accumulated by a plane wave over Δz . For a matter wave, the phase shift induced by the separation is scaled by $\Delta z/\lambda_{\text{dB}}$, where λ_{dB} is the deBroglie wavelength. At short interrogation times, this is also typically a small phase contribution.

2.2.5 Finite Pulse Duration Effects

The expression for the laser interaction phase shift in Eq. (2.22) assumes that the Raman pulses are negligibly short in duration compared to the interrogation time T (the short pulse limit). In other words, the light pulse ‘grating’ is considered to be infinitely thin [69]. More detailed calculations, such as those by Peters [24], Antoine [70], and Stoner *et al.* [60], include the effects of detuning variation within the interferometer pulses, and predict corrections to the accelerometer and gyroscope scale factors. For instance, the analysis in [60] finds the phase shift due to a constant acceleration and constant laser frequency difference is, to second order in τ/T ($\tau = t_{\pi/2}$):

$$\Delta\phi = k_{\text{eff}}aT^2 \left[1 + \frac{4\tau}{\pi T} + \frac{\tau^2}{T^2} \left(\frac{2}{\pi} - 1 \right) \right] \quad (2.28)$$

The analysis by Antoine, [70], incorporates additional effects relating to the motion of the wavepackets during light pulses, and produces a slightly different result. Specifically, the latter analysis includes the atomic Borrmann effect, which shifts the path of the incoming wavepacket during the pulse (other analyses assume that the diffraction occurs exactly at the center of the pulse). As a result, the interferometer area, and thus the acceleration scale factor, are modified.

A detailed discussion of these analyses is beyond the scope of this chapter; nevertheless, these scale factor modifications are clearly more significant for short interrogation times; e.g., the first order effect on the phase of a $T = 1$ ms interferometer is typically $\sim 1\%$. It

is worth noting, however, that this correction does not apply to the case where the Raman laser frequency difference is chirped to compensate for the linear variation in the Doppler shift, preserving resonance throughout the interrogation. The modified scale factor would only appear in the phase shift resulting from the difference between the acceleration implied by the applied chirp rate, $\hat{a} = \alpha/k_{\text{eff}}$, and the actual acceleration experienced during the interferometer.

2.3 Interferometer Frequency Response

Thus far, the discussion of acceleration sensitivity has been restricted to constant accelerations. For inertial navigation applications, it is important to consider the frequency response of the interferometer, and choose an appropriate interrogation time to capture the desired vehicle dynamics. The transfer function of the $\pi/2 - \pi - \pi/2$ interferometer is determined by calculating the interferometer phase induced by a vibrational acceleration at a defined frequency, ω :

$$a(\omega, t) = a_c \cos \omega t + a_s \sin \omega t, \quad (2.29)$$

with the time origin arbitrarily defined as the time of the center of the π pulse. The acceleration response function is plotted in Fig. 2-5, for $T = 1$ ms. The sensitivity of the interferometer rolls off as $\sim 1/\omega^2$ at frequencies higher than $1/T$, i.e., it acts as a low pass filter. In addition, the interferometer is insensitive to acceleration Fourier components at frequencies that are multiples of $1/T$, since the platform position is equal at each pulse. This analysis is also relevant to assessing noise produced by platform vibrations in a gravimeter. For instance, a vibration at a particular frequency could in principle be suppressed by a suitable choice of T .

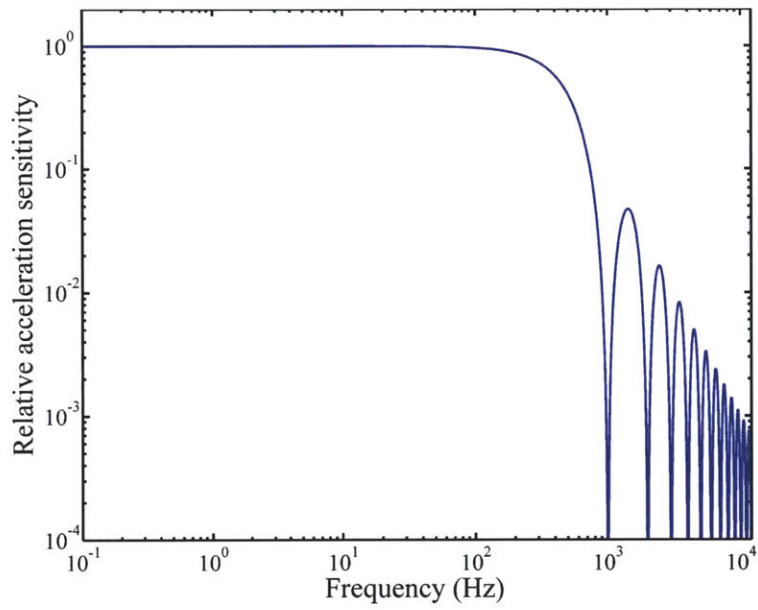


Figure 2-5: Frequency response of a $\pi/2-\pi-\pi/2$ interferometer to acceleration input ($T = 1$ ms). The interferometer is insensitive to acceleration Fourier components with frequencies at multiples of $1/T$, and its sensitivity rolls off as $\sim 1/\omega^2$ at frequencies greater than $1/T$.

Chapter 3

Apparatus

This chapter describes the experimental apparatus developed for investigations of atom interferometry at short interrogation times. A compact vacuum cell was designed for implementing atom cooling and trapping, interferometry, and state detection in a single volume. Conventional laboratory atom interferometers (e.g., [24]) typically use multiple vacuum regions to isolate interferometer interrogations from stray magnetic fields, regions of higher background pressure and sources of scattered light (e.g., the MOT). Practical applications, however, constrain the volume of the vacuum cell and might preclude distinct separation of the trapping, interrogation, and detection sites. A gravimeter with cesium atoms was implemented as a testbed for studying high bandwidth inertial sensor performance, and as a step toward developing more advanced compact inertial sensors.

3.1 Vacuum System

Ultra-high vacuum (UHV) is required to minimize collisions of cold cesium atoms with background (non-cesium) particles, which would reduce the number of atoms in the trap and lead to spurious phase shifts in the interferometer. A compact, octagonal vacuum cell (80 cc), shown in Fig. 3-1, was constructed from a machined quartz frame, and seven 1" and two 2.3" windows were fused to the frame with quartz frits. This allowed fusing to occur at a temperature sufficiently low to prevent significant distortions of the windows, which have a higher softening temperature. Before fusing, the windows were polished to $\lambda/20$ flatness, and maintained flatness to $\lambda/10$ after construction.

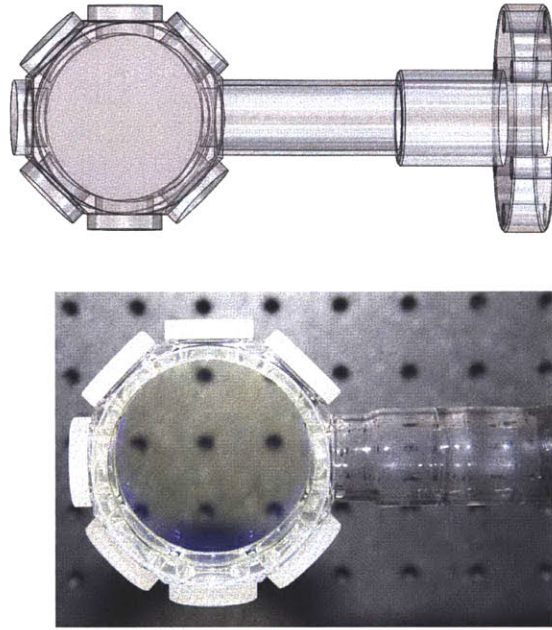


Figure 3-1: Octagonal vacuum cell design and photograph of the finished cell. The diameter of the large windows is 2.3", and 1" for the smaller windows.

The cell accommodates a configuration of three orthogonal beam pairs for laser cooling, two possible axes for Raman beams, a probe beam, and a beam for state preparation (the actual configuration is described in the next chapter). The large windows also provide access for a microwave source and detection optics for measuring laser-induced fluorescence (LIF). All windows are anti-reflection coated, and transmit more than 99.5% of 852 nm laser light. The all-glass design offers several advantages. First, it is effective at reducing scattered light, which can lead to spontaneous emission and systematic phase shifts. In addition, the use of glass avoids stray magnetic fields produced by metal vacuum chambers.

The vacuum cell is initially evacuated with a turbomolecular pump, and the entire vacuum system is baked at 100 – 120°C to minimize outgassing. The vacuum level is maintained at 3×10^{-9} Torr by a 200 L/s getter (SAES CapaciTorr, St 185 Ti-V alloy) and a 2 L/s ion pump. A cesium metal dispenser (SAES, 5.2 mg) controls the cesium background pressure, and emits a directed flux of atoms toward the MOT. For cleanliness, the metal dispenser is baked out while the turbomolecular pump is attached. Initially, 1 A of current is run through the dispenser until the pressure returns to its post-bakeout level. This cycle is repeated at 2 A and 3 A over a period of 24 hours. This preparation process removes hydrogen trapped

in the dispenser cartridge. Efficient loading of the MOT requires a large cesium flux in the cell, but a high background pressure can be detrimental to interferometry for the reasons stated above. The cesium dispenser is located in the nozzle of the quartz cell, about 3" from the MOT. It evaporates cesium through a small slit, which is aligned toward the trapping region to maximize the loading rate. At 3 A, the source depletes the cesium sample over more than one year with daily usage. This current level results in a trap loading rate of $\sim 3 \times 10^7$ atoms/s (the lifetime was ~ 0.3 s). Evaporation is most efficient at over 4.5 A, but operating at this current depletes the sample in under one hour. A higher flux could be produced by adding a 2D MOT, at the cost of extra complexity and size [31].

One of the significant challenges for sensor development is reducing the power required to maintain UHV over a potentially multiple year lifetime. Getter pumps efficiently pump many species after being activated, and use no power until the gettering material surface is saturated and requires reactivation. Unfortunately, getters cannot pump noble gases, so ion pumps must be used additionally. In particular, helium diffusion becomes a major limitation without an ion pump. One potential solution is to use materials with low helium permeability, such as sapphire (the diffusion constant for helium permeation in sapphire has been observed to be at least six orders of magnitude smaller than in other glasses [71]).

3.2 Magnetic Field Control

State preparation, interferometry, and detection require a bias magnetic field in order to define a quantization axis for the atoms. Careful engineering of the field is required, since atom interferometers are sensitive to spatially or time-varying magnetic fields. To reduce the sensitivity of the interferometer to magnetic fields, the atoms are prepared in the first-order insensitive $|F = 3, m_F = 0\rangle$ ground state. The splitting of the $|F = 3, m_F = 0\rangle$ and $|F = 4, m_F = 0\rangle$ ground states used in the interferometer increases with the magnetic field as $\Delta E = \alpha B^2$ where $\alpha = 427$ Hz/G². By contrast, $\Delta m_F \neq 0$ levels split by $\Delta E = \beta m_F B$, where $\beta \approx 700$ kHz/G.

Three orthogonal pairs of magnetic coils, separated at the Helmholtz condition (the coil separation is equal to the coil radius), are tuned to null environmental magnetic fields (Earth and laboratory). A programmable power supply (Agilent N6700B) alternates two vertically-

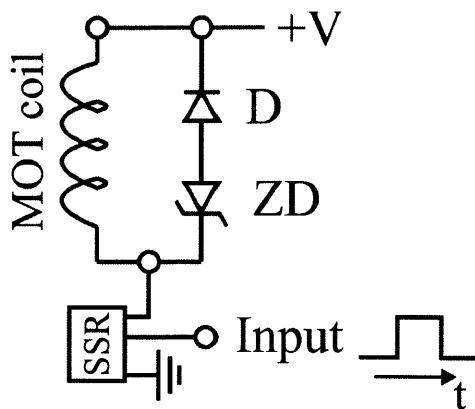


Figure 3-2: Simple circuit used to reduce the MOT coil shutoff time. D = Diode, ZD = Zener diode.

oriented, 12" diameter coils between nulling field and bias field settings. A bias field of 0.8 G lifts the degeneracy of the Zeeman sublevels, and permits driving Raman transitions between the $m_F = 0$ states. The magnitude of the quadratic Zeeman shift is resolved to better than 1 Hz with microwave Ramsey spectroscopy. Since the atoms fall a small distance during the interrogation (several millimeters), no magnetic shielding is used.

To form a quadrupole field for the MOT, two 80 mm diameter anti-Helmholtz magnetic coils are mounted around the vacuum cell. A current of 2.3 A produces a field gradient of ≈ 10 G/cm. A solid state relay switches the MOT coil current on for loading the trap. Additionally, high voltage Zener diodes are installed in parallel to shorten the shut-off time to 100 μ s by dissipating the large back-EMF produced when the relay closes (Fig. 3-2 shows the MOT coil circuit schematic).

3.3 Optical System

Fig. 3-3 depicts the generation of the trapping and detection light on an atomic energy level diagram. Two Toptica TA100 lasers serve as sources for atom trapping, state preparation, and detection. Each laser produces up to 300 mW of fiber-coupled 852 nm light by injecting the output of an external cavity diode laser (≈ 0.5 MHz linewidth) into a tapered amplifier. These lasers are locked by saturated absorption spectroscopy to the cesium $F = 4 \rightarrow F' = 4/5$ and $F = 3 \rightarrow F' = 3/4$ crossover transitions (referred to as the $F = 4$ and $F = 3$ lasers, respectively). Fig. 3-4 shows the optical scheme for locking. A 50/50 beamsplitter splits a

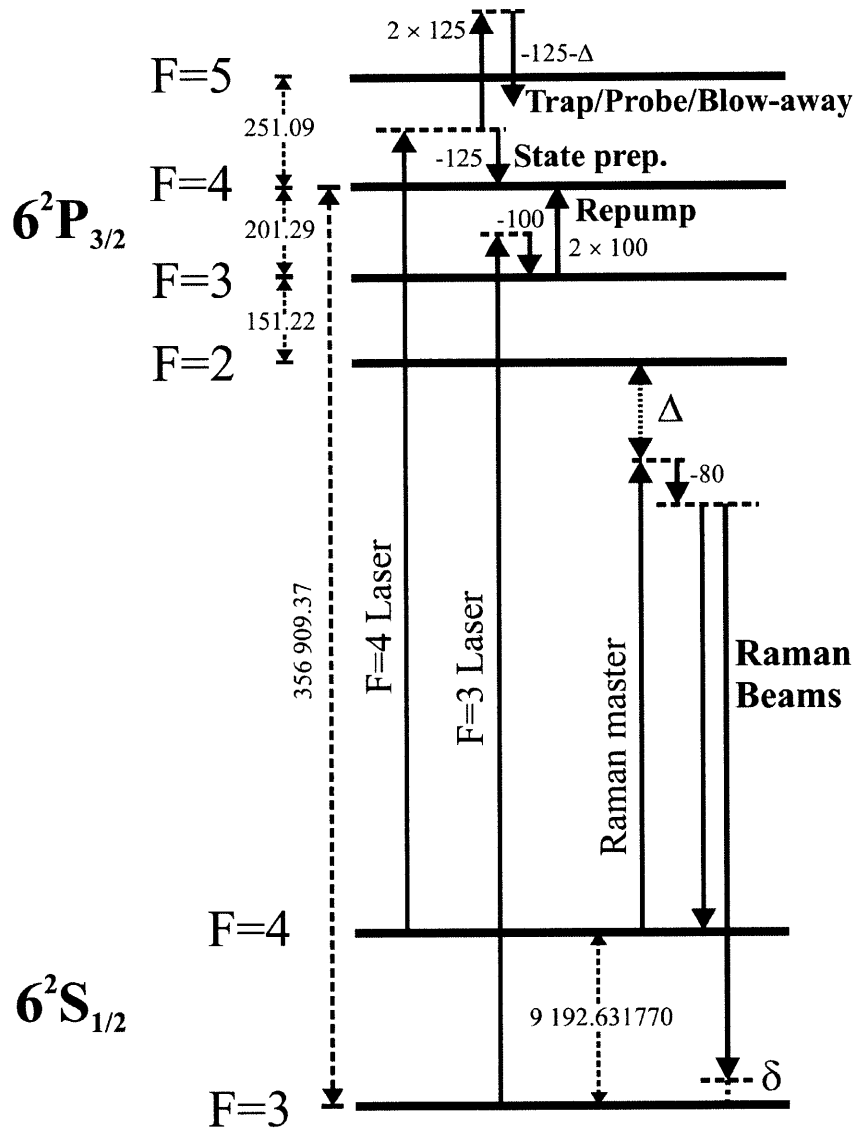


Figure 3-3: Atomic energy level diagram for cesium, with laser frequencies generated by the apparatus. The $F = 4$ and $F = 3$ lasers are locked to the $4'/5'$ and $3'/4'$ crossover resonances, respectively. All numerical values are in units of MHz.

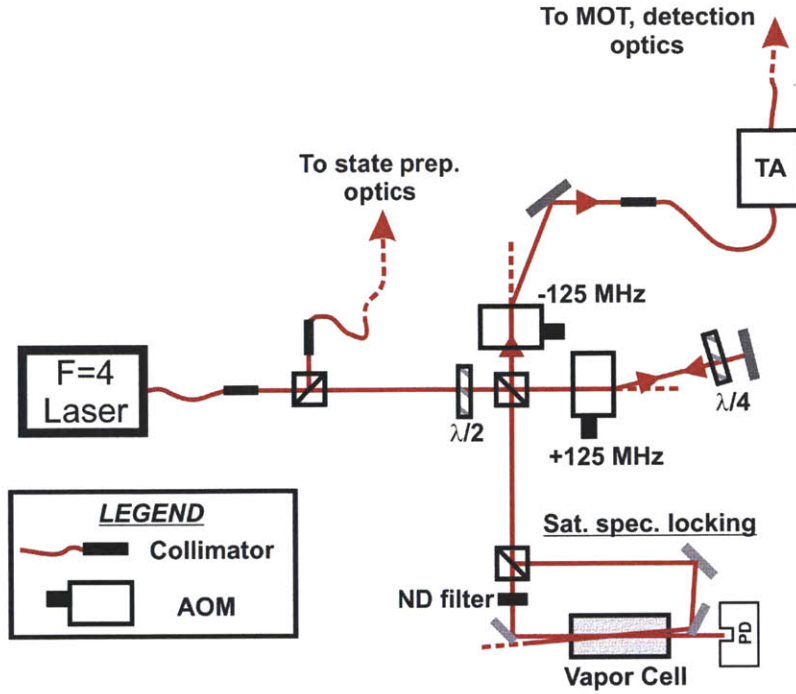


Figure 3-4: Diagram of optics for locking an external cavity diode laser used as a source for driving optical transitions from $F = 4 \rightarrow F' = 4, 5$. The optics for splitting and delivering trapping, state preparation and detection light to the vacuum cell are shown in Figs. 3-5, 3-6.

≈ 1 mW beam into a pump and probe beam, the latter of which is attenuated by an ND filter. These beams are expanded and overlapped in a cesium vapor cell (ThorLabs), and the probe beam is subsequently detected on a photodiode. A lock-in regulator circuit locks the laser to the appropriate peak in the absorption signal by controlling both the grating piezo and the laser current. A similar scheme is used to stabilize the $F = 3$ laser.

Acousto-optic modulators (AOM, Isomet) tune the $F = 4$ laser output to generate frequencies for driving the $F = 4 \rightarrow F' = 5$ cycling transition (trapping) and the $F = 4 \rightarrow F' = 4$ transition (Figs. 3-5, 3-6). The latter frequency is overlapped with repump ($F = 3 \rightarrow F' = 4$) light to optically pump atoms into the $|F = 4, m_F = 0\rangle$ level, which is a dark state to both frequencies when the laser beams are linearly polarized. As mentioned in Section 3.2, $m_F = 0$ states are used for interferometry to reduce magnetic field sensitivity. AOM drive signals are derived from voltage-tunable RF drivers (Isomet), and pulsed with TTL-controlled switches (RF-Lambda, 80 dB isolation). The AOMs provide high optical attenuation (60 dB) and short switching times (100 ns when the beam is focused to a waist in the crystal). By double-passing light through AOMs, the trapping light can be detuned by

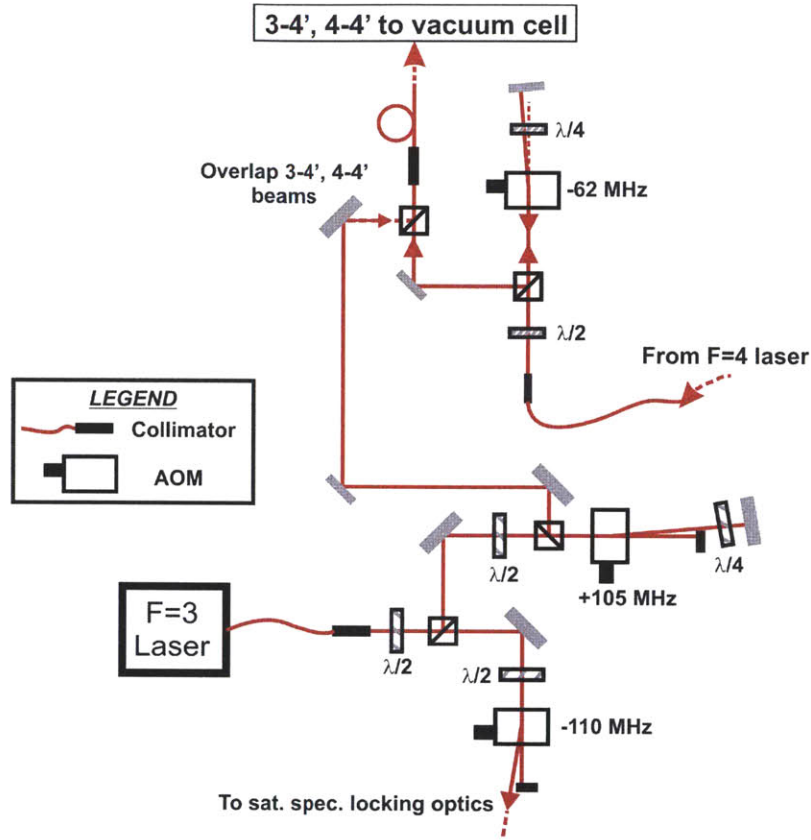


Figure 3-5: Diagram of optics for state preparation. A laser beam resonant with the $F = 4 \rightarrow F' = 4$ transition is overlapped with repump ($F = 3 \rightarrow F' = 4$) light and delivered to the cell. Both beams are linearly polarized, so that atoms are optically pumped into the $|F = 4, m_F = 0\rangle$ level.

>45 MHz for sub-Doppler cooling, while preserving alignment and fiber-coupling efficiency. All of the optical fiber in the system was single mode and polarization maintaining (PM). Chapter 4 discusses the experimental sequence for atom interferometry in more detail.

3.3.1 Tapered Amplifiers

Fiber-coupled laser amplifier modules were constructed to increase the available power for the trapping and Raman beams. Larger atom numbers were achieved with higher trapping beam intensities, and more efficient interferometer pulses required higher Raman beam intensity (see Section 3.5). Tapered amplifiers (TAs) are well-suited to this task because they avail high output power over a broad frequency band and preserve single mode input.

Fig. 3-7 shows the design of the amplifier module, which couples seed light into a tapered

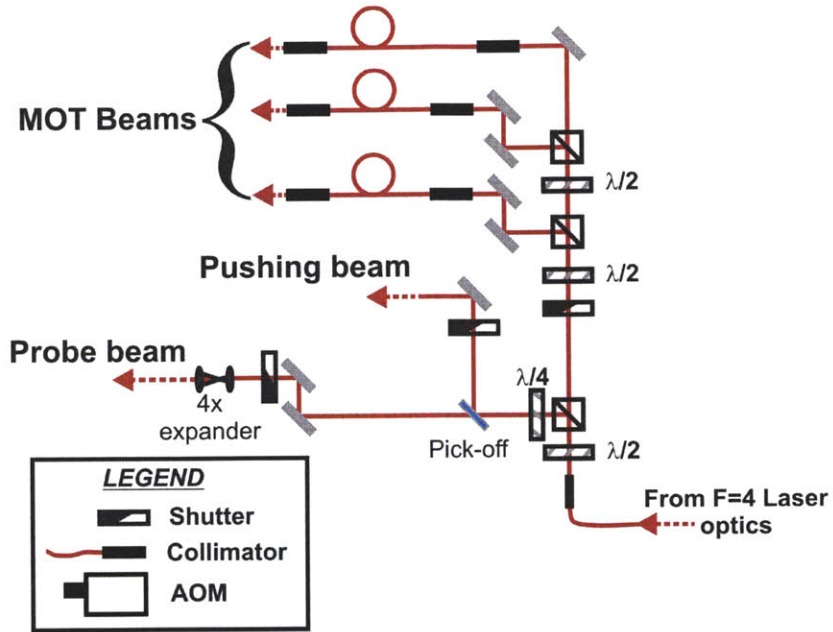


Figure 3-6: Diagram of optics for splitting the trapping light, as well as preparing the probe and pushing beams. The probe beam is expanded to 4 mm before the vacuum cell. The pushing beam is used to push away atoms in $m_F \neq 0$ levels, which are undesirable for interferometry. Since these laser beams derive from the same source (Fig. 3-4), mechanical shutters select which beams reach the atoms.

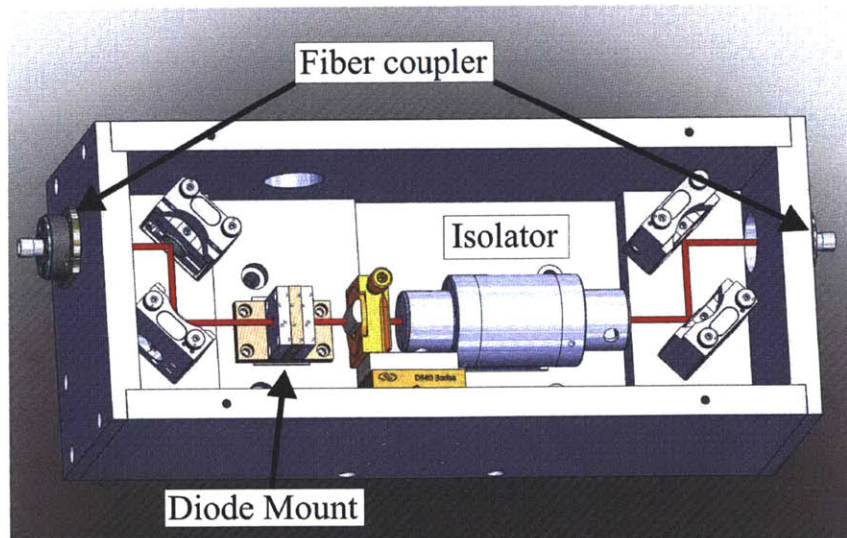


Figure 3-7: Design for the tapered amplifier modules. Two of these modules were used to amplify the trapping light and the Raman beam.

diode (Eagleyard Photonics, EYP-TPA-0850-01000-4006-CMT04) and fiber-couples the amplified output. With 10-15 mW of seed power to saturate the diode, the TA produces up to 1 W of optical power at 852 nm with a drive current of 2.7 A. The diode amplifies light over a 26 nm band centered at 850 nm. An aspheric and cylindrical lens circularize the output beam before coupling it into a PM fiber (OFR FiberPorts fiber-coupled the input and output beams). By fiber-coupling, a module can be conveniently installed in the optics train. Furthermore, since the mode of amplified spontaneous emission (ASE) from the diode is broader than the amplified output mode, the fiber-coupling optics effectively spatial filter it. To prevent backward amplification of back-reflected light, which can damage the diode [72], a 38 dB isolator (OFR IO-3-850-HP) is installed before the output coupler. A drive current of 2 A produces 400 mW of fiber-coupled light with <1 mW of broadband ASE. A 5 A current controller (Wavelength Electronics PLD5K-CH) provides a switchable drive current for the diode.

After amplification, the trapping light is split into three separate beams, and coupled back into fibers, as shown in Fig. 3-6. These beams are delivered to the cell via cage-mounted optics (ThorLabs) (Fig. 3-8), which provide high pointing stability and reduce the need for frequent realignment. The trapping beams are collimated to a 1 cm diameter ($1/e^2$) with an intensity of ≈ 10 mW/cm². Each beam is circularly polarized by a polarizer and $\lambda/4$ waveplate. After the cell, another $\lambda/4$ waveplate and mirror retroreflects the trapping beams with opposite helicity. The coldest temperatures are achieved, however, with slightly misaligned retroreflections. Optimal alignment is accomplished by maximizing the MOT size with perfect retroreflections, and then making small adjustments to the retroreflections by trial and error. Since the probe beam for atom state detection is derived from the same source as the trapping light, mechanical shutters serve to select which beam is delivered to the atoms (the characteristics of the probe beam and LIF detection optics are discussed in Section 4.3).

3.4 Control Electronics

A National Instruments PXI-1042Q real-time embedded controller manages data acquisition, the RF switches for the AOMs, the mechanical shutters, tuning of the AOM driver frequen-

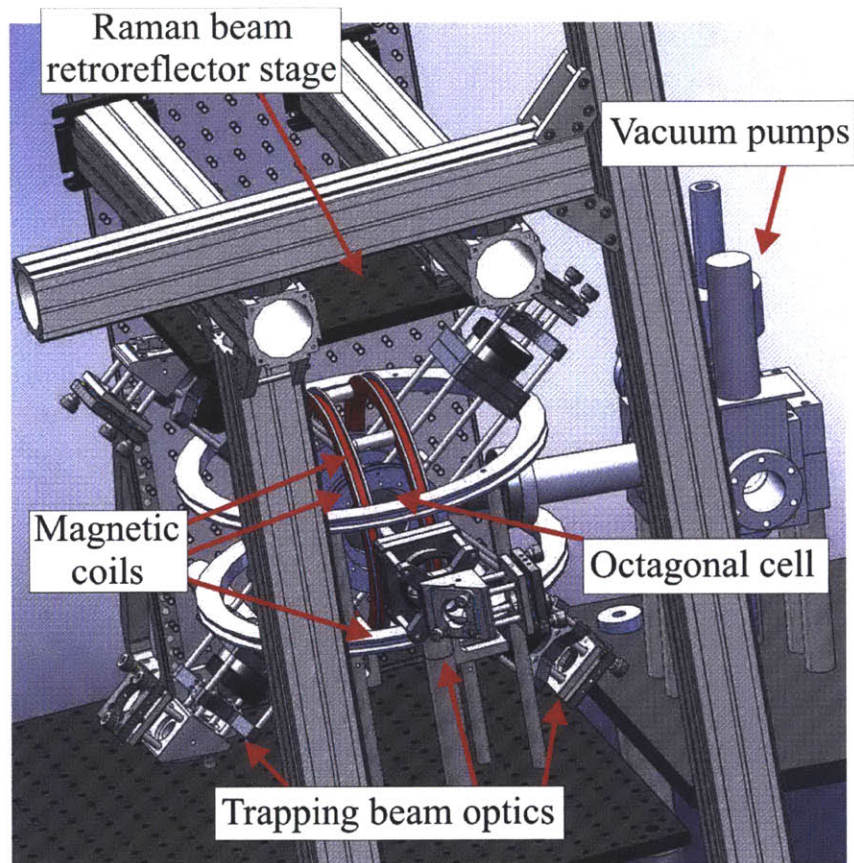


Figure 3-8: Design of vacuum cell mount with trapping beam optics, magnetic coils (MOT and nulling) and Raman retroreflector stage. The breadboard supporting the vacuum pumps is tilted 5° relative to the table surface in order to prevent the formation of standing waves in the Raman beam.

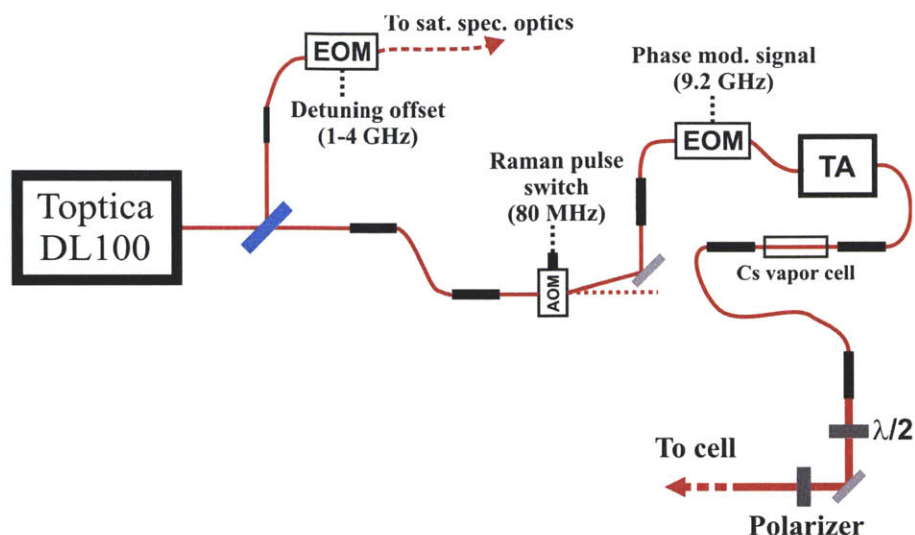


Figure 3-9: Diagram of optics for generating the Raman beams. The RF circuit for the phase modulation signal and AOM drive signal is shown in Fig. 3-11.

cies, and timing for the experimental sequence. The data acquisition and digital/analog output cards share a common 10 MHz clock reference (Spectracom 9383). The experimental sequence is programmed in LabVIEW and executes with $< 10 \mu\text{s}$ timing jitter. Since much more precise timing is required for the interferometer pulses, a 15 bit, 625 MS/s arbitrary waveform generator (AWG, Agilent N8241A) handles Raman and microwave pulse timing (the interferometer sequences are only triggered by a digital I/O card in the PXI chassis). Raman pulse and microwave frequency generation is discussed below. A separate laptop serves as a host for data storage, running LabVIEW, and programming the AWG in MATLAB.

3.5 Raman Beam Generation

The Raman beams are used for interferometry as well as velocity selection in the experiments. Fig. 3-9 shows the optical layout for generating the Raman beam frequencies. A distributed feedback laser (Toptica DL100) emitting at 852 nm with a 1 MHz linewidth serves as the master laser. This laser is offset-locked from the cesium D2 line by picking-off light from the laser output and phase-modulating it in an EOM (EOSpace PM-0K5-10-PFA-PFA-850) to produce sidebands at the offset frequency. The laser is locked via saturated absorption spectroscopy to a cesium transition in the absorption profile corresponding to one of the

sidebands. Typically, the detuning is set to $\Delta \approx -1$ GHz from the $F = 4 \rightarrow F' = 2$ frequency, in order to maximize interferometer contrast. A smaller laser detuning increases the effective Rabi frequency but also increases the rate of spontaneous emission. A higher Rabi frequency improves transfer efficiency because a larger velocity distribution of atoms is addressed (the bandwidth of a Raman pulse is $\approx \Omega_{\text{eff}}$). An 80 MHz AOM serves as a switch for the Raman beam by coupling the first diffracted order into a fiber (the RF signal for this AOM is produced by the AWG for precise timing). A fiber-coupled EOM (Photline NIR-MPX800-LN-08) phase-modulated the beam at the cesium hyperfine splitting frequency ($\omega_{HF} \approx 9.2$ GHz) to produce sidebands for driving Raman transitions. The RF signal driving the EOM also realized phase-shifting and frequency sweeping capabilities for interferometry. The generation of this signal is described in Section 3.5.1. The phase-modulated beam is then amplified by a TA, in order to produce short interferometer pulses. To minimize spontaneous emission and AC Stark shifts produced by near-resonant ASE, the TA output is filtered in a separate cesium vapor cell before being sent to the vacuum cell.

The Raman beam is collimated to a diameter of 5 or 10 mm ($1/e^2$) and polarized by a high extinction ratio (>80 dB) linear film polarizer (ThorLabs LPVIS). A pure polarization ensures that spurious Doppler insensitive transitions, which require $\sigma^+ - \sigma^+$ polarizations, are not driven. To drive Doppler sensitive transitions, the Raman beam is retroreflected through a $\lambda/4$ waveplate above the vacuum cell so that the counter-propagating beams have lin. \perp lin. polarizations. To prevent the formation of standing waves from back-reflections occurring at the upper window of the cell, the vacuum cell is mounted at an angle of 5° relative to the vertical Raman beam axis¹.

This retroreflected beam configuration offers several advantages for interferometry. By phase-modulating a single laser beam, any phase introduced by the optics prior to reaching the atoms is common mode to both frequencies, so it does not contribute to a differential phase shift. Secondly, since both frequencies and circular polarizations are present in the counter-propagating beams, Raman transitions with opposite propagation directions $\pm \mathbf{k}_{\text{eff}}$ can be selectively excited. If the atoms have a non-zero velocity along the Raman beam, the two resonances are separated by Doppler shifts of opposite signs. This allows excitation of Raman transitions along either propagation direction by simply changing the laser frequency

¹The cell was originally mounted without the tilt, and lower Raman pulse transfer efficiency was observed.

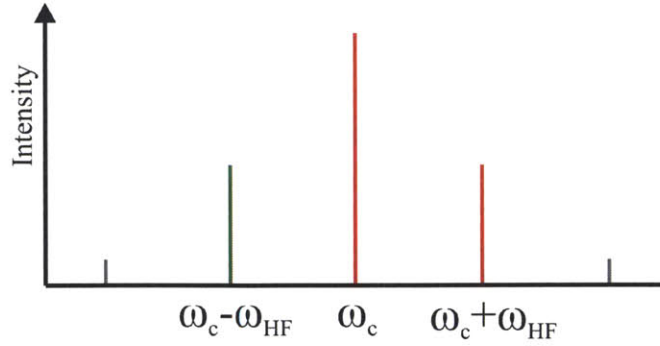


Figure 3-10: The Raman beam spectrum produced by phase modulation with an EOM. Optical frequencies ω_c and $\omega_c + \omega_{HF}$ (red) contribute the largest effective Rabi frequency. The symmetric pair of frequencies, ω_c and $\omega_c - \omega_{HF}$ (green), produce interference with the coherent population transfer of the dominant frequencies (Eq. 3.1).

difference. As Chapters 5 and 6 discuss, propagation direction reversal enables suppression of systematic light-based phase shifts, as well as a method for large area interferometry with Raman pulses.

Since one of the Raman frequencies must propagate to the retroreflecting mirror and back to the atoms, the effective laser phase $\phi_{\text{eff}} = \phi_1 - \phi_2$ is defined relative to the position of the mirror (the mirror surface is flat to $\lambda/20$ in order to minimize phase front distortions). Thus, the position of the mirror along the input axis needs to be stable over the duration of the interferometer sequence. Mirror motion $z(t)$ contributes an overall phase shift $\Delta\phi_{\text{mirror}} \approx k_{\text{eff}} [z(t_0) - 2z(t_0 + T) + z(t_0 + 2T)]$. In the apparatus, the mirror is mounted on an optical breadboard supported by large, rigid posts. Noise introduced by mirror vibrations is discussed in Section 2.3.

A disadvantage of using a single phase-modulated beam is that optical power is distributed amongst other sidebands that do not significantly contribute to population transfer, due to large detuning. Moreover, other sideband pairs separated by ω_{HF} produce interfering population transfer [73]. As the Raman beam spectrum in Fig. 3-10 shows, optical frequencies ω_c and $\omega_c + \omega_{HF}$, and $\omega_c - \omega_{HF}$ and ω_c are both Raman resonant. Since the spectrum of a phase-modulated beam is symmetric, the single-photon Rabi frequencies of the ± 1 sidebands are equal. The effective Rabi frequency for the farther detuned pair is lower by a factor of $\Delta/(\Delta + \omega_{HF}) \approx 1/10$ for $\Delta \approx -1$ GHz.² Since the EOM is operated in

²In Chapter 5, ω_c is locked to a detuning of +3.5 GHz from the $F = 4 \rightarrow F' = 5$ transition. In this case, the Rabi frequencies are different only by a factor of ≈ 2 , and both pairs contribute significantly.

the weak phase modulation limit (far from suppression of the carrier frequency), the effect of higher-order sidebands can be neglected. Analysis in [74] derives the effective Rabi rate for the combination of the three dominant optical frequencies

$$\Omega_{\text{eff}} = \sqrt{\Omega_{c,+1}^2 + \Omega_{c,-1}^2 + 2\Omega_{c,+1}\Omega_{c,-1} \cos(\Delta\theta)} \quad (3.1)$$

where $\Omega_{c,\pm 1}$ is the standard two-photon Rabi frequency for frequencies ω_c and $\omega_c \pm \omega_{HF}$, and $\Delta\theta$ is the difference phase of the fields $\Delta\theta \equiv \phi_{-1}^0 + \phi_{+1}^0 - 2\phi_c^0$. For phase-modulated fields $\Delta\theta = \pi$, so the two Raman processes destructively interfere, reducing the effective Rabi frequency. Moreover, a retroreflected, phase-modulated beam also forms to a spatially-modulated Rabi frequency, with a period of $\lambda_{\text{microwave}}/2$, where $\lambda_{\text{microwave}} = 2\pi c/\omega_{HF} \approx 3.3$ cm [34]. This effect leads to dephasing and pulse length errors if the atoms are displaced a significant fraction of $\lambda_{\text{microwave}}$ during the interrogation (e.g., while operating in a dynamic environment); in this work, however, it does not contribute significantly for the small displacements accrued over drop times of <25 ms.

3.5.1 Microwave Frequency Generation

Microwave frequencies at around the cesium ω_{HF} are generated for driving the Raman EOM and a microwave antenna. As Fig. 3-11 shows, the Raman EOM signal derives from a single sideband mixer (Polyphase SSB90110A) that mixes a constant 9.2 GHz signal from an Agilent E8257D signal generator with a dynamic ~ 30 MHz signal from the AWG (Agilent N8241A). The E8257D has a phase noise specification of -114 dBc/Hz, at an offset of 10 kHz. The intermediate frequency band covers 10-50 MHz. Spurious frequency components produced by mixing are suppressed by >27 dB. The laser frequency difference is given by

$$\Delta\omega(t) = f_{E8257D} + f_{N8241A}(t) \quad (3.2)$$

The signal is then amplified to $\approx 16 - 24$ dBm for driving the EOM. The RF amplitude is chosen to produce the intensity ratio in the Raman beam frequencies that cancels the differential AC Stark shifts of the $|F = 3, m_F = 0\rangle$ and $|F = 4, m_F = 0\rangle$ levels. This signal can be programmed for phase-continuous frequency sweeps and discrete phase shifting, which

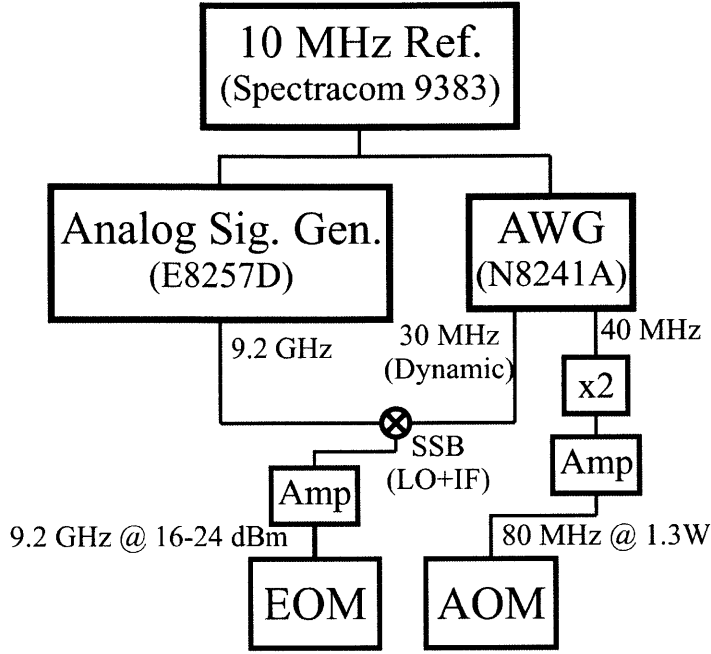


Figure 3-11: Diagram of the circuit for generating the microwave frequencies for the Raman EOM and AOM signals. The single sideband mixer adds the base 9.2 GHz signal (f_{E8257D}) with the dynamic signal from the AWG [$f_{N8241A}(t)$], providing frequency sweeping and phase shifting capabilities.

are useful for scanning through interference fringes.

In state preparation, a microwave antenna (Narda WR90) transfers atoms between the $m_F = 0$ ground state levels, and is also used for microwave interferometry. An IFR 2042 signal generator produces a 4.6 GHz signal that is doubled to the cesium ω_{HF} , and then is amplified by a narrowband RF amplifier (Microwave Power L0809) to 35 dBm. Positioned $\approx 3''$ from the atoms, the antenna produces a π pulse with a duration of 110 μ s. A high isolation (>70 dB) RF switch controls the microwave pulse timing. High isolation is important because leakage power can coherently transfer population during the interferometer, leading to systematic phase shifts. Finally, the IFR 2042 and Agilent E8257D signal generators, as well as the AWG, shared a common 10 MHz reference (Spectracom 9383, a rubidium-locked crystal oscillator with GPS corrections).

THIS PAGE INTENTIONALLY LEFT BLANK

Chapter 4

Short Interrogation Time Atom Interferometry

This chapter presents a demonstration of a cold atom gravimeter with short interrogation times ($2T < 15$ ms). The operation of the interferometer in a compact vacuum cell is described in detail, from state preparation to detection, and a summary of the performance of the system is given. High contrast interference fringes were observed at these short interrogation times, and limitations to achieving higher contrast are discussed.¹

4.1 Atom Trapping and State Preparation

The measurement sequence begins by loading cesium atoms from a thermal vapor into a MOT. A diagram of the vacuum cell with trapping and Raman beams is shown in Fig. 4-1. Three orthogonal, counter-propagating laser beams are detuned by -2.5Γ from the $F = 4 \rightarrow F' = 5$ cycling transition ($\Gamma = 2\pi \times 5.23$ MHz, see table in Appendix A for other cesium data). Each beam is 1 cm in diameter ($1/e^2$) and has an intensity of $\approx 10I_{\text{sat}}$, where $I_{\text{sat}} = 1.10$ mW/cm² is the saturation intensity for the cycling transition. After loading $\sim 10^7$ atoms over a period of 500 ms (with a loading rate of $\sim 3 \times 10^7$ atoms/s), the magnetic field is shut off and the detuning of the trapping beams is increased to -8Γ for sub-Doppler cooling. The trapping beam intensity is stepped down to $\approx 10\%$ over 5 ms and then switched off. The

¹This chapter is based on Butts *et al.*, “Light pulse atom interferometry at short interrogation times,” in *Journal of the Optical Society of America B* **28**, 416-421 (2011) [75].

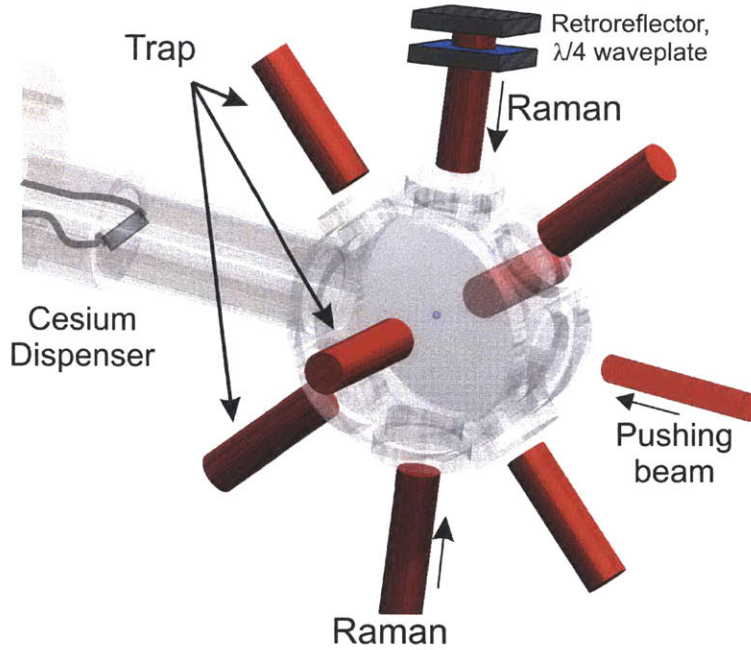


Figure 4-1: Vacuum cell with the configuration of laser beams for trapping and interferometry. The Raman beams are oriented vertically for gravimetry. The cesium dispenser is located in the nozzle of the vacuum cell, so that it provides a direct flux of atoms to the trapping volume. The probe beam (not shown) uses the same axis as the Raman beams, but is tilted slightly from vertical.

far-detuned molasses cools the atoms to $\approx 5 - 6 \mu\text{K}$. Doppler sensitive Raman transitions measure the final temperature in a separate measurement. Finally, the repump light remains on for 1 ms to ensure atoms are distributed in the $F = 4$ manifold.

As discussed in Chapter 3, only the magnetically-insensitive $m_F = 0$ sublevels in $F = 4$ and $F = 3$ are used for interferometry. To increase the population in $m_F = 0$ sublevels, the vertical bias coils apply a 0.8 G bias field to lift the degeneracy of the Zeeman sublevels, and define a quantization axis. A $100 \mu\text{s}$ optical pumping pulse with resonant $F = 4 \rightarrow F' = 4$ and $F = 3 \rightarrow F' = 4$ laser light places $\sim 80\%$ of the atoms in the $|F = 4, m_F = 0\rangle$ level, which is a dark state to both beams since they are linearly polarized (along the quantization axis). This step slightly heats the ensemble to $\approx 5 \mu\text{K}$, but increases the atom count in the desired level by a factor of seven. To select atoms in the $m_F = 0$ level, a $120 \mu\text{s}$ microwave π pulse drives atoms from $|F = 4, m_F = 0\rangle$ to $|F = 3, m_F = 0\rangle$. Alternatively, a Doppler sensitive Raman pulse can transfer atoms to $|F = 3, m_F = 0\rangle$ to select an ensemble with near-recoil temperatures ($T_r \approx 200 \text{ nK}$ for cesium) along the Raman beam axis, at a cost

of lower atom number. By selecting a population with a temperature of $0.5 \mu\text{K}$, about 10% of the atoms from the MOT remain. All of the atoms in $m_F \neq 0$ states do not make a transition, and stay in the $F = 4$ manifold. At this point, a horizontal pushing beam, resonant with the $F = 4 \rightarrow F' = 5$ transition, is pulsed for $500 \mu\text{s}$ to accelerate them out of the interrogation region. Far-detuned $F = 4 \rightarrow F' = 4$ transitions distribute $< 0.5\%$ of the atoms in the $F = 3$ manifold, so that they remain visible at detection (this only contributes a small background signal).

This state preparation sequence produces a free-falling ensemble of up to $\sim 10^7$ atoms in the $|F = 3, m_F = 0\rangle$ level (with velocity selection, the atom number is further reduced by $\sim 10\times$).

4.2 Interferometry

The gravitational acceleration of the atoms in free fall is measured with a $\pi/2 - \pi - \pi/2$ interferometer. The Raman beam is aligned to local vertical to within 0.3° , using a plumb bob as a reference. The actual acceleration measured by the interferometer is $\hat{k}_{\text{eff}} \cdot g = g \cos \theta$, where θ is the angle from vertical and \hat{k}_{eff} is the unit vector for the propagation axis of the Raman beam. To ensure that the Raman resonance condition is satisfied during all three pulses, the laser frequency difference is swept to cancel the Doppler shift of the accelerating atoms, as shown in Fig. 4-2. The Doppler shift increases at a rate $\alpha = k_{\text{eff}}g \approx 2\pi \times 23 \text{ kHz/ms}$. Figure 4-3 shows two oppositely Doppler-shifted Raman resonances after a drop time of 12 ms; as noted earlier, the retroreflected Raman beam can excite Raman transitions along opposite \mathbf{k}_{eff} . Either may be selected for interferometry as long as the separation of the resonances is greater than the Rabi frequency, which determines the width of the resonances.

The Raman laser detuning is typically set at $\Delta = -1.25 \text{ GHz}$ from the $F = 4 \rightarrow F' = 2$ frequency. Smaller detunings allow for shorter Raman pulses, but also increase the rate of spontaneous emission. Contrast was found to be maximized with π pulse durations $\approx 8 - 10 \mu\text{s}$. With velocity selection, a π pulse transfers $\sim 85\%$ of the atoms, since the bandwidth of the pulse is broader than the velocity distribution of the atoms. Contrasts up to 70% were observed. Using hotter atoms leads to greater variation in pulse area across the ensemble, and therefore higher dephasing. While the availability of higher laser power from

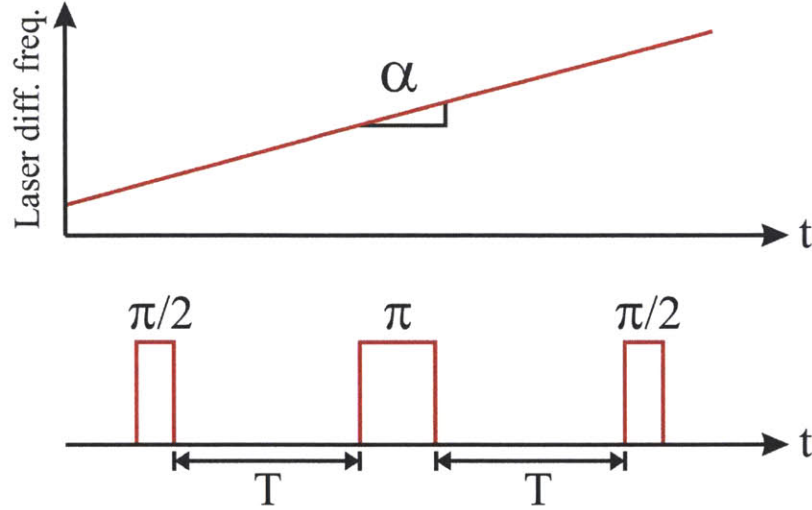


Figure 4-2: Interferometer pulse timing diagram. The laser frequency difference is chirped by $\alpha/2\pi \approx 23$ kHz/ms continuously to maintain resonance in all three pulses.

the tapered amplifiers could further reduce the pulse durations, Rabi frequencies greater than 100 kHz begin to drive Raman transitions along both propagation directions simultaneously, leading to extra interferometer loops that reduce contrast. Launching the atoms with moving molasses could provide for increased separations and use of higher Rabi frequencies.

To produce interference fringes, such as those shown in Fig. 4-4, the phase of the third Raman pulse is scanned. The dynamic RF signal driving the Raman EOM enables both frequency sweeping and discrete phase shifting (see Section 3.5.1). As derived in Section 2.2.2, the gravitational phase shift is canceled for all T when the chirp rate is tuned to compensate for the linearly-increasing Doppler shift, providing a measurement of gravity:

$$g = \frac{\alpha}{|\mathbf{k}_{\text{eff}}|} \quad (4.1)$$

To ensure an accurate fringe count, T is initially set to several values less than 1 ms, and the chirp rate is adjusted to null the small inertial phase shifts. The interrogation time can then be increased to the desired duration.

Another step in the preparation for a gravity measurement is the cancellation of the differential AC Stark shift of the $F = 3$ and $F = 4$ ground state levels, in order to avoid systematic phase shifts. The differential AC Stark shift is nulled by tuning the ratio of intensities in the Raman fields with the RF amplitude driving the EOM. To calibrate the

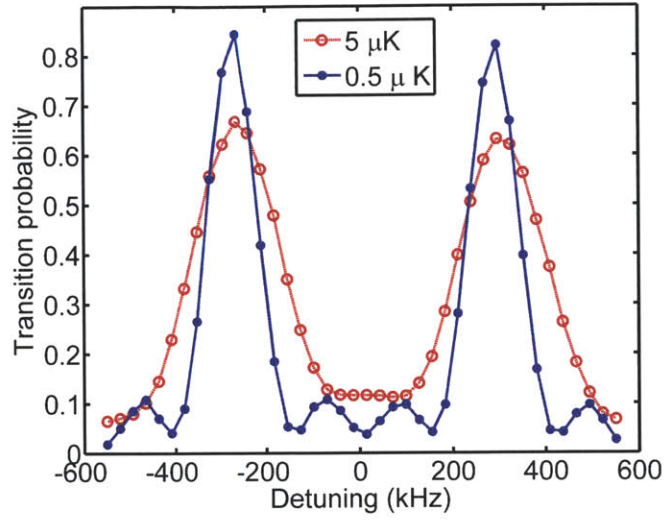


Figure 4-3: Detuning scans for atom samples with $\approx 5 \mu\text{K}$ and $\approx 0.5 \mu\text{K}$ temperatures. The colder sample exhibits less broadening and more clearly defined features. The two resonances correspond to opposite \mathbf{k}_{eff} , which occur because both Raman frequencies are present in the Raman beam retroreflection.

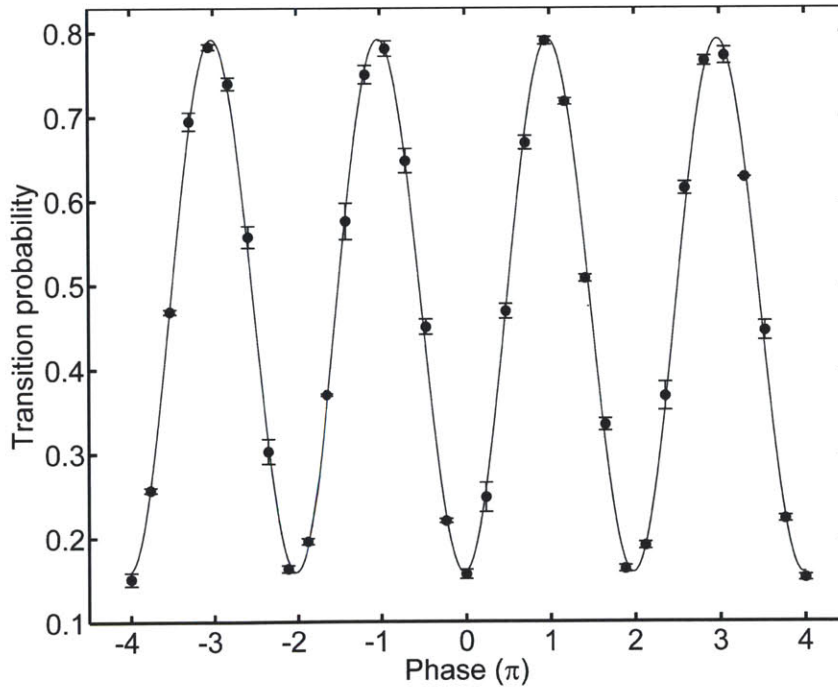


Figure 4-4: Interference fringes for $T = 1 \text{ ms}$. Each point is an average of three shots.

shift, a microwave $\pi/2 - \pi/2$ interferometer is tuned so that atoms are placed in a balanced superposition, and a Raman pulse is inserted between the microwave pulses. To suppress coherent transfer, the Raman detuning is set to several MHz (the AC Stark shifts, however, are not significantly altered). For the duration of the Raman pulse, the AC Stark shift introduces a temporary detuning, resulting in a phase shift proportional to the pulse length. The differential shift is canceled when the optically-induced phase shift is nulled for a range of pulse lengths.

The next section describes the method for measuring interferometer phase by state detection. Analysis of a gravity measurement with the apparatus is discussed in Section 4.4.

4.3 State Detection

At the output of the interferometer, the atoms are in a superposition of the $F = 3$ and $F = 4$ hyperfine ground states, corresponding to the populations in the two interferometer output ports. The interferometer phase $\Delta\phi$ is extracted from these populations by measuring the fraction of atoms in $F = 4$ as a function of the scanned laser phase $\Delta\phi^0$:

$$P = \frac{1}{2} - \frac{C}{2} \cos(\Delta\phi + \Delta\phi^0) \quad (4.2)$$

where $C = (P_{max} - P_{min})/(P_{max} + P_{min})$ is the contrast, P_{max} and P_{min} are the observed maximum and minimum $F = 4$ populations (at a net phase of 0 and π , respectively), and P is the transition probability.

The method for state detection in this experiment is normalized laser-induced fluorescence. A vertical probe beam is tuned to the $F = 4 \rightarrow F' = 5$ cycling transition is pulsed for 500 μs to measure the $F = 4$ population. The probe beam is 5 mm in diameter and has an intensity of $2.5I_{\text{sat}}$. To balance the scattering force, the beam is retroreflected and tuned slightly to the red of resonance ($\Delta \approx -1$ MHz). Approximately 1.5% of the fluorescence from the atoms is collected by a 1" lens (f=37.5 mm) at a distance of 2f from the atoms, and imaged on a photodetector positioned another 2f beyond the lens (1:1 imaging). The integrated photodetector voltage, V_4 , provides a measure of the $F = 4$ population.

After measuring the population in $F = 4$, the probe beam is tuned to the blue of the

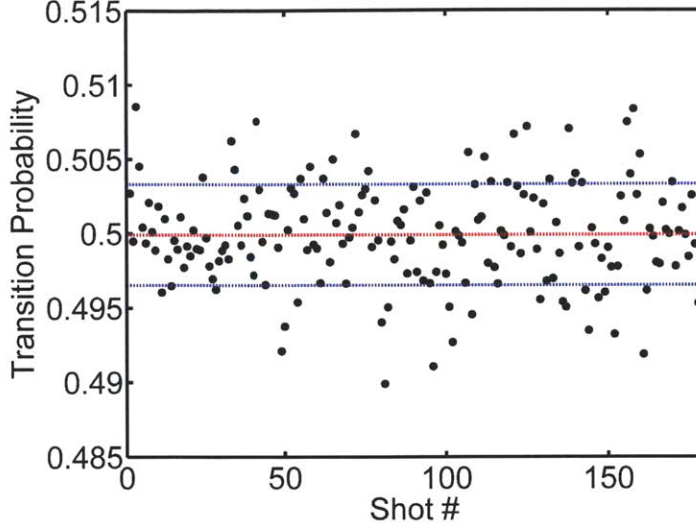


Figure 4-5: Measurement of detection SNR with a Doppler insensitive $\pi/2 - \pi/2$ clock sequence ($T = 0.5$ ms). The phase SNR is 140.

$F = 4 \rightarrow F' = 5$ transition and pulsed for $500 \mu\text{s}$ to push the $F = 4$ atoms out of the detector field of view. Finally, a repump pulse places the $F = 3$ atoms in the $F = 4$ manifold, after which another $F = 4 \rightarrow F' = 5$ pulse measures the population as signal V_3 . The estimate of the transition probability is therefore

$$\hat{P} = \frac{V_4}{V_4 + V_3} \quad (4.3)$$

By normalizing, the readout is insensitive to fluctuations in the total atom number from shot to shot. Normalization is improved by blowing away the $F = 4$ atoms, and separately measuring the two populations; alternatively, one population could be measured, followed by a measure of the total population. Normalization errors can easily occur in the latter case if some of the $F = 4$ atoms are scattered out of the field of view by the first probe pulse.

The detection SNR was measured with a Doppler insensitive Raman $\pi/2 - \pi/2$ clock sequence. The laser frequency difference was tuned such that the atoms were in an equal superposition of the two ground states ($\Delta\phi = \pi/2$), with the pulse separation set to $T = 500 \mu\text{s}$. The noise in the population measurement, $\sigma_{\Delta P}$ is related to the phase SNR, $1/\sigma_{\Delta\phi}$, by

$$\sigma_{\Delta\phi} \approx \left| \frac{\partial(\Delta\phi)}{\partial P} \right|_{\Delta\phi=\pi/2} \times \sigma_{\Delta P} = \frac{2}{C} \sigma_{\Delta P} \quad (4.4)$$

using the result in Eq. (4.2) and propagation of uncertainty. The measured phase SNR was 140 per shot, corresponding to a phase sensitivity of 7 mrad per shot.

The primary SNR limitation of this readout is the frequency and amplitude stability of the probe beam. The probe beam intensity is stable to $\approx 0.3\%$ from shot to shot. The dominant noise source, however, is frequency jitter, since the populations in the two states are not measured simultaneously. For example, consider a laser linewidth of 0.5 MHz and a probe beam intensity of $2.5I_{\text{sat}}$. The photon scattering rate fluctuates by $\approx 0.8\%$ if the laser is tuned to resonance. Assuming the fluctuations between detection pulses are uncorrelated, the SNR is limited to ≈ 170 . In previous work, simultaneous fluorescence detection, which is less sensitive to these fluctuations, has achieved $\text{SNR} \sim 800$, which is near or at the shot-noise limit for many atom interferometry experiments [76]. However, this approach typically involves spatially-separating the two populations so they can be simultaneously imaged, relying upon the high velocity of atoms at the bottom of an atomic fountain (one population is ‘stopped’ by a resonant beam while the other continues to fall). In a brief interrogation where the atoms are not launched by moving molasses, sufficient separation is difficult to achieve. One possible solution is to split the probe beam with a high frequency AOM driven at half the hyperfine splitting frequency. The -1 and +1 diffracted orders would be used to excite the $F = 4 \rightarrow F' = 5$ and $F = 3 \rightarrow F' = 2$ transitions, so both populations could be measured simultaneously on separate detectors by absorption imaging (a similar method was used to generate Raman beams in [77]).

4.4 Gravity Measurement

A gravity measurement provided a characterization of the acceleration sensitivity of the apparatus. The total fringe number was accounted for by scanning the interrogation time (T), and calibrating the chirp rate of the Raman laser frequency difference to cancel the inertial phase shift. The chirp rate was then fixed and the interferometer phase was set to mid-fringe ($\Delta\phi = \pi/2$) by shifting the phase of the third pulse. Data was acquired for 11 hours at a repetition rate of 1.7 Hz, with an interrogation time of $T = 3.5$ ms (the remaining time was for loading the MOT).

In principle, one could measure the precision of the gravity measurement by computing

the standard deviation over the entire data sample. For long samples, however, instabilities in the apparatus lead to a diverging sample standard deviation as the number of measurements increases, making this statistic ill-defined. The sensitivity and stability of the system were instead characterized by computing the Allan deviation, $\sigma_g(\tau)$, where τ is the measurement averaging interval. The Allan variance ($\sigma_g^2(\tau)$) for equally-spaced measurements of g , $\{g_n\} = \{g(t_n)\}$ is defined as²:

$$\sigma_g^2(\tau) = \frac{1}{2} \left\langle \left(\sum_{j=0}^{N-1} \frac{g_{n+j}}{N} - \sum_{j=N}^{2N-1} \frac{g_{n+j}}{N} \right)^2 \right\rangle \quad (4.5)$$

where $\tau = N\delta t = N(t_n - t_{n-1})$. Since the statistic is defined over a fixed measurement interval, the statistic is always well-defined. Purely white, uncorrelated noise in the measurements should average as $\sim \tau^{-1/2}$, so quoting a sensitivity in terms of velocity random walk ($\sim g/\sqrt{\text{Hz}}$) is identified by the occurrence of such a trend in a plot of σ_g versus τ . Instabilities can also be characterized by trends in the Allan deviation as a function of τ . For instance, an acceleration random walk manifests as a trend $\sim \tau^{1/2}$. The bias stability of the measurement is typically taken to be the minimum value of the Allan deviation (in units of g).

Fig. 4-6 shows the Allan deviation calculated from the full sample, in units of μg . The short term sensitivity is measured to be $\approx 120 \mu g/\sqrt{\text{Hz}}$, and averages down to $6 \mu g$ at about 750 seconds. Based on the phase SNR calculated in the previous section, however, one infers a sensitivity of $4 \mu g/\sqrt{\text{Hz}}$, a factor of 30 lower than the observed noise density. The dominant source of noise is high frequency vibrations of the platform from floor vibrations and ambient acoustic noise. To diagnose this, similar gravity measurements were made with different interrogation times ($T = 3, 3.1, 3.25$ ms). Fig. 4-7 shows that, despite the variation in scale factor, the noise statistics in units of g are nearly identical, indicating that the interferometer is in fact measuring real motion. It is worth noting that one would not expect a velocity random walk process to result from platform motion (i.e., the table height does not undergo a random walk). It is likely that the observed $\sim \tau^{-1/2}$ averaging is a consequence of measuring vibrations with a low sampling rate. While the interferometer responds to motion at many of the vibrational frequencies (10-200 Hz, which are within the $< 1/T$

²The Allan variance is also referred to as the two-sample variance.

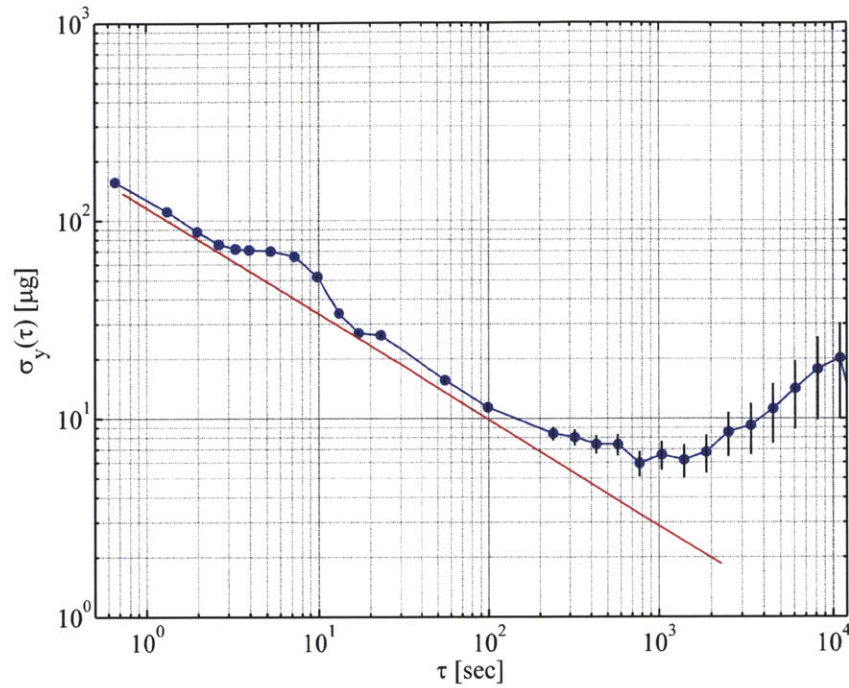


Figure 4-6: Allan deviation of gravity data acquired over 11 hours at a repetition rate of 1.7 Hz. The red line represents a $\tau^{-1/2}$ trend. The minimum value of $6 \mu g$ occurs at $\tau \approx 750$ seconds. The feature at $\tau \approx 5$ seconds is likely the result of rocking motion of the optical table.

frequency band), the vibrations are not sufficiently coherent from shot to shot to average down effectively as τ^{-1} . In effect, the interferometer samples a random phase, producing an apparent velocity random walk process with averaging statistics scaling as $\tau^{-1/2}$. The instability observed at $\tau \approx 5$ seconds is due to rocking motion of the optical table at the ≈ 10 mrad level, since the optical table is floated but not actively stabilized.

The apparatus is unfortunately located in a laboratory environment that is quite adverse to making precise gravity measurements—several stories above ground, with large environmental control systems in close proximity. Nevertheless, the value of gravity obtained, $9.80381 \pm 0.00006 \text{ m/s}^2$, agrees with the value predicted by a gravity survey, $9.80382 \pm 0.00002 \text{ m/s}^2$, accounting for elevation and table tilt³. At shot noise-limited performance (assuming $N \sim 10^6$ and $T = 3.5 \text{ ms}$), the interferometer would achieve a sensitivity of $\approx 0.56 \mu g/\sqrt{\text{Hz}}$. The following section discusses sources of systematic error.

³National Geodetic Survey, Lat. = $N42^\circ 21' 54''$, Long. = $W71^\circ 5' 26''$.

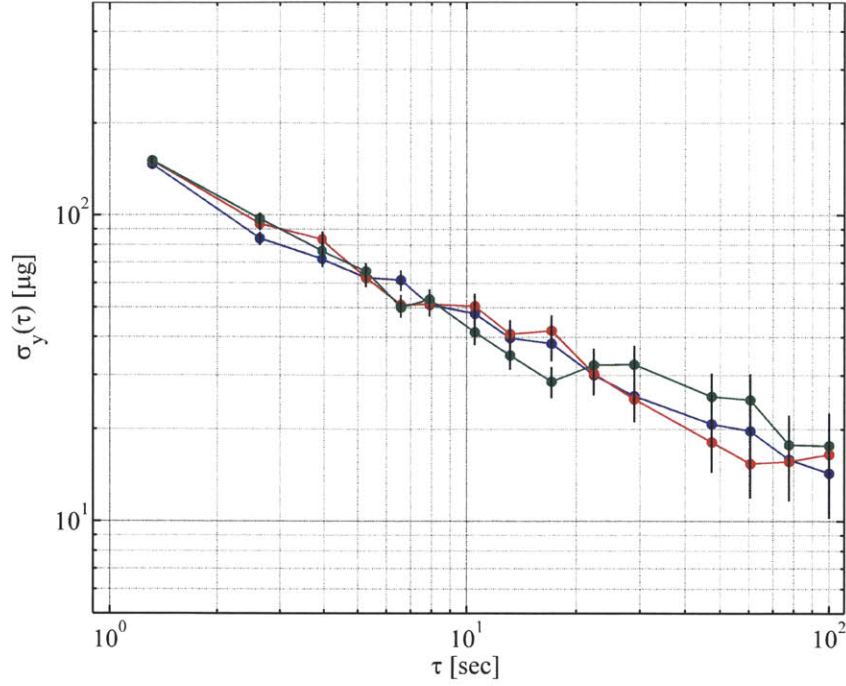


Figure 4-7: Allan deviation of gravity data acquired at different interrogation times. Blue: $T = 3.25$ ms, Red: $T = 3.1$ ms, Green: $T = 3$ ms. Despite the variation in scale factor, the noise statistics are very similar. This indicates that high frequency vibrations are the dominant noise source.

4.4.1 Systematics

The accuracy of the measurement is limited by several systematic error sources. First, misalignment of the Raman beams from local vertical by angle θ leads to an error $g_{meas}/g = \cos(\theta)$, where g_{meas} is the acceleration measured by the interferometer. The tilt of the Raman beams was measured with an uncertainty $\Delta\theta \approx 0.3^\circ$, corresponding to an uncertainty in g of $\approx 4 \mu g$. This is the largest source of systematic error ⁴. Uncertainty in \mathbf{k}_{eff} also results from the resolution of the laser wavelength. By locking the laser to an optical transition in cesium, the laser frequency is known to 1 MHz (≈ 1 ppb), so it is not a significant error source. Noise in the microwave frequency electronics used to generate the Raman frequency difference also leads to fluctuations in the interferometer phase. With a method similar to that applied in analyzing the contribution of vibrations to interferometer phase noise, a transfer function for Raman phase noise in the three-pulse interferometer can be derived [78] (Fig. 4-8 shows

⁴A more precise measurement could be done, in principle, but table motion quickly becomes the dominant source of pointing uncertainty.

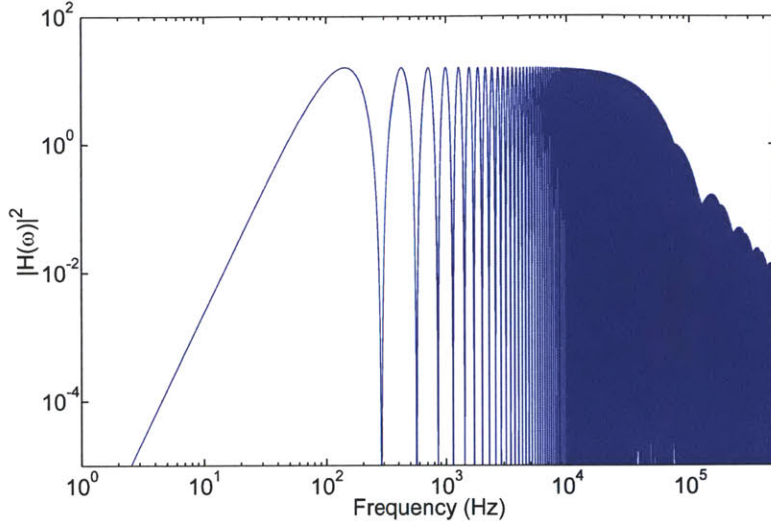


Figure 4-8: Frequency response of the $\pi/2 - \pi - \pi/2$ interferometer to laser phase noise ($T = 3.5$ ms, $\tau = 10$ μ s). The pulse duration effectively high pass filters laser phase noise, since these fluctuations average within one pulse. At frequencies $< 1/2T$, the contribution of fluctuations is small over the duration of the interferometer. The interferometer is insensitive to Fourier components with frequencies at multiples of $\sim 1/(T + 2\tau)$, where τ is the π pulse duration.

this function, $|H(\omega)|$, for $T = 3.5$ ms and a π pulse duration of 10 μ s).

$$\sigma_{\Delta\phi}^2 = \int_0^{\infty} |H(\omega)|^2 S_{\phi}(\omega) d\omega \quad (4.6)$$

where $S_{\phi}(\omega)$ is the Raman phase power spectral density. From the measured power spectral density of the Raman EOM drive signal, which defines the Raman phase excluding mirror vibrations, $\sigma_{\Delta\phi}$ is estimated to be ≈ 3 mrad ($\Delta g/g \approx 2 \times 10^{-6}$). This is not currently a dominant noise source, and could be further reduced in the future by generating the 9.2 GHz signal from a cleaner oscillator.

Fluctuations in the Raman intensity lead to noise in the relative populations. Intensity fluctuations σ_I lead to proportional changes in the effective Rabi frequency, $\sigma_I/I = \sigma_{\Omega_{\text{eff}}}/\Omega_{\text{eff}}$. The resulting noise in the relative populations σ_P after the three-pulse sequence is approximately

$$\sigma_P = \frac{\sqrt{3}\pi}{2} \frac{\sigma_I}{I}, \quad (4.7)$$

assuming uncorrelated noise in each pulse [3]. For shot-to-shot fluctuations at the level of $\approx 0.3\%$, $\sigma_P < 0.01$ and therefore $\Delta g/g \approx 10^{-6}$ per shot. While this is not the current

sensitivity limitation, the Raman laser power is not actively stabilized and drifts at the $\sim 1\%$ level occur over hour-time scales, which could produce long term drifts.

Another light-based error source results from AC Stark shifts. As described earlier in this chapter, the differential AC Stark shift between the two interferometer states is canceled by tuning the intensity ratio of the Raman beam frequency components. The three-pulse interferometer is intrinsically insensitive to AC Stark shifts, as long as the shift is the same in all three pulses. The phase shift due to a differential AC Stark shift $\delta_{AC,j}$ during pulse j is

$$\Delta\phi_{AC} = \frac{\delta_{AC,3}}{\Omega_{\text{eff}}} - \frac{\delta_{AC,1}}{\Omega_{\text{eff}}} \quad (4.8)$$

When canceled, fluctuations in the Raman beam power do not lead to a variation in the differential AC Stark shift. Long term cancellation relies on the stability of the phase modulation signal and optical properties of the electro-optic modulator, which can vary due to environmental factors such as temperature drift. For a non-zero differential AC Stark shift, however, the expansion of the cloud over the non-uniform beam can introduce significant shifts. This effect is commonly a long term stability limitation for Raman pulse atom interferometers, and are more problematic for sensors operating at shorter interrogation times (the phase shifts introduced by AC Stark shifts do not significantly change with interrogation time, so it is a fractionally larger effect). The amplitude of the 9.2 GHz signal driving the EOM is stable to ~ 0.1 dB over several hours. Over multiple hour durations, AC Stark shifts were measured to produce systematic phase shifts of on the order of ~ 0.01 rad for $\delta_{AC} \sim 0.1\Omega_{\text{eff}}$, which is the dominant limitation to the long term stability of the measurement. In principle, these long term drifts could be suppressed by comparing measurements with opposite Raman beam propagation direction (e.g., see [34]). While the phase shift due to gravitational acceleration will change sign, systematic shifts from AC Stark shifts and Raman beam power drift do not.

Higher-order Inertial Effects

Time-varying and higher-order inertial effects also affect the accuracy of a gravity measurement. First, daily tidal variations occur at the $\sim 10^{-7} g$ level, and are therefore not a significant source of error in these measurements. Secondly, gravity gradients introduce a

higher-order phase shift, as described in Section 2.2.3:

$$\Delta\phi_{\text{grav.grad.}} = k_{\text{eff}}\gamma T^2 \left(\frac{7}{12}gT^2 - \dot{z}(0)T - z(0) \right) \quad (4.9)$$

where $\dot{z}(0) = \dot{z}(0) + \frac{1}{2}v_r$ is the mean velocity of the two wavepackets after the beam splitter pulse. For an interferometer with $T = 3.5$ ms and a drop time of 13 ms, the offset in the measured gravity value is ~ 0.1 ng, which is also well below the resolution of the interferometer.

Finally, imperfect alignment of the Raman beam with \mathbf{g} leads to a horizontal velocity component in the trajectory of the atom during the interferometer, which means that spatial area is enclosed and a Sagnac phase shift is introduced. In this case, the rotation rate of the Earth induces a phase shift:

$$\Delta\phi_{\text{rot}} = 2\mathbf{\Omega} \cdot (\mathbf{v}_0 \times \mathbf{k}_{\text{eff}})T^2 \quad (4.10)$$

where $\mathbf{\Omega}$ is the Earth rotation rate ($\approx 7.29 \times 10^{-5}$ rad/s), \mathbf{v}_0 is the initial velocity of the atom, and m is the atomic mass. Therefore, the error in gravity is:

$$\Delta g = \frac{\Delta\phi_{\text{rot}}}{k_{\text{eff}}T^2} = 2\mathbf{\Omega} \cdot (\mathbf{v}_0 \times \hat{\mathbf{k}}_{\text{eff}}) \quad (4.11)$$

Given the Raman beam pointing uncertainty and the drop time of the atoms, the offset is only $\Delta g/g \approx 10^{-8}$, which again is below the current resolution.

4.5 Raman Pulse Dephasing

An important factor which limits contrast for short interrogation time interferometry is the transfer efficiency of the Raman pulses. The atom temperature does not increase significantly during the interrogation, so high Rabi frequencies allow transform-limited Raman pulses. As Chapter 5 discusses, Raman pulse transfer efficiency is also the primary limitation to realizing larger area interferometers and higher sensitivity.

The dominant limitation to transfer efficiency in this apparatus is due to the non-uniformity of the intensity profile of the Raman beams. An ideally uniform Raman beam profile would produce a constant Rabi frequency across the ensemble. The Gaussian envelope

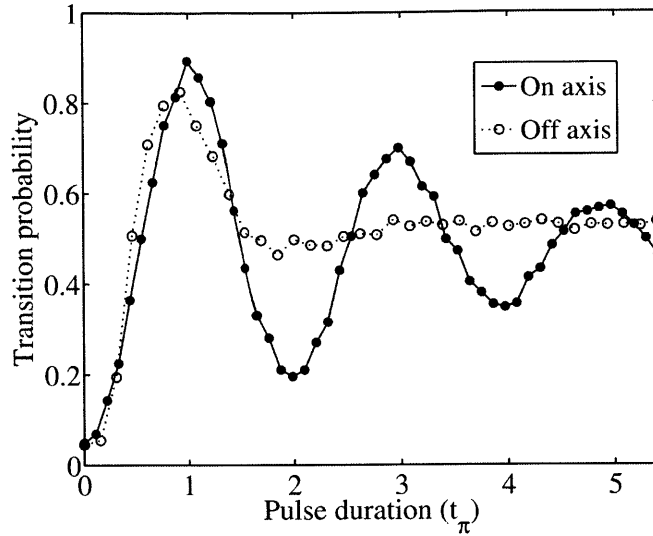


Figure 4-9: Doppler insensitive Raman pulse population transfer versus pulse duration. The solid curve was acquired with the cloud centered in the Raman beam, and the dotted curve was acquired with the cloud displaced radially by 3 mm from the center of a 5 mm beam. More rapid dephasing is evident in the off-axis case.

of the Raman beam and imperfections in the optics, however, create a spatial distribution of Rabi frequencies. Figure 4-9 shows population transfer as a function of Raman pulse duration. By displacing the atoms radially in the Raman beam, Rabi oscillations appear to decay more rapidly as a result of the broader distribution of intensity. However, this effect is not the result of an irreversible decoherence— coherence is preserved in each atom, and in principle, the dephasing is reversible at some level.

A diagnostic was developed to isolate the effects of Raman beam non-uniformity on population transfer, using an $n\pi - n\pi$ pulse sequence, with even n . The basic idea of the diagnostic is to apply two Doppler insensitive Raman pulses of variable duration in rapid succession. The pulses have identical durations but a relative phase of 0 or π . The effect of the second pulse in the latter case is, at least in part, to undo the dispersion in transfer induced by the first Raman pulse. A similar regimen is used to test the fidelity of quantum information systems manipulated by microwave pulses, drawing on spin echo techniques developed for NMR spectroscopy [79–82].

In the pseudospin representation, depicted in Fig. 4-10, an inhomogeneous Rabi frequency causes the pure initial spin state to spread angularly in the plane of rotation. The dephasing becomes more pronounced with increasing pulse duration, ultimately dispersing

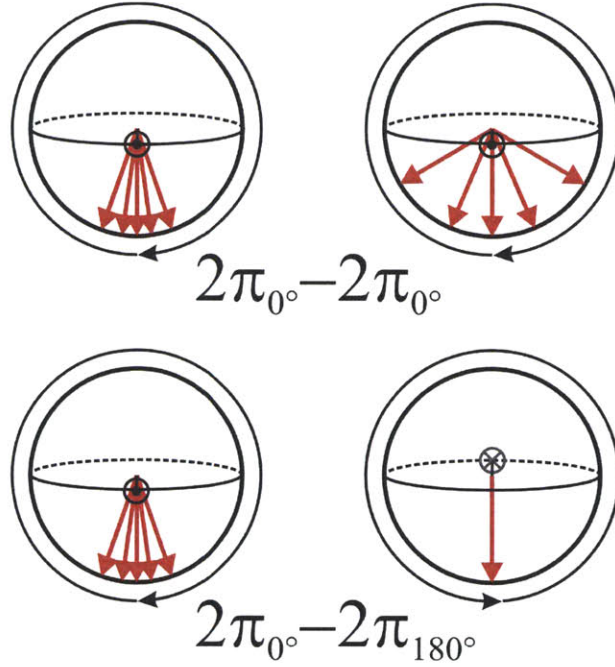


Figure 4-10: Bloch sphere representation of the Raman pulse dephasing diagnostic discussed in Section 4.5. The initial state is spin down, and the spheres represent the state after each pulse. A $2\pi_{0^\circ} - 2\pi_{0^\circ}$ sequence dephases the ensemble in both pulses. The second pulse of the $2\pi_{0^\circ} - 2\pi_{180^\circ}$ sequence, however, reverses the dephasing.

the ensemble with longer pulses. Figure 4-11 shows the measured final relative populations after several $n\pi - n\pi$ sequences, with a common dwell time of $16 \mu\text{s}$. In the $n\pi_{0^\circ} - n\pi_{0^\circ}$ sequence, where the subscript refers to the relative phases of the pulses, both pulses lead to dephasing. Conversely, the second pulse in the $n\pi_{0^\circ} - n\pi_{180^\circ}$ sequence effectively counter-rotates the pseudospin and reverses the dispersion produced by the first pulse, assuming the atoms are motionless and the Raman beam intensity is constant. Both sequences should, in a uniform Raman beam, return the pseudospin to the initial state. However, as the data in Fig. 4-11 show, the final state of the ensemble after the $n\pi_{0^\circ} - n\pi_{180^\circ}$ sequence is weighted more toward the initial $F = 3$ state, even beyond an accumulation of 20π in pulse area. At longer pulse durations, rephasing is degraded by spontaneous emission and dephasing due to imperfect AC Stark shift cancellation.

The same experiment was run with the atoms radially displaced by 3 mm from the center of the Raman beam. As the other curves in Fig. 4-11 show, it is clear that dispersion is even more dramatic in the $n\pi_{0^\circ} - n\pi_{0^\circ}$ sequence. The $n\pi_{0^\circ} - n\pi_{180^\circ}$ sequence, however, still achieves significant rephasing in the presence of a far broader intensity distribution.

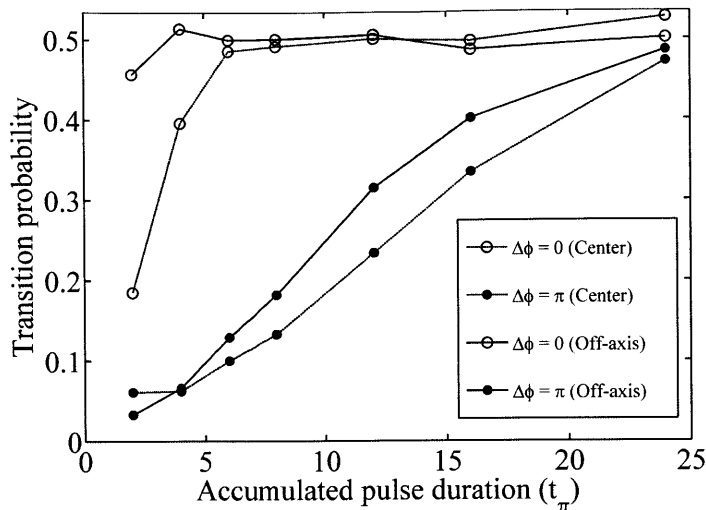


Figure 4-11: Raman pulse dephasing measured by two pulse ($n\pi_{0^\circ} - n\pi_{0^\circ/180^\circ}$) interferometers. Open (solid) points correspond to zero (π) phase shift in the second pulse. These profiles are shown for a cloud centered in the Raman beam, and then radially displaced by 3 mm.

This result motivates composite pulse sequences, which accomplish the same net transfer as a π pulse but use multiple rotations at different laser phases to reduce these dispersive effects. Chapter 5 discusses particular pulse sequences that improve transfer efficiency and enable large area atom interferometers with Raman pulses. Contrast loss as a function of the transverse position of the cloud also has important implications for the design of a sensor operating in a dynamic environment, where the transverse motion of the atom could be significant. The design of the sensor must trade Raman beam size with the dynamic range, maximum input, and bandwidth requirements of the sensor. A wider Raman beam can accommodate larger transverse input, but the required laser power quickly increases.

4.6 Summary

In this chapter, a gravity measurement using short interrogation time atom interferometry was described. The primary limitation to the sensitivity of the current apparatus is high frequency vibrations in the laboratory environment. Longer term stability was affected mostly by slowly-varying phase shifts introduced by AC Stark shifts. Significant improvements in sensitivity could be made by better vibration isolation (e.g., mounting the Raman retro-reflector on a passive isolation stage), though much of the vibration resulted from acoustic

noise that may require other measures to effectively isolate the mirror. Alternatively, the position of the mirror could be continuously monitored by a Michelson interferometer using the Raman beam path as one arm, and used in analysis to compensate for the motion. In the future, improvements to the readout SNR, Raman beam intensity and phase stability, and repetition rate, could yield a sensitivity of $<1 \mu g/\sqrt{\text{Hz}}$. Finally, sources of Raman pulse dephasing were diagnosed and implications for interferometer performance in a dynamic environment were discussed.

Chapter 5

Composite Raman Pulses and Large Area Atom Interferometry

This chapter presents a demonstration of large area atom interferometry with Raman transitions, and proposes it as a method for increasing the sensitivity of a high bandwidth atom interferometric inertial sensor. Large area atom interferometry is realized with large momentum transfer (LMT) atom optics, which linearly improve the precision of an atom interferometer with the relative momentum splitting of the atomic wavepackets. As discussed in Chapter 1, existing light pulse atom interferometers achieve state of the art performance in measurements of gravity, rotation, and gravity gradients in laboratory conditions [4,6,25]. Atom interferometers operating in a dynamic environment, however, are constrained to potentially much shorter interrogation times, trading away much sensitivity for sensor compactness, dynamic range and bandwidth. In this regard, LMT atom optics could improve interferometer precision without a requisite reduction in sensor bandwidth, thereby regaining some of the sensitivity lost at shorter interrogation times.

In this work, large momentum transfer is achieved with extended Raman pulse sequences, based on the Mach-Zehnder $\pi/2 - \pi - \pi/2$ interferometer. The maximum achievable momentum transfer is limited by the transfer efficiency of the Raman pulses, since this factor ultimately constrains the interferometer contrast and phase SNR. In this chapter, it is shown that by using more efficient composite Raman pulses, the momentum splitting can be increased to $9\hbar k_{\text{eff}} \approx 18\hbar k$ (compared to the standard $2\hbar k$ Raman beam splitter), thus

increasing the inertial phase shift by a factor of nine. Composite pulses techniques were initially developed for high-resolution NMR spectroscopy, and are implemented here for the first time in a light pulse atom interferometer. The main advantages of this approach are that the increase in precision can be obtained without using significantly colder atoms, making drastic increases in laser power or reductions in repetition rate. In addition, composite Raman pulses are shown to improve the robustness of the interferometer to several effects that limit Raman pulse transfer efficiency and are of particular concern to operation in a dynamic environment.

5.1 Large Momentum Transfer with Raman Pulses

The most widely-demonstrated light pulse atom optics are stimulated Raman transitions, which impart momentum splittings of $2\hbar k$. While other light pulse atom optics, such as multi-photon Bragg pulses [46, 47, 83] and Bloch oscillations [46, 84], have achieved larger momentum splittings and offer higher precision, Raman pulse beam splitters place less stringent demands on atom temperature. Multi-photon Bragg transitions have demonstrated $24\hbar k$ single-pulse beam splitters [46] and up to $102\hbar k$ with sequential-pulse beam splitters [47]. Efficient transfer with Bragg pulses, however, requires sub-recoil temperatures, achieved either by narrow velocity selection, which limits sensitivity due to atom number counting statistics, or by using ultracold samples that are produced at low repetition rates (e.g., 0.3 Hz in [54]). As a result, Raman pulse atom optics appear technologically favorable for high bandwidth sensors.

As first demonstrated by McGuirk *et al.* [45], extended Raman pulse sequences with alternating wavevectors, $\pm\mathbf{k}_{\text{eff}}$, increase the momentum splitting between atomic wavepackets by a factor of $2N + 1$, where N is the number of pulses inserted after the initial $\pi/2$ beam splitter pulse. Fig. 5-1 depicts a sequence of N π pulses, called augmentation pulses here, after the initial $\pi/2$ pulse that imparts $(4N + 2)\hbar k$ of relative momentum. A large area Mach-Zehnder interferometer, shown in Fig. 5-2, is then composed of a symmetric sequence of $4N + 3$ pulses that splits, reflects, and recombines wavepackets, and results in an inertial phase shift larger by a factor of $2N + 1$ over the conventional $\pi/2 - \pi - \pi/2$ interferometer.

In the first demonstration of large area Raman pulse interferometry, a momentum split-

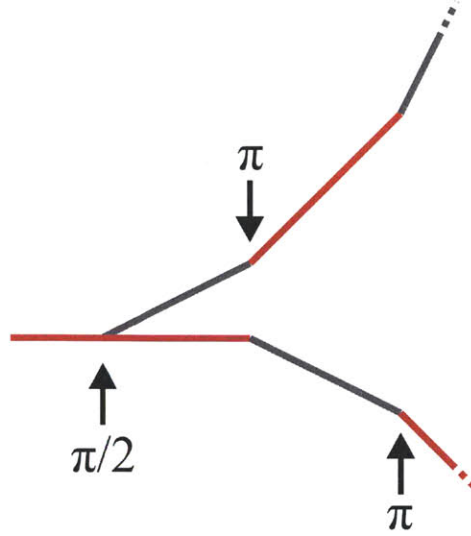


Figure 5-1: Diagram of Raman pulse sequence that increases the relative momentum of atomic wavepackets to $(4N + 2)\hbar k$, where N is the number of augmentation pulses of alternating propagation direction after the $\pi/2$ pulse. The arrows indicate the Raman beam propagation direction, \mathbf{k}_{eff} , and the line colors denote the internal states of the wavepackets (e.g., Red= $|g\rangle$ and Grey= $|e\rangle$).

ting of $6\hbar k$ ($N = 1$) was reported [45]. The major limitations to increasing the number of augmentation pulses were cited as Rabi frequency inhomogeneities arising from the Gaussian-shaped Raman beam, the frequency selectivity of a square pulse, and decoherence due to spontaneous emission. All of these factors reduce population transfer efficiency, interferometer contrast, and phase SNR, which ultimately obviates the use of larger momentum interferometers despite the larger signals available. McGuirk *et al.* [29] suggested the substitution of composite Raman pulses for the conventional π augmentation pulses as a means of increasing the efficiency of the augmentation pulses, thereby enabling larger momentum splittings without significant degradation of interferometer contrast.

5.1.1 Composite Pulse Techniques

A composite pulse is composed of a sequence of contiguous or nearly contiguous pulses (subpulses) at constant amplitude but different relative phase [85]¹. It is illustrative to describe the action of a composite pulse on the atomic state as consecutive rotations of the atomic pseudospin on a Bloch sphere, recalling the discussion in Section 2.1.1. This

¹More complex composite pulses with frequency or amplitude shaping have been used in NMR experiments, but are beyond the current scope.

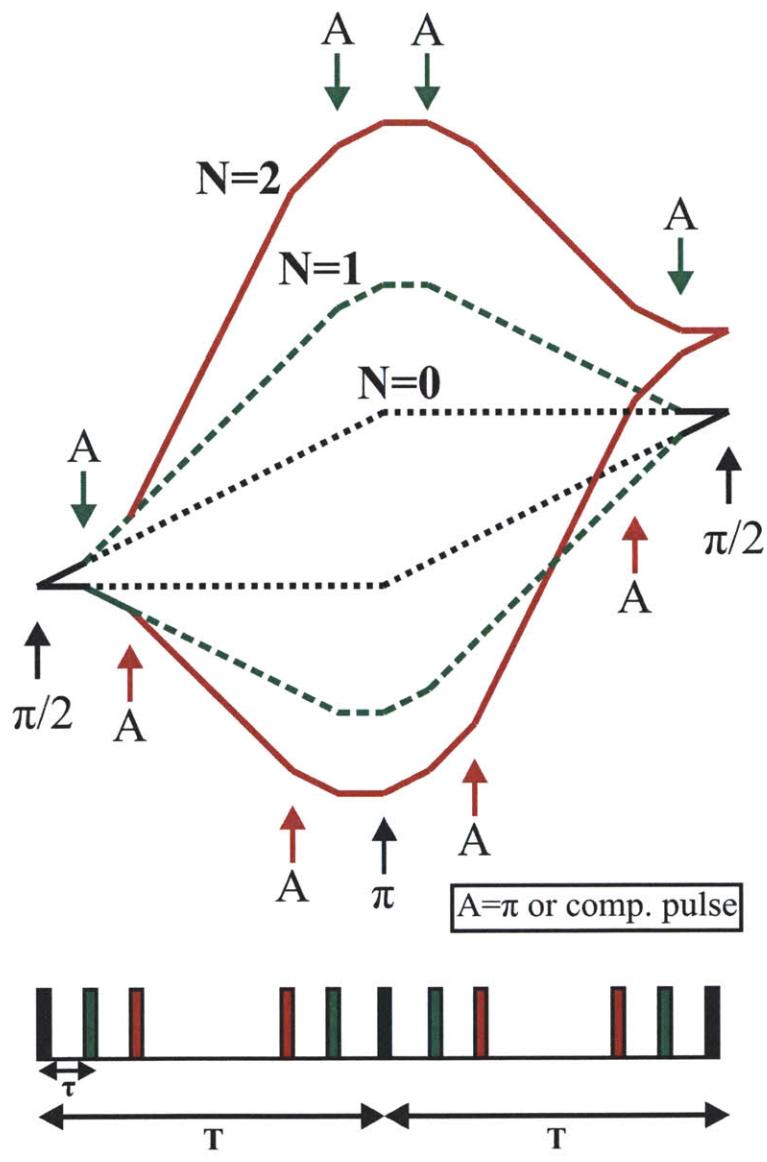


Figure 5-2: Diagram of two large area atom interferometers ($N = 1, 2$) compared to a $\pi/2 - \pi - \pi/2$ ($N = 0$) interferometer. The augmentation pulses are denoted A .

framework elegantly links Raman pulse population transfer to NMR techniques, from which composite pulses were initially developed.

Fig. 5-3 depicts the evolution of the atomic state for a simple composite pulse used for population inversion, $\pi/2_{0^\circ} - \pi_{90^\circ} - \pi/2_{0^\circ}$, where the subscripts indicate the relative phase of the effective drive field between subpulses (for now, consider coherent transfer between two hyperfine ground states driven by microwave pulses). As the figure shows, this sequence of subpulse rotations accomplishes the same net rotation as a single π pulse, inverting population from one state to the other. The composite pulse, however, achieves near perfect inversion for a larger range of Rabi frequency errors. For this reason, the composite pulse yields higher average transfer efficiency with an ensemble sampling a spatially-varying drive field intensity, as encountered in interrogations of cold atom samples with laser and microwave fields [86]. Composite pulses can also achieve efficient population inversion over a larger bandwidth [87], as shown in Fig. 5-4. For example, the bandwidth of a π pulse is limited to a full-width-half-maximum (FWHM) of $2\Omega_0$, where Ω_0 is the Rabi frequency, while the bandwidth of the $\pi/2_{0^\circ} - \pi_{90^\circ} - \pi/2_{0^\circ}$ sequence approaches $4\Omega_0$. Thus, composite pulses can also be more robust to inhomogeneous broadening effects (e.g., atom temperature).

The primary advantage of composite pulse techniques is that robustness is obtained without significant additional technical complexity beyond that which is required to implement square pulses. More advanced composite pulse techniques involving shaped pulses have also been proposed for higher efficiency and robustness (e.g., [88]), but come at the cost of more complex implementation. In NMR spectroscopy, a staggering variety of composite pulses have been developed with varying degrees of insensitivity to Rabi frequency error, detuning, and phase error (i.e., for imperfectly applied phase shifts between subpulses) [89–92]. Composite pulses have served more recently as diagnostic tools for analyzing the fidelity of microwave manipulations in quantum information systems. Fidelity determines the number of possible manipulations before the ensemble is dephased, and its coherent evolution is no longer detectable [80,81].

Section 5.2 describes the experimental characterization of two composite Raman pulses, $\pi/2_{0^\circ} - \pi_{90^\circ} - \pi/2_{0^\circ}$ and $\pi/2_{0^\circ} - \pi_{180^\circ} - 3\pi/2_{0^\circ}$, where in the context of Raman pulses, the subscripts refer to the relative effective laser phase ϕ_{eff} of each subpulse. Both of these sequences are designed for high efficiency, broadband population inversion. Finally, Section

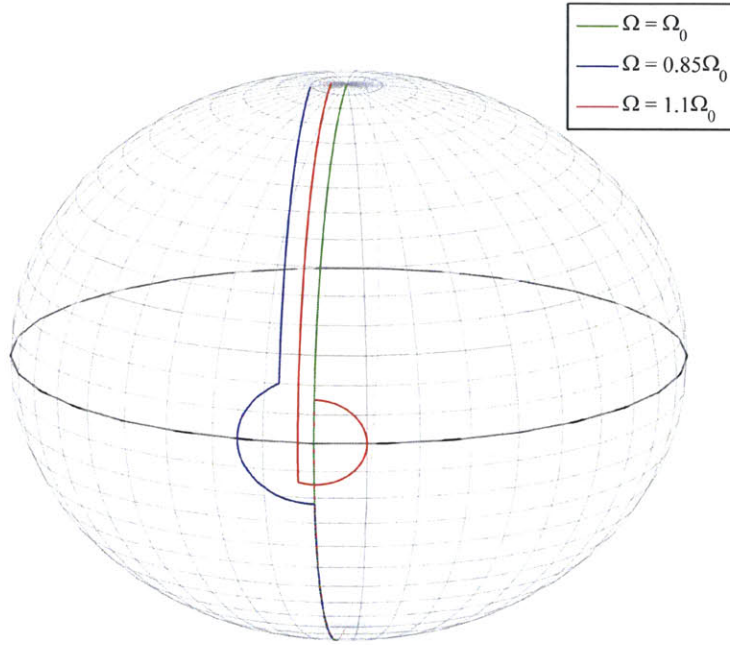


Figure 5-3: Atomic pseudospin evolution for a population-inverting composite pulse ($\pi/2_{0^\circ} - \pi_{90^\circ} - \pi/2_{0^\circ}$), in the presence of pulse length errors resulting from drive field inhomogeneities. Even for a $\approx 10\%$ error in pulse length, the composite pulse transfers over 98% of the population.

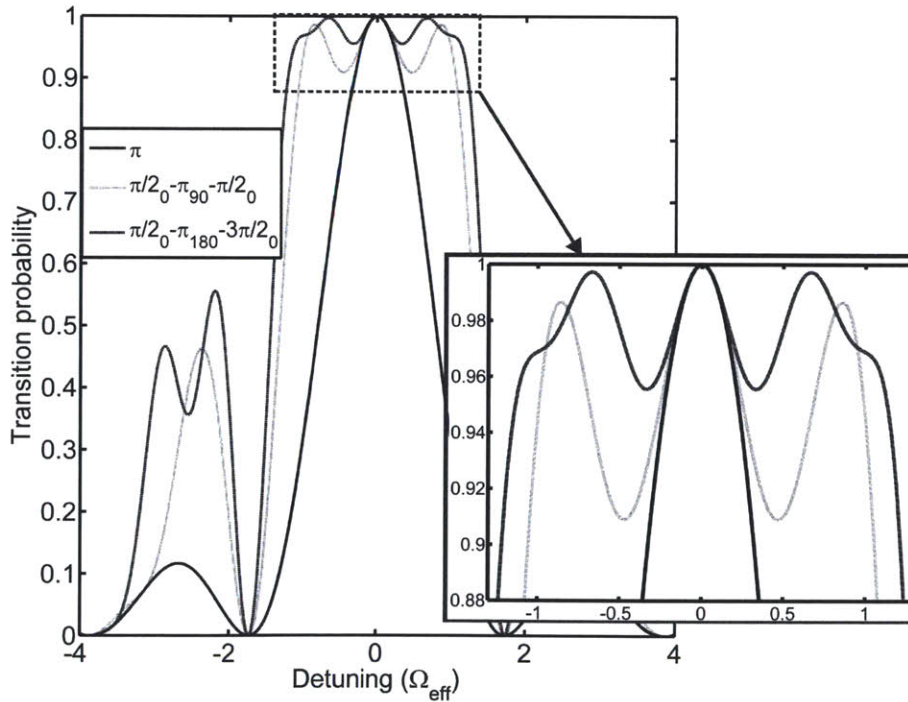


Figure 5-4: Comparison of theoretical detuning profiles of a π pulse and the $\pi/2_{0^\circ} - \pi_{90^\circ} - \pi/2_{0^\circ}$ and $\pi/2_{0^\circ} - \pi_{180^\circ} - 3\pi/2_{0^\circ}$ composite pulses. The larger bandwidth of the composite pulses is evident (these profiles assume the same Rabi frequency)).

5.3 discusses the application of composite Raman pulses as augmentation pulses for increasing the momentum splitting of Raman pulse interferometers up to $18\hbar k$ (corresponding to a factor of $\approx 9\times$ increase in the inertial phase shift).

5.2 Composite Raman Pulses

As mentioned above, composite pulses improve transfer efficiency by compensating for pulse length and detuning errors, and are relatively simple to implement. Since these practical limitations are closely analogous to the effects that composite pulses were designed to suppress in NMR experiments, composite Raman pulses can be expected to improve the contrast, and thus the phase SNR of large area atom interferometers. Achieving high efficiency with composite Raman pulses, in contrast to NMR experiments, is ultimately constrained in total pulse duration by decoherence from spontaneous emission. This precludes the use of almost arbitrarily-efficient ‘super-cycle’ composite pulses, which can involve pulse areas exceeding 45π [90, 91]. Therefore, shorter composite pulses like the $\pi/2_{0^\circ} - \pi_{90^\circ} - \pi/2_{0^\circ}$ sequence described above are more suitable in interferometry.

As previously discussed, Fig. 5-4 shows the population transfer of the $\pi/2_{0^\circ} - \pi_{90^\circ} - \pi/2_{0^\circ}$ composite pulse as a function of detuning. Neglecting spontaneous emission, this profile is identical to the one produced with the Raman pulse theory described in Chapter 2, highlighting the power of the isomorphic relation of Raman pulse and NMR physics. Here, the three subpulses are assumed to be contiguous (i.e., zero dwell times), since this maximizes the bandwidth of population inversion and reduces sensitivity to atom temperature. Moreover, in the context of large area atom interferometry with Raman pulses, broadband population inversion is essential because of the differential Doppler shifts that occur between wavepackets during augmentation pulses in the interferometer (this issue is discussed in more detail in Section 5.3). Fig. 5-4 also shows the detuning profile of a slightly longer composite pulse sequence, $\pi/2_{0^\circ} - \pi_{180^\circ} - 3\pi/2_{0^\circ}$, which was first proposed and demonstrated in NMR by Shaka *et al.* [90, 93]. This composite pulse achieves efficient population inversion over an even larger bandwidth. The reason for the large bandwidth of this composite pulse is not as intuitive as the other (incidentally, this composite pulse was invented by numerical optimization [90]). Fig. 5-5 illustrates a particular example in which, despite a large detuning

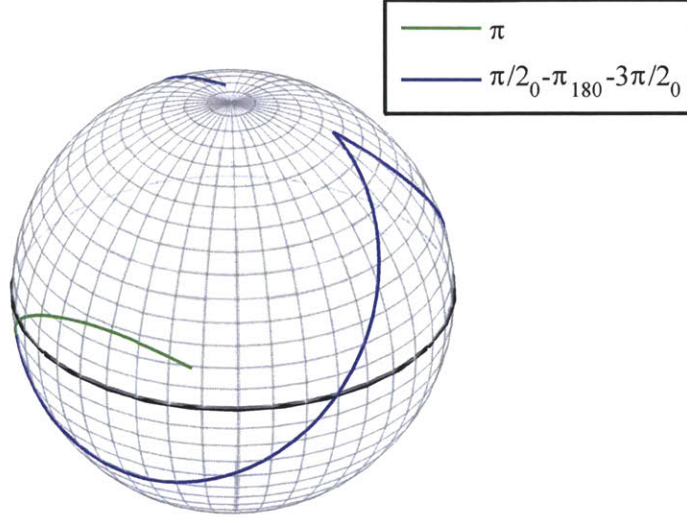


Figure 5-5: Bloch sphere representation of population inversion by a $\pi/2_0^\circ - \pi_{180^\circ} - 3\pi/2_0^\circ$ composite pulse and a π pulse for a drive field detuned by $\delta = 0.6\Omega_0$. While the π pulse achieves $\approx 60\%$ transfer, the non-trivial evolution of the composite pulse transfers 99% of the population.

($0.6\Omega_0$), the non-trivial subpulse rotations manage to achieve near-perfect population inversion, dramatically improving upon a π pulse. The next section describes the implementation of these composite pulses, where it is seen that the $\pi/2_0^\circ - \pi_{180^\circ} - 3\pi/2_0^\circ$ provides superior robustness.

5.2.1 Experiment

Composite Raman pulses were implemented with the same apparatus described in Chapter 3. Fig. 5-6 compares the observed transfer efficiency of both Doppler sensitive composite Raman pulses as a function of Raman detuning, as well as the profile for a π pulse. These data were acquired with $\approx 0.5 \mu\text{K}$ samples ($\Delta p \approx 1.5\hbar k$, achieved by velocity selection). The atom cloud was approximately 1 mm across. Both composite pulses achieved broadband inversion, but the $\pi/2_0^\circ - \pi_{90^\circ} - \pi/2_0^\circ$ sequence (lower plot) exhibited a spurious asymmetric feature near resonance. This resulted from transient phase and amplitude errors in the Raman EOM drive signal, due to bandwidth limitations in the RF frequency mixer (see Section 3.5.1). These errors occurred between subpulses, when phase shifts were applied. While

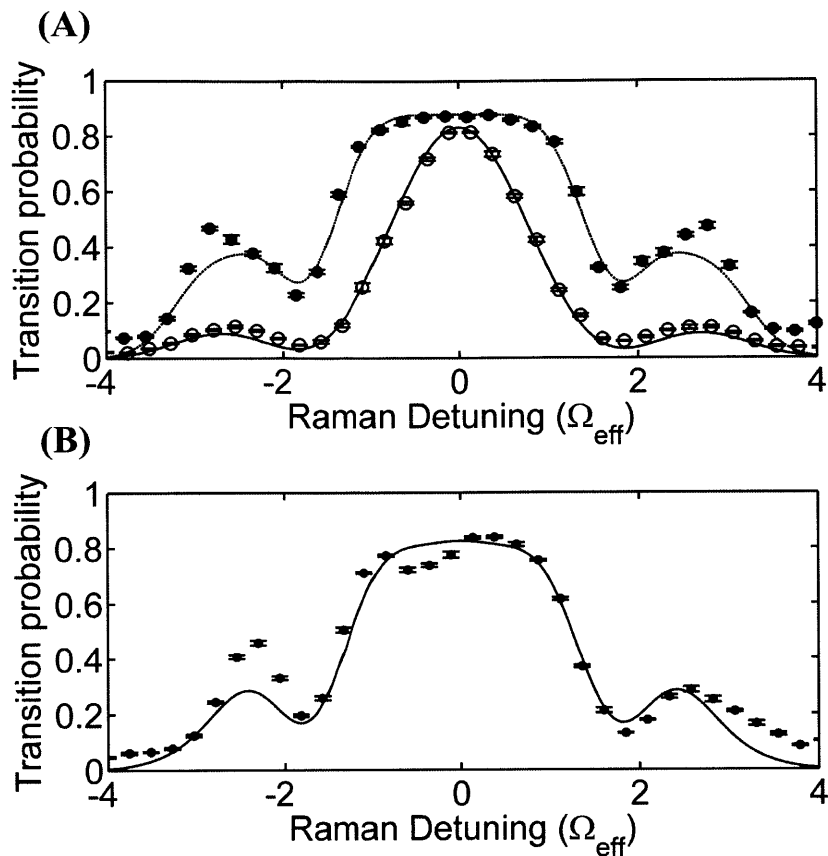


Figure 5-6: Detuning profiles of Doppler sensitive composite Raman pulses. A) Comparison of a π pulse with a $\pi/2_{0^\circ} - \pi_{180^\circ} - 3\pi/2_{0^\circ}$ composite pulse. B) Profile of the $\pi/2_{0^\circ} - \pi_{90^\circ} - \pi/2_{0^\circ}$ composite pulse. The profile exhibits lower transfer near resonance, due to amplitude and phase shift errors occurring between subpulses. Each point represents an average of four shots. Theoretical curves include thermal averaging and use frequency offset and overall amplitude as free parameters.

the detuning profile of the $\pi/2_{0^\circ} - \pi_{180^\circ} - 3\pi/2_{0^\circ}$ composite pulse also exhibits a slight asymmetry, it is largely unaffected by these experimental defects. Interestingly, previous NMR studies recognized insensitivity to phase shift errors in composite pulses using strictly 180° phase shifts ('phase-alternating') [93,94].

A model was developed for calculating composite Raman pulse detuning profiles, including the velocity distribution of the ensemble (a Maxwell-Boltzmann velocity distribution was assumed). Wavepacket amplitudes were calculated according to the diagrammatic method described in Stoner *et al.* [60], which derives a Raman pulse operator for time-varying detunings. For reference, a summary of the model is provided in Appendix B. In the case of the $\pi/2_{0^\circ} - \pi_{180^\circ} - 3\pi/2_{0^\circ}$ composite pulse, the observed peak transfer is 89%, an increase of

9% over that of a π pulse. For a Rabi frequency of $\Omega_{\text{eff}}/2\pi = 50$ kHz, this sequence achieved $>80\%$ transfer over a range of $\pm\Omega_{\text{eff}}$ (approximately the FWHM of the π pulse detuning profile). This composite pulse also exceeded the transfer efficiency of the $\pi/2_{0^\circ} - \pi_{90^\circ} - \pi/2_{0^\circ}$ sequence over a broad range of atom temperatures, especially for hotter atoms. With an ≈ 8 μK sample, the $\pi/2_{0^\circ} - \pi_{180^\circ} - 3\pi/2_{0^\circ}$ composite pulse achieved 84% transfer, while the $\pi/2_{0^\circ} - \pi_{90^\circ} - \pi/2_{0^\circ}$ composite pulse and π pulse achieved 76% and 63%, respectively.

Both composite pulses demonstrated relative insensitivity to Rabi frequency inhomogeneities as well. This factor was measured by comparing the transfer efficiency of composite pulses with that of a π pulse, using Doppler insensitive Raman transitions to eliminate sensitivity to atom temperature. As Fig. 5-7 shows, both composite pulses achieved a maximum transfer of 97% with a cloud of ≈ 1 mm in diameter and a Raman beam diameter of 5 mm ($1/e^2$). The maximum π pulse transfer was 91%. It is interesting to note that the $\pi/2_{0^\circ} - \pi_{180^\circ} - 3\pi/2_{0^\circ}$ composite pulse achieved a transfer efficiency similar to the π pulse near resonance, but yielded higher transfer at large detuning ($\sim \pm 0.5\Omega_{\text{eff}}$). This result indicates that the composite pulse is less sensitive to the Raman beam intensity distribution when off resonance, and equally as sensitive as the π pulse on resonance. The latter fact is expected. Due to the symmetry of the subpulse rotations, this composite pulse produces the same transfer as a π pulse exactly on resonance for any drive field intensity. As mentioned above, the large asymmetric feature in the profile of the $\pi/2_{0^\circ} - \pi_{90^\circ} - \pi/2_{0^\circ}$ composite pulse is the result of the transient amplitude and phase errors between subpulses (without thermal averaging, the effect appears more dramatic here than in the Doppler sensitive case shown in Fig. 5-6).

Robustness to intensity gradients over the atom cloud may also prove useful for atom interferometers operating in a dynamic environment. If a sensor accelerates transversely to the Raman beam axis, the cloud could be interrogated in regions of the beam with higher intensity gradients (e.g., in a Gaussian beam profile), leading to pulse length errors and, consequently, reduced contrast. In principle, composite Raman pulses would mitigate the impact of these effects on sensor performance.

In summary, the $\pi/2_{0^\circ} - \pi_{180^\circ} - 3\pi/2_{0^\circ}$ composite pulse demonstrated superior transfer efficiency and robustness to atom temperature and a non-uniform Raman beam. It is possible that in other implementations the $\pi/2_{0^\circ} - \pi_{90^\circ} - \pi/2_{0^\circ}$ composite pulse may per-

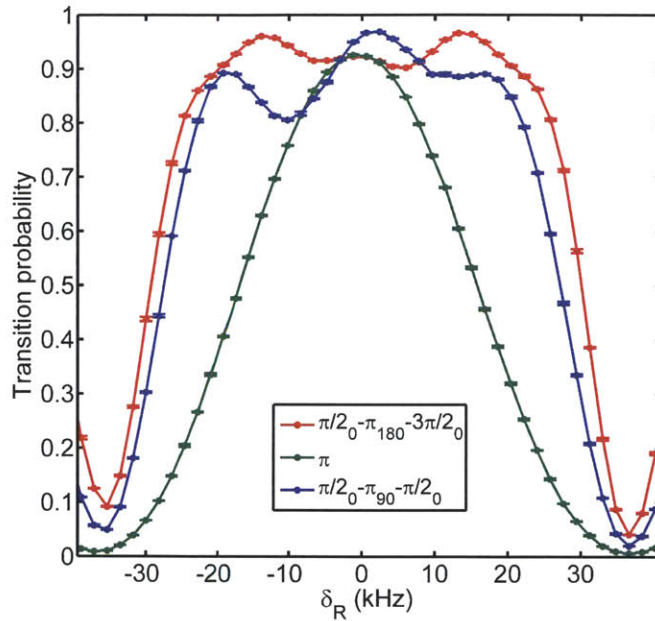


Figure 5-7: Detuning profiles of Doppler insensitive composite Raman pulses ($\Omega_{\text{eff}} = 20$ kHz). The maximum transfer of the composite pulses is 97%, compared to 91% for a π pulse, demonstrating that the composite pulses are less sensitive to Raman beam non-uniformities. The asymmetry in the profile of the $\pi/2_{0^\circ} - \pi_{90^\circ} - \pi/2_{0^\circ}$ is a result of amplitude and phase errors occurring between subpulses.

form comparably well, but it has been shown here that the former composite pulse has clear advantages in both theory and practice.

5.3 Large Area Atom Interferometry with Composite Raman Pulses

As motivated above, the enhanced transfer efficiency demonstrated by composite Raman pulses enables larger momentum splitting in large area atom interferometers. Section 5.1 described how the area enclosed by atomic wavepackets in a $\pi/2 - \pi - \pi/2$ interferometer can be increased by inserting extra Raman pulses (Figs. 5-1, 5-2)². After the initial beam splitter pulse, each augmentation pulse adds $4\hbar k$ of relative momentum between the interferometer arms. Some consideration must be given to how the Raman laser frequency difference is to be tuned during the sequence. The primary reason for this is that, while each subsequent

²In the case of a gravimeter, the atoms are split over a longer baseline, so more *spatio-temporal* area is enclosed.

pulse flips the target internal state from $|F = 4, m_F = 0\rangle$ to $|F = 3, m_F = 0\rangle$ and vice versa, the external momentum states of the wavepackets in each arm differ, resulting in differential Doppler shifts (i.e., the Raman fields cannot be simultaneously resonant in both arms). For instance, with an initial state of $|F = 3, \mathbf{p}_0\rangle$, where the second quantity represents the momentum state, the basis states for the beam splitter are $|F = 3, \mathbf{p}_0\rangle$ and $|F = 4, \mathbf{p}_0 + \hbar\mathbf{k}_{\text{eff}}\rangle$. For the first augmentation pulse in which the Raman beam propagation direction is reversed ($-\mathbf{k}_{\text{eff}}$), the upper arm target state basis is $|F = 4, \mathbf{p}_0 + \hbar\mathbf{k}_{\text{eff}}\rangle$ and $|F = 3, \mathbf{p}_0 + 2\hbar\mathbf{k}_{\text{eff}}\rangle$. The target states of the lower arm are $|F = 3, \mathbf{p}_0\rangle$ and $|F = 4, \mathbf{p}_0 - \hbar\mathbf{k}_{\text{eff}}\rangle$. Therefore, the Raman resonance conditions differ by $4\omega_r$, where ω_r is the Doppler shift from two photon recoils ($\omega_r/2\pi \approx 8.27$ kHz for the cesium D2 transition). By the same argument, the resonance conditions for the second augmentation pulse can be shown to differ by $8\omega_r$. The separation continues to increase by $4\omega_r$ with each additional augmentation pulse in the beam splitter sequence. Here, the large bandwidth of composite Raman pulses is a useful resource, since it can accommodate larger splittings for a given laser power.

To analyze large area interferometer phase shifts, wavepacket amplitudes were calculated by the model described in Appendix B (based on the diagrammatic method described in Stoner *et al.* [60]), assuming a constant Rabi frequency and neglecting spontaneous emission. In the short pulse limit ($t_\tau/T \ll 1$), the phase shift due to a uniform acceleration a in an $N = 1$ interferometer is $\Delta\phi = 3k_{\text{eff}}aT^2 - 4k_{\text{eff}}aT\tau$, where T is the dwell time between the first and middle pulse and τ is the time between augmentation pulses. The second phase term $\propto T\tau$ results from the momentum transfer occurring over time $N\tau$. This expression agrees with the phase shift calculated in [45]. Table 5.1 lists the phase shifts for several interferometers with higher N . The model also confirmed that for arbitrary N , the phase shift introduced by a constant acceleration is canceled by chirping the laser frequency difference at a constant rate, $\alpha_a = \mathbf{k}_{\text{eff}} \cdot \mathbf{a}$ (recall that this is a desirable mode for operating a sensor with the standard three-pulse interferometer as well). For an $N = 1$ interferometer with π pulses as augmentation pulses, the model predicts a maximum contrast of

$$C_{max} = \frac{\Omega_{\text{eff}}^4}{(\Omega_{\text{eff}}^2 + 16\omega_r^2)^2} \sin\left(\frac{\pi\sqrt{\Omega_{\text{eff}}^2 + 16\omega_r^2}}{2\Omega_{\text{eff}}}\right)^4 \quad (5.1)$$

A typical Rabi frequency of 50 kHz gives $C_{max} = 40\%$, meaning that the maximum

Table 5.1: Large area atom interferometer phase shifts induced by a constant acceleration a .

N	$\Delta\phi$
1	$3k_{\text{eff}}aT^2 - 4k_{\text{eff}}aT\tau$
2	$5k_{\text{eff}}aT^2 - 12k_{\text{eff}}aT\tau$
3	$7k_{\text{eff}}aT^2 - 24k_{\text{eff}}aT\tau$
4	$9k_{\text{eff}}aT^2 - 40k_{\text{eff}}aT\tau$

phase SNR improvement over the three-pulse interferometer is only $\approx 20\%$. By contrast, an $N = 1$ and $N = 2$ interferometer with $\pi/2_{0^\circ} - \pi_{180^\circ} - 3\pi/2_{0^\circ}$ composite pulses could achieve a maximum contrast of $>98\%$ for the same Rabi frequency. Even after accounting for the greater losses due to spontaneous emission over the increased pulse area, a large gain in sensitivity is still possible without increasing the laser detuning.

5.3.1 Experiment

With standard π pulses as augmentation pulses, interference was observed for $N = 1$ and $N = 2$ interferometers, with 29% and 10% contrast, respectively. To improve contrast, the augmentation π pulses were replaced with $\pi/2_{0^\circ} - \pi_{180^\circ} - 3\pi/2_{0^\circ}$ composite pulses, leaving the mirror pulse as a π pulse since the Doppler shift in the upper and lower interferometer arms is equal. To minimize spontaneous emission, the Raman laser detuning was set to $\Delta = +3.5$ GHz from the $F = 4 \rightarrow F' = 5$ transition. At this detuning, 0.3% of the atoms spontaneously decay for each π pulse duration. At this rate, spontaneous emission made a relatively small contribution to loss of contrast. With composite Raman pulses, large area interferometer fringes were visible up to $N = 4$, corresponding to a momentum splitting of $18\hbar k$ and factor of nine increase in signal. Fig. 5-8 shows the contrast achieved for $N = 1-4$ with and without composite pulses. The $\pi/2_{0^\circ} - \pi_{90^\circ} - \pi/2_{0^\circ}$ composite pulse did not consistently improve the contrast of large area interferometers. This result is likely implementation-specific, due to the observed composite pulse defects discussed above; nevertheless, this result again highlights the superior intrinsic robustness of the $\pi/2_{0^\circ} - \pi_{180^\circ} - 3\pi/2_{0^\circ}$ composite pulse.

To verify that the observed interference was produced by large area interferometers, the interferometer phase was measured as a function of the chirp rate of the Raman laser frequency difference, $\alpha_L = \frac{d}{dt}(\omega_1 - \omega_2)$, providing a measure of the acceleration scale factor (see Section 2.2.2 for relevant theoretical discussion). It is important to note that the laser

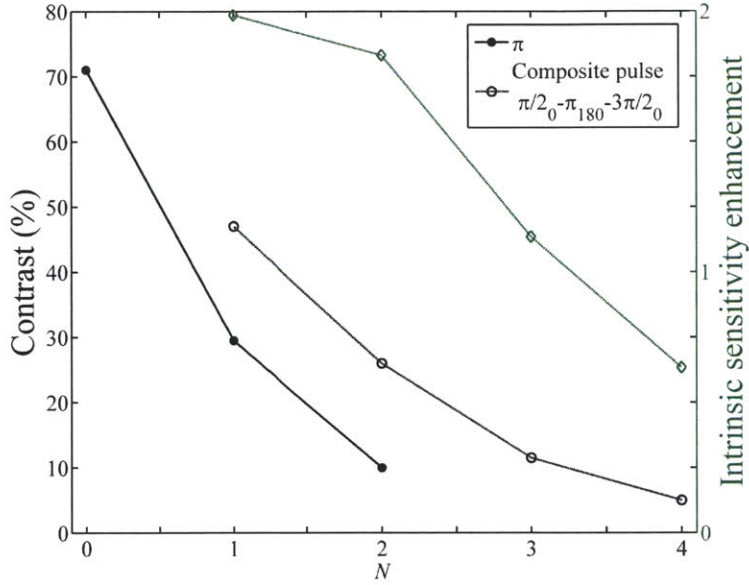


Figure 5-8: Interferometer contrast versus N for large area atom interferometers using π or $\pi/2_{0^\circ} - \pi_{180^\circ} - 3\pi/2_{0^\circ}$ composite pulses as the augmentation pulses. The factor of enhancement in intrinsic sensitivity is plotted for large area interferometers using composite pulses (points represented by open diamonds).

phase of a large area interferometer is not changed, to first order, by substituting the $\pi/2_{0^\circ} - \pi_{180^\circ} - 3\pi/2_{0^\circ}$ composite pulse in place of π pulses. The net phase of the composite pulse is equal to the phase applied during the first subpulse. Fig. 5-9 and Fig. 5-10 show interference fringes of $6\hbar k$, $10\hbar k$, $14\hbar k$, and $18\hbar k$ ($N = 1 - 4$) interferometers. The $18\hbar k$ interferometer phase as a function of α_L is plotted separately in Fig. 5-11. Theoretical curves with the theoretical scale factor (ratio of interferometer phase to α_L) are included, with only amplitude and arbitrary phase offset as free parameters. All four cases show good agreement with the theory.

Based on the measured contrast, the intrinsic sensitivity of the large area interferometers is inferred as the ratio of the increase in the inertial phase shift (over the three-pulse interferometer) to the factor of contrast loss. This figure of merit describes the gain in sensitivity assuming other sources of noise remain constant. Fig. 5-8 shows the factor by which each large area interferometer enhances the intrinsic sensitivity over the three-pulse interferometer. Currently, the maximum enhancement is approximately a factor of two, realized by the $6\hbar k$ ($N = 1$) interferometer, with lower improvements by the $N = 2, 3$ interferometers. The $N = 4$ interferometer does not currently improve sensitivity. Interestingly, similar gains

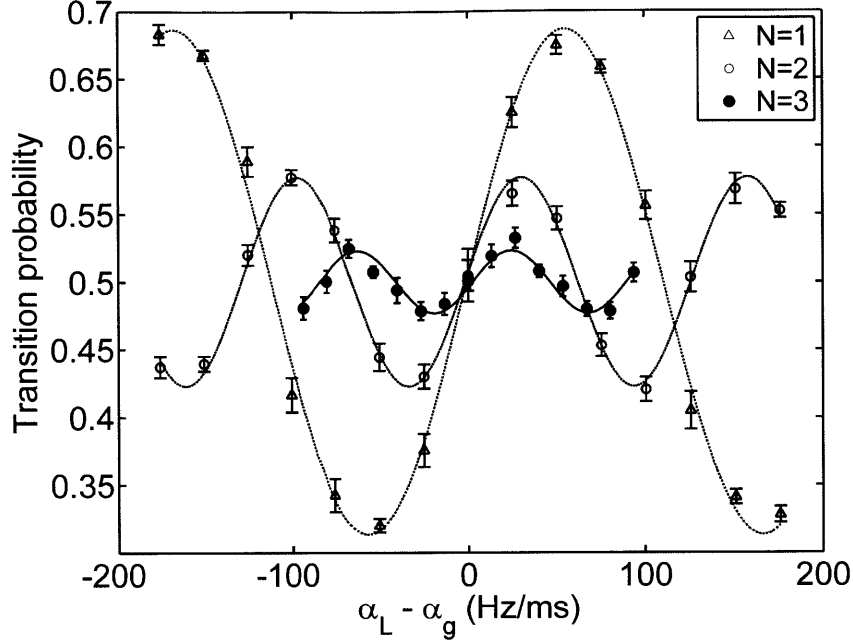


Figure 5-9: Interference fringes for $6\hbar k$, $10\hbar k$, and $14\hbar k$ ($N = 1 - 3$), using $\pi/2_{0^\circ} - \pi_{180^\circ} - 3\pi/2_{0^\circ}$ composite pulses as augmentation pulses, with $2T = 2.5$ ms and $\tau = 40 \mu\text{s}$ (each point represents an average of four shots). The fringes were scanned by varying the chirp rate of the Raman laser frequency difference (α_L) about the linearly-increasing Doppler shift induced by gravity (α_g). The theoretical curves use only amplitude and arbitrary phase offset as free parameters.

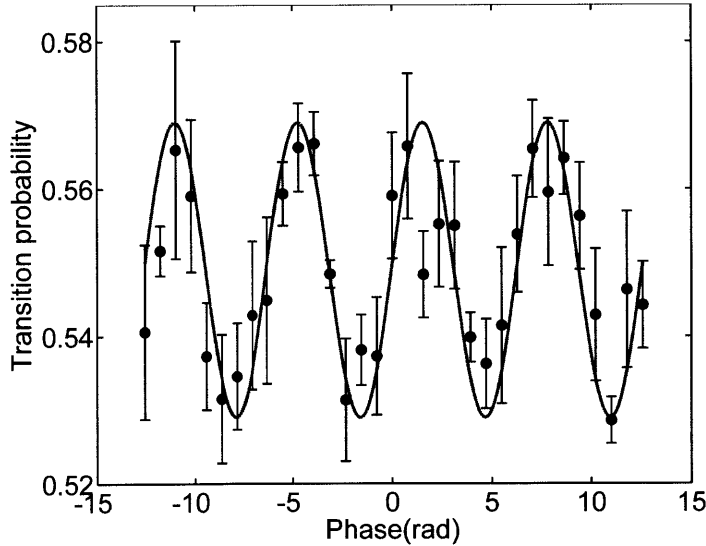


Figure 5-10: Interference fringes of an $18\hbar k$ ($N = 4$) interferometer using $\pi/2_{0^\circ} - \pi_{180^\circ} - 3\pi/2_{0^\circ}$ composite pulses, with $2T = 2$ ms and $\tau = 40 \mu\text{s}$. Each point represents an average of four shots.

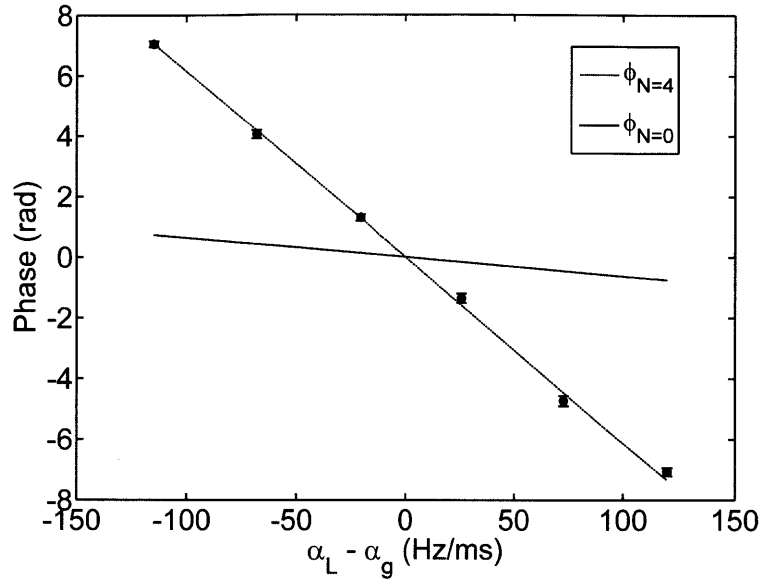


Figure 5-11: Scale factor of the $18\hbar k$ ($N = 4$) interferometer with $\pi/2_{0^\circ} - \pi_{180^\circ} - 3\pi/2_{0^\circ}$ composite pulses ($2T = 2$ ms and $\tau = 40$ μ s), compared to the scale factor of a $2\hbar k$ interferometer with the same interrogation time. Each point was calculated from a least-squares fit of four interferograms. The theoretical lines use only an arbitrary phase offset as a free parameter.

in intrinsic sensitivity were also achieved when using atom samples at μ K temperatures (no velocity selection after the MOT). This result underscores the advantages provided by composite Raman pulses for sensors operating at high repetition rates, at which velocity selection may be precluded by short MOT loading periods.

Several aspects of the experimental apparatus limit the realized gains in sensitivity with large area interferometers. First, extended light pulse sequences are more susceptible to phase shifts from Raman beam phase front distortions. In the presence of these distortions, the transverse motion of an atom imprints a spatially-varying phase at each pulse. If the atom were motionless, the local offset in phase would be common mode. Since the Raman beam is retroreflected, only the vacuum cell window above the atoms, a quarter waveplate, and the retroreflecting mirror introduce phase front errors. Nevertheless, the vacuum cell windows are only rated to $\lambda/10$ flatness. Since the total phase error is proportional to the number of pulses, an $18\hbar k$ ($N = 4$) interferometer with 19 pulses creates a spatial phase distribution of nearly 2π (of course, each atom samples only a small fraction of the beam). Secondly, large area interferometers are more susceptible to vibrations, which also introduces phase noise proportional to the number of light pulses. As discussed in Chapter 4, the

retroreflecting mirror that serves as the inertial reference is not actively stabilized, and experiences high frequency vibrations from the laboratory environment. Finally, imperfections in the composite pulses degrade their transfer efficiency. Small improvements in transfer efficiency would result in large gains in contrast, scaling as $\sim \xi^{4N}$, where ξ is the transfer efficiency.

Systematic phase shifts induced by AC Stark shifts in large area interferometers were also measured to diagnose whether or not large area atom interferometers were more sensitive to AC Stark shifts. The magnitude of these shifts were observed to be similar in large area interferometers and the three-pulse interferometer (variation of ~ 0.01 rad for differential AC Stark shifts of $\sim 0.1\Omega_{\text{eff}}$); i.e., the insertion of extra pulses did not appear to significantly increase the sensitivity of the interferometer to Stark shifts.

5.4 Summary and Improvements

Composite Raman pulses were demonstrated to improve transfer efficiency over that of a single π pulse because of their insensitivity to atom temperature and the Raman beam intensity distribution. The broadband population inversion realized by these pulses enabled large area atom interferometry with Raman transitions, with momentum splittings up to $18\hbar k$. This is the largest reported momentum transfer for an inertially-sensitive Raman pulse atom interferometer. An $18\hbar k$ interferometer increases the inertial phase shift by a factor of approximately nine, without increasing interrogation time. This work is also the first reported demonstration of optical composite pulse techniques in an inertially-sensitive atom interferometer. Raman atom optics offer the advantage of permitting hotter atoms than other LMT atom optics (e.g., multi-photon Bragg transitions), which could allow for rapid interrogation. Additionally, composite Raman pulses that are robust to Raman beam non-uniformity may prove beneficial in dynamic applications, in which the ensemble of atoms is not guaranteed to remain in the beam center throughout the interrogation. Atoms displaced transversely in a Gaussian beam experience a broader distribution of laser power across the ensemble, due to the larger local intensity gradient. Importantly, these advantages are technologically favorable for inertial sensors demanding high repetition rates and robust operation in dynamic environments.

In the current implementation, the $N = 1 - 3$ interferometers achieve a net gain in intrinsic sensitivity, with a maximum gain by a factor of two. The $N = 4$ interferometer loses contrast by a factor larger than the increase in the inertial phase shift, and so is not useful for a sensor. Currently, however, the contrasts achieved with large area interferometers are far from theoretical limits. Interferometer contrast is primarily limited in this apparatus by defects in the implementation of composite Raman pulses, high frequency platform vibrations, and the phase front quality of the optics. With realistic improvements to the Raman beam optics and RF electronics, higher contrasts should be possible, enabling yet larger gains in the realized sensitivity. Ultimately, for a given laser power, the performance of large area interferometers are limited by differential Doppler shifts, and increasing decoherence from spontaneous emission as the pulse area grows with N . Of course, spontaneous emission rates could be reduced by using higher laser power and laser detuning, which would also accommodate larger differential Doppler shifts. With a Rabi frequency of ~ 100 kHz, a useful $N = 4$ or larger interferometer should be feasible, though a lower N interferometer might still yield higher sensitivity in practice. In the future, more advanced composite pulse sequences with temporal intensity or frequency shaping could improve upon the robustness offered by the simple composite pulses in this work.

Chapter 6

Coherent Population Trapping in Raman Pulse Atom Interferometry

At present, most implementations of light pulse atom interferometers use stimulated Raman transitions as atom optics. Both existing and future high precision measurements using atom interferometry demand critical investigations of light-based error sources, such as higher order light shifts [65]. Analyses of stimulated Raman transitions in the atom interferometry literature commonly neglect the effects of spontaneous emission, or treat it solely as a source of decoherence (e.g., [57] and the basic theory outlined in Chapter 2). As described in previous chapters, typical Raman atom optics use fields with GHz-scale single-photon detunings, so that spontaneous emission produces a minor or negligible source of decoherence. An additional consequence of spontaneous emission, however, is coherent population trapping (CPT), or the coherent transfer of atomic population to a decoupled (dark) superposition state.

CPT has been extensively analyzed and observed experimentally in three-level (Λ) atomic systems where Raman resonances are excited by bichromatic laser fields [95–97]. Since the discovery of the effect, it has been exploited for precision measurement applications including chip-scale atomic clocks [98] and atomic magnetometry [99], in which narrow RF resonances are achieved in steady-state laser operation. However, the possible impact of CPT in atom interferometry with stimulated Raman transitions has not been discussed in the literature. This chapter addresses the effect of transient CPT on Raman pulse atom interferometers, and

it is argued that interferometer phase shifts of multiple milliradians in amplitude have likely been produced in previous precision measurements. While the claimed accuracies in past work were not significantly affected by neglecting this source of bias, due to the large phase shifts being measured with long interrogation times, the characterization of such systematic effects is critical for high precision inertial sensing. For instance, a 1 mrad bias for a $T = 1$ ms accelerometer amounts to an acceleration error of $\approx 7 \mu\text{g}$.

The chapter begins with a basic description of coherent population trapping, and then presents an elementary density matrix theory for calculating Raman pulse output state populations and coherences. It is shown that, by including spontaneous emission, the analytical model predicts CPT effects. To complement the theory, experimental measurements are presented of dark state coherences and population differences induced in cold cesium atoms by Raman pulses. Finally, a simple argument is proposed that Raman pulse-induced dark state coherences shift the phase of a $\pi/2 - \pi - \pi/2$ interferometer. This discussion also suggests a method for suppressing the error.¹

6.1 Background

Coherent population trapping is a quantum mechanical effect involving interference between transitions in a multi-level atom. The simplest example is the irradiation of a three-level Λ atom by two phase-coherent laser fields, whose frequency difference is close to the ground state splitting ($\omega_e - \omega_g$), as shown in Fig. 6-1. For the case of large single-photon detuning Δ from the optical transitions, this interrogation is of obvious relevance to atom interferometry with stimulated Raman transitions. Initially, however, consider the case in which both fields are optically resonant and satisfy the Raman resonance condition. One finds in experiment that, despite the presence of two fields coupling to strong optical transitions, the fluorescence of the atoms is dramatically suppressed around Raman resonance. The laser fields have pumped the atoms into a non-absorbing state that is a superposition of the two ground states. Figure 6-2 shows the steady-state excited state population as a function of the Raman detuning, in which the trapping of population in this coherent dark state is evident.

¹This chapter is based on Butts *et al.*, “Coherent Population Trapping in Raman-Pulse Atom Interferometry,” *Physical Review A* **84**, 043613 (2011) [62].

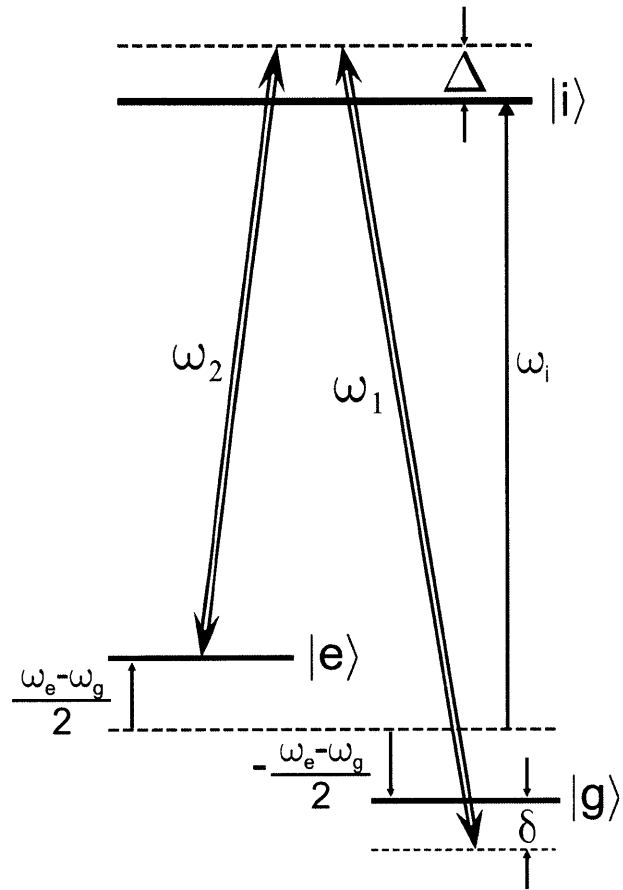


Figure 6-1: Diagram of the three-level (Λ) atom and laser fields considered in Section 6.2.

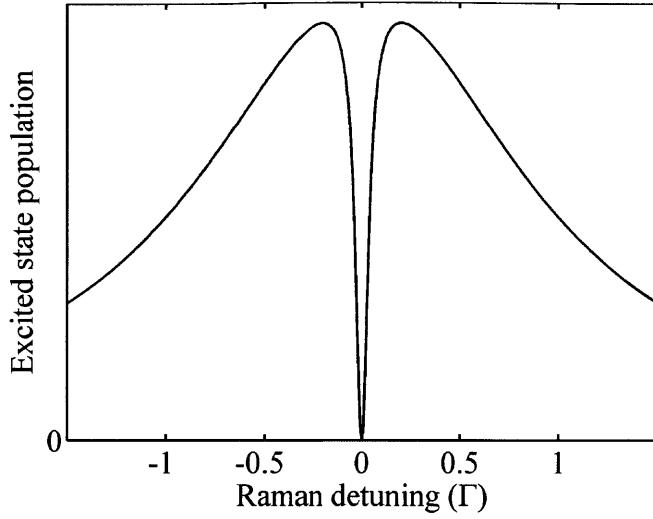


Figure 6-2: Steady-state excited state population as a function of Raman detuning, assuming typical parameters for an alkali atom and two laser fields with equal intensity. Γ is the natural linewidth. The lineshape exhibits a narrow resonance induced by coherent population trapping.

Interestingly, if one constructs the Hamiltonian for the atom and the two laser fields and finds the energy eigenstates, two of the resulting eigenstates are

$$\begin{aligned}
 |C\rangle &= \frac{\Omega_1|g\rangle + \Omega_2|e\rangle}{\sqrt{\Omega_1^2 + \Omega_2^2}} \\
 |NC\rangle &= \frac{\Omega_2|g\rangle - \Omega_1|e\rangle}{\sqrt{\Omega_1^2 + \Omega_2^2}}
 \end{aligned} \tag{6.1}$$

where Ω_j is the Rabi frequency associated with the field j (ignoring cross-coupling), and the states $|C\rangle$ and $|NC\rangle$ denote ground state superposition states that are coupled and uncoupled, respectively, from the optical fields. These states are commonly referred to as “bright” and “dark” states. The probability amplitudes for the two transitions interfere destructively, and population accumulates in the dark state, from which the atom cannot be excited. As mentioned above, this phenomenon has been theoretically and experimentally investigated, as well as employed in precision measurements [100]. Previous work, however, has focused on steady-state CPT with near-resonant optical fields. In this chapter, the impact of transient CPT effects is investigated in the novel context of Raman pulse atom interferometry, with GHz-scale single-photon detunings.

6.2 Raman Pulse Theory including Spontaneous Emission

Stimulated Raman transitions have been previously described in atom interferometry using Schrödinger formalism [57,60,70], in which spontaneous emission effects were not considered. The basic theory outlined in Chapter 2 uses such an approach. For typical \sim GHz detuned fields, spontaneous emission during Raman pulses causes minimal decoherence. However, it will be shown that the occurrence of spontaneous emission also results in the formation of dark state coherences, even in the large detuning regime of relevance to Raman pulse atom interferometry.

This section summarizes a three-state density matrix theory for Raman pulse physics that motivates and qualitatively describes the experimental results. While this model only approximately treats the more complex structure of a real atom, it captures the essential physics and permits an analytic solution. The theory includes spontaneous emission in a three-level (Λ) atom, depicted in Fig. 6-1. Prior to exhibiting solutions, the problem is recast in terms of a pseudospin vector polarization on a Bloch sphere, similar to the approach outlined in Section 2.1.1. It is also seen that in addition to “torquing” the initial polarization state in a fashion exactly analogous to RF spin resonance in nuclear magnetic resonance, the Raman pulse also induces a dark state polarization.

Consider an atom with two closely-spaced ground states, $|g\rangle$ and $|e\rangle$, and a single excited state $|i\rangle$ (Fig. 6-1). Ground state $|g\rangle$ ($|e\rangle$) is coupled by electric field \mathbf{E}_1 (\mathbf{E}_2) to $|i\rangle$. The analysis is placed in a reference frame co-moving with the atom in $|g\rangle$, and therefore the frequencies of the applied fields depend on the motional state of the atom. The fields \mathbf{E}_1 , \mathbf{E}_2 are defined as²

$$\mathbf{E}_1 = \hat{e}_1 \varepsilon_1 \cos [\phi_1(t) + \phi_1^0] \quad (6.2)$$

$$\mathbf{E}_2 = \hat{e}_2 \varepsilon_2 \cos [\phi_2(t) + \phi_2^0] \quad (6.3)$$

with $\phi_1(t) = \int_0^t [\omega_1(t') - \mathbf{k}_1 \cdot \hat{e}_z \dot{z}(t')] dt'$, $\phi_2(t) = \int_0^t [\omega_2(t') - \mathbf{k}_2 \cdot \hbar \mathbf{k}_{\text{eff}}/m - \mathbf{k}_2 \cdot \hat{e}_z \dot{z}(t')] dt'$, polarization vectors \hat{e}_j , amplitudes ε_j , time-dependent frequencies ω_j , wavevectors \mathbf{k}_j , effective

²The notation used in this chapter differs slightly from the notation in Chapter 2, but should be clear in given definitions.

wavevector $\mathbf{k}_{\text{eff}} = \mathbf{k}_1 - \mathbf{k}_2$, and phases ϕ_j^0 for field \mathbf{E}_j . The two wavevectors are assumed to be either parallel or anti-parallel to each other, with both aligned along \hat{e}_z , so that the derivation accounts for both co-propagating (Doppler insensitive) and counter-propagating (Doppler sensitive) cases. The two-photon recoil velocity $\hbar\mathbf{k}_{\text{eff}}/m$ is included in the velocity of an atom in state $|e\rangle$, which couples to \mathbf{E}_2 ; the Doppler shift of \mathbf{E}_2 thus contains a recoil contribution. The optical phases are defined with time-dependent frequencies to address the interrogation of atoms accelerating relative to the Raman beams, which is applicable to the gravimeter configuration in the experiments. The choice of reference frame here is different from the canonical laboratory frame approach described in Chapter 2, and the resulting equations of motion have a slightly different appearance (of course, interferometer phase shifts can be derived by either framework).

The energy origin for the atom is chosen to be the midpoint between the ground state energies $\hbar\omega_e$ and $\hbar\omega_g$, as shown by Fig. 6-1. The laser detuning Δ from the optical resonances, as well as the Raman detuning δ between the laser frequency difference and the ground state energy level splitting, are indicated in Fig. 6-1. These detunings are defined here as

$$\delta(t) \equiv [\omega_1(t) - \omega_2(t)] - \left[(\omega_e - \omega_g) + \frac{\hbar\mathbf{k}_{\text{eff}}^2}{2m} - \frac{\hbar}{2m}(k_1^2 - k_2^2) + \mathbf{k}_{\text{eff}} \cdot \dot{z}(t)\hat{e}_z \right] \quad (6.4)$$

$$\Delta \equiv \frac{\omega_1(t) + \omega_2(t)}{2} - \left[\omega_i - \frac{1}{2} \left(\frac{\hbar\mathbf{k}_{\text{eff}}^2}{2m} - \frac{\hbar}{2m}(k_1^2 - k_2^2) - (\mathbf{k}_1 + \mathbf{k}_2) \cdot \dot{z}(t)\hat{e}_z \right) \right] \quad (6.5)$$

The total Hamiltonian, including both internal (diagonal elements) and atom-field interaction (off-diagonal elements) Hamiltonians, is

$$\hat{H} = \frac{\hbar}{2} \begin{bmatrix} \omega_e - \omega_g & \Omega_2 e^{i\phi_2(t)} & 0 \\ \Omega_2^* e^{-i\phi_2(t)} & 2\omega_i & \Omega_1^* e^{-i\phi_1(t)} \\ 0 & \Omega_1 e^{i\phi_1(t)} & -(\omega_e - \omega_g) \end{bmatrix} \quad (6.6)$$

where $\Omega_j = |\Omega_j| e^{i\phi_j^0}$ is the complex Rabi frequency associated with the coupling for field \mathbf{E}_j . The time dependence of the Hamiltonian can be factored out using a unitary transformation

defined by

$$\begin{aligned} \hat{U}_{\text{int}} \equiv & \exp \left\{ -\hat{P}_e \cdot \frac{i}{2} [(\omega_e - \omega_g) + \delta(t)] \right\} + \exp \left\{ \hat{P}_g \cdot \frac{i}{2} [(\omega_e - \omega_g) + \delta(t)] \right\} \\ & + \exp \left[-\hat{P}_i \cdot i (\Delta + \omega_i) \right] \end{aligned} \quad (6.7)$$

where \hat{P}_e , \hat{P}_i , \hat{P}_g are the Hilbert space projection operators onto states $|e\rangle$, $|i\rangle$, and $|g\rangle$, respectively. In terms of Eq. (6.6), the Hamiltonian can be written as

$$\hat{H} = \hbar \hat{U}_{\text{int}} \begin{bmatrix} \frac{1}{2}(\omega_e - \omega_g) & \frac{1}{2}\Omega_2 & 0 \\ \frac{1}{2}\Omega_2^* & \omega_i - \frac{1}{2}(\omega_e + \omega_g) & \frac{1}{2}\Omega_1^* \\ 0 & \frac{1}{2}\Omega_1 & -\frac{1}{2}(\omega_e - \omega_g) \end{bmatrix} \hat{U}_{\text{int}}^\dagger \quad (6.8)$$

The density matrix ρ for the three-level system is

$$\rho = \begin{bmatrix} \rho_{ee} & \rho_{ei} & \rho_{eg} \\ \rho_{ie} & \rho_{ii} & \rho_{ig} \\ \rho_{ge} & \rho_{gi} & \rho_{gg} \end{bmatrix} \quad (6.9)$$

The time rate of change of the density matrix due to spontaneous emission is

$$\dot{\rho}_{SE} = \begin{bmatrix} \frac{\Gamma}{2}\rho_{ii} & -\frac{\Gamma}{2}\rho_{ei} & 0 \\ -\frac{\Gamma}{2}\rho_{ie} & -\Gamma\rho_{ii} & -\frac{\Gamma}{2}\rho_{ig} \\ 0 & -\frac{\Gamma}{2}\rho_{gi} & \frac{\Gamma}{2}\rho_{ii} \end{bmatrix} \quad (6.10)$$

where Γ is the average rate of spontaneous decay from the excited state [101]. For simplicity, this decay rate matrix assumes a closed system in which excited state decay is restricted to the two ground states with equal branching ratios, and neglects any decay of the ground state coherences. The equation of motion for the density matrix is

$$\frac{d\rho}{dt} = \frac{1}{i\hbar} [\hat{H}, \rho] + \dot{\rho}_{SE} \quad (6.11)$$

This equation is then transformed to the interaction picture using \hat{U}_{int} and by representing

the interaction picture density matrix R_{int} as

$$R_{\text{int}} \equiv \begin{bmatrix} \rho_{ee} & r_{ei} & r_{eg} \\ r_{ie} & \rho_{ii} & r_{ig} \\ r_{ge} & r_{gi} & \rho_{gg} \end{bmatrix} = \hat{U}_{\text{int}}^\dagger \rho \hat{U}_{\text{int}} \quad (6.12)$$

The equations governing the ground-excited state coherences r_{ei} and r_{gi} can be simplified, first by noting that for typical experimental conditions $|\delta(t)| \ll |\Delta|$. Adiabatic elimination, wherein a large rate is taken to dominate time evolution, permits an approximate solution for the ground-excited state coherences:

$$\frac{d}{dt} R_{\text{int}} \cong \frac{d}{dt} \begin{bmatrix} \rho_{ee} & 0 & r_{eg} \\ 0 & \rho_{ii} & 0 \\ r_{ge} & 0 & \rho_{gg} \end{bmatrix} \quad (6.13)$$

It can then be shown, from the approximate equation of motion for R_{int} , that

$$r_{ei} \cong \frac{\Omega_1 r_{eg} - \Omega_2 (\rho_{ii} - \rho_{ee})}{2\Delta - i\Gamma} \quad (6.14)$$

$$r_{ig} \cong \frac{\Omega_1^* (\rho_{gg} - \rho_{ii}) + \Omega_2^* r_{eg}}{2\Delta + i\Gamma} \quad (6.15)$$

Substituting these relations back into the equation of motion, and making the additional assumption that the excited state population $\rho_{ii} \ll 1$, reduces the original equation of motion to an equation for populations ρ_{ee} , ρ_{gg} , and coherence r_{eg} . At this point, one can define components for a pseudospin $\mathbf{P}(t)$ on a Bloch sphere (as before in Section 2.1.1):

$$P_j(t) = \text{Tr} \left[\begin{bmatrix} \rho_{ee} & r_{eg} \\ r_{ge} & \rho_{gg} \end{bmatrix} \cdot \sigma_j \right], \quad j = x, y, z \quad (6.16)$$

where $\{\sigma_j\}$ are the Pauli spin matrices. Thus,

$$\mathbf{P}(t) = \begin{bmatrix} P_x(t) \\ P_y(t) \\ P_z(t) \end{bmatrix} = \begin{bmatrix} 2\text{Re}[r_{eg}] \\ -2\text{Im}[r_{eg}] \\ \rho_{ee} - \rho_{gg} \end{bmatrix} \quad (6.17)$$

A similar transformation was used in [24], although spontaneous emission was not considered.

In a lengthy but elementary analysis, the pseudospin components from Eq. (6.17) are substituted into the equation of motion for R_{int} and adiabatic elimination is applied as per Eq. (6.13), assuming that $\rho_{ii} \ll 1$. The resulting vector equation of motion for $\mathbf{P}(t)$ is

$$\frac{d}{dt} [\mathbf{P}(t) - \mathbf{P}_{\text{dark}}] + [\mathbf{P}(t) - \mathbf{P}_{\text{dark}}] \times \boldsymbol{\Omega} + \Gamma_{\text{loss}} [\mathbf{P}(t) - \mathbf{P}_{\text{dark}}] \cong -\hat{e}_z \Gamma_{\text{source}} \quad (6.18)$$

where, using notation similar to that of Chapter 2,

$$\begin{aligned} \mathbf{P}_{\text{dark}} &\equiv -\frac{\boldsymbol{\Omega}}{\Omega_{e,AC} + \Omega_{g,AC}} \\ \Gamma_{\text{source}} &= \frac{\Gamma \delta}{2\Delta} \\ \Gamma_{\text{loss}} &= \frac{\Gamma}{2\Delta} (\Omega_{e,AC} + \Omega_{g,AC}) \\ \Omega_{j,AC} &= \frac{|\Omega_j|^2}{4\Delta} \\ \delta_{AC} &= \Omega_{e,AC} - \Omega_{g,AC} \\ \boldsymbol{\Omega} &= \Omega [\cos \theta \hat{z} + \sin \theta (\cos \phi \hat{x} + \sin \phi \hat{y})] \\ \Omega &= \sqrt{|\Omega_{\text{eff}}|^2 + (\delta_{AC} - \delta)^2} \\ \cos \theta &= \frac{\delta_{AC} - \delta}{\Omega}, \quad \sin \theta = \frac{|\Omega_{\text{eff}}|}{\Omega} \\ \phi &= \phi_1^0 - \phi_2^0 \\ \Omega_{\text{eff}} &= \frac{\Omega_1 \Omega_2^*}{2\Delta} = \frac{|\Omega_1| |\Omega_2| e^{i\phi}}{2\Delta} \end{aligned} \quad (6.19)$$

Eq. (6.18) is analogous to the dynamics for a classical magnetization subjected to a magnetic field torque and decoherence, with a source of longitudinal magnetization. This equation can be solved with the aid of a concise notation. Given a fixed vector $\alpha = \alpha \hat{a}$, one can define an exponentiated cross product operator acting on an arbitrary vector \mathbf{V} as

$$\begin{aligned} \exp(\alpha(\hat{a} \times)) \mathbf{V} &= [\cos(\alpha)(\mathbf{1} \cdot) + \sin(\alpha)(\hat{a} \times) + (1 - \cos \alpha) \hat{a}(\hat{a} \cdot)] \mathbf{V} \\ &= \cos(\alpha) \mathbf{V} + \sin(\alpha) (\hat{a} \times \mathbf{V}) + (1 - \cos \alpha) \hat{a} (\hat{a} \cdot \mathbf{V}) \end{aligned} \quad (6.20)$$

where $\mathbf{1}$ is the identity matrix. This exponentiated cross product operator acts to rotate

\mathbf{V} about $\hat{\alpha}$ in the right-handed sense by an angle α . The expression in Eq. (6.20) can be obtained by Taylor expansion and the application of cross product rules. It is simple to show that the derivative of this operator is

$$\frac{d}{d\alpha} \exp[\alpha(\hat{\alpha} \times)] = \hat{\alpha} \times \exp[\alpha(\hat{\alpha} \times)] \quad (6.21)$$

With the rotation operator, it can be shown that the solution to Eq. (6.18) for the time-dependent pseudospin is

$$\begin{aligned} \mathbf{P}(t) = & \exp \left[\left(\Omega(\hat{\Omega} \times) - \Gamma_{\text{loss}} \mathbf{1} \right) t \right] \cdot \mathbf{P}(0) \\ & + \left\{ \exp \left[\left(\Omega(\hat{\Omega} \times) - \Gamma_{\text{loss}} \mathbf{1} \right) t \right] - \mathbf{1} \right\} \left\{ \mathbf{P}_{\text{dark}} - \left[-\Omega(\hat{\Omega} \times) + \Gamma_{\text{loss}} \mathbf{1} \right]^{-1} \cdot (\Gamma_{\text{source}} \hat{e}_z) \right\} \end{aligned} \quad (6.22)$$

Note that Γ_{loss} cannot vanish on physical grounds, so that the inverse in the final term of Eq. (6.22) always exists. This solution represents the dynamics of the atomic pseudospin in the rotating frame. As expected, the action of the Raman pulse on the initial polarization is to rotate it about the Raman effective drive field, $\mathbf{\Omega}$. There is also a slow loss of coherence due to spontaneous emission. However, in addition to the torquing action on the initial polarization, another polarization is induced, with an asymptotic value of

$$\mathbf{P}(t \rightarrow \infty) = -\mathbf{P}_{\text{dark}} + \left[-\Omega(\hat{\Omega} \times) + \Gamma_{\text{loss}} \mathbf{1} \right]^{-1} \cdot (\Gamma_{\text{source}} \hat{e}_z) \quad (6.23)$$

On resonance, this expression simplifies to $\mathbf{P}(t \rightarrow \infty) = -\mathbf{P}_{\text{dark}}$. Recalling the definition for \mathbf{P}_{dark} , note that for negative laser detunings ($\Delta < 0$), the asymptotic polarization is induced parallel to the effective drive field $\mathbf{\Omega}$. The dark polarization is aptly named since $\hat{\Omega} \times \mathbf{P}_{\text{dark}} = 0$, i.e., the optical fields do not couple to it.

As stated earlier, this simple three-level theory can only be expected to provide a qualitative description of Raman pulse physics in the real ground state hyperfine manifold of an alkali atom. In this closed system, spontaneous decay must return atoms to one of the coupled ground states. In an alkali atom, however, spontaneous emission can remove an atom from further interaction via decay to an uncoupled ground state (e.g., any $m_F \neq 0$ level in the ground state manifolds). The theory also neglects the effect of multiple excited states. Selec-

tion rules permit two excited state sublevels to act as intermediaries for Raman transitions in typical alkali atomic hyperfine structure. The coupling of the ground states to the two intermediaries is comparable for the range of detunings considered here ($\Gamma \ll \Delta \ll \omega_e - \omega_g$). Therefore, one expects substantial deviations between the present theory and experiment. Since no ground state superposition is be dark with respect to two possible intermediary excited states, continued coupling to the field should result in decreasing magnitudes of induced polarization at long pulse lengths. The theory, by contrast, predicts large asymptotic polarizations, of magnitude approaching unity for excitation close to Raman resonance.

It is important to note that for off-resonant Raman pulses, the theory predicts that a population difference between the ground states is induced in addition to a dark state coherence (i.e., $P_z \neq 0$). In addition, the time evolution of the polarization, when scaled by the pulse area Ωt , is predicted to be independent of the effective Rabi frequency. The approximations employed by the theory would not appear to compromise this prediction. While a more accurate numerical simulation of a real atom is not included in this work, such a study is certainly feasible, and constitutes an interesting step for future work. For instance, such a simulation could address the potential for variation in the magnitude of the effect in other atomic species (e.g., rubidium). In the next section, experimental tests of the qualitative predictions of the theory are described.

6.3 Experiment

The approach of these experiments differs from previous CPT-related investigations in that non-steady-state CPT effects were produced and detected with atom interferometry in a cold atom ensemble, rather than the conventional approach in which pump and probe laser fields induce and detect steady-state CPT effects in a vapor cell (e.g., [97]). The basic method was to prepare a sample of cold cesium atoms in the $|F = 3, m_F = 0\rangle$ ground state, apply long Raman pulses in free space to induce CPT, and observe the resultant population and coherences. As will be described in detail below, care was taken to discriminate against the contribution of the initial polarization of the atoms.

CPT-induced population differences and coherences were observed to be induced by both Doppler insensitive and Doppler sensitive Raman pulses. Use of Doppler insensitive Raman

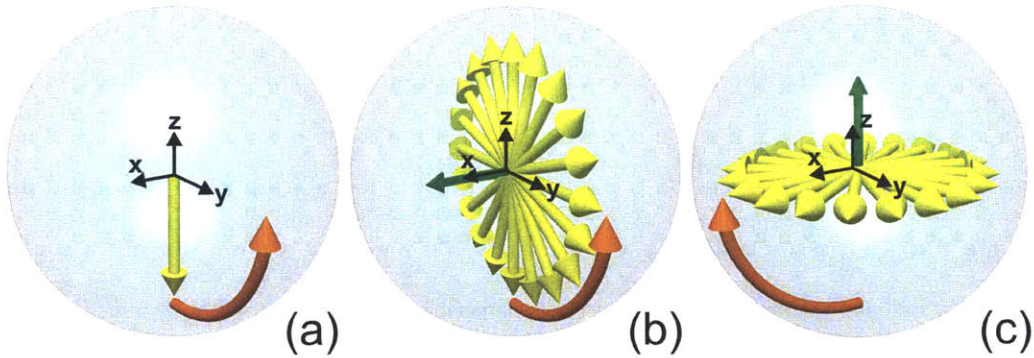


Figure 6-3: Bloch sphere representation of a two-pulse experiment for detecting coherently trapped population induced by a velocity insensitive Raman pulse. (a) The first Raman pulse rotates the initial polarization along $-z$ about Ω on the x axis. (b) At long first pulse durations, the initial polarization of the ensemble is dispersed in the $y - z$ plane by a spatially-varying Rabi frequency. A polarization along the effective drive field (vector along x) is induced by CPT. (c) After a brief dwell time, a $\pi/2$ pulse at a phase 90° (-90°) relative to the first pulse rotates the induced coherence onto z , where it is measured as a population difference. The initial ensemble contributes no net polarization.

pulses afforded an expedient path to a first demonstration, because of the ease of implementation and the suppression of systematic effects due to atom temperature and laboratory vibrations. However, inasmuch as Doppler insensitive Raman interferometers are used mostly as an experimental diagnostic, Doppler insensitive CPT effects are of limited practical interest. Doppler sensitive Raman pulses serve as atom optics in high precision atom interferometers, so CPT effects induced by such pulses have implications for precision measurement results obtained with Raman atom interferometry (e.g., [25, 26]).

6.3.1 Doppler Insensitive Raman pulses

Experiments with Doppler insensitive Raman pulses probed the dependence of CPT effects on Raman pulse duration, Raman detuning, Rabi frequency, and laser detuning. In addition to providing an expedient demonstration of CPT effects, these measurements also provided an estimate of the effect that could be expected to be produced by Doppler sensitive Raman pulses.

To distinguish coherently trapped population from population remaining in bright states, Raman pulses with duration greater than $10t_\pi$ were applied to dephase the ensemble by the spatial distribution of Rabi frequencies in the Raman beam. The resulting visibility of

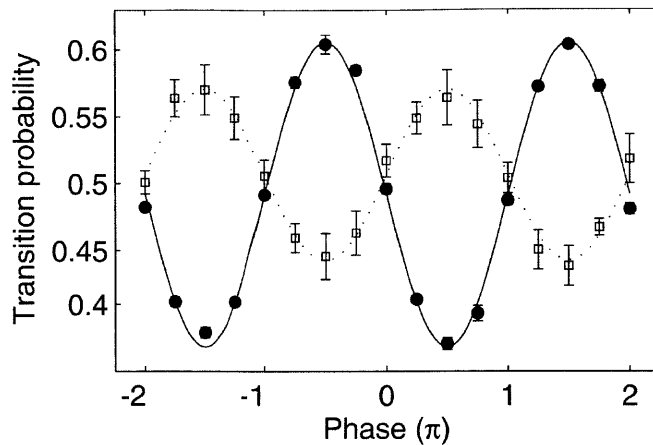


Figure 6-4: Dark state population observed with Doppler insensitive $75\pi - \pi/2$ interferometers at positive (filled circles: $\Delta = -1.25$ GHz; open squares: $\Delta = +2.5$ GHz). As predicted by the theory in Section 6.2, CPT induces dark state polarizations at opposite phases for positive/negative laser detunings.

Rabi oscillations of the initial polarization was less than 1% (in other words, $\langle P_z \rangle = 0$ for the ensemble-averaged pseudospin and the average transition probability was 50%). When subjected immediately to population readout, the ensemble appeared completely dephased; i.e., the population trapped in a dark superposition state had no P_z component. However, by subsequently applying a $\pi/2$ pulse, as depicted in Fig. 6-3, the coherence was rotated into an observable population difference. An induced coherence parallel to the effective field Ω of the first pulse would then produce minimum (maximum) population transfer at $\pm 90^\circ$. Interferograms obtained by varying the $\pi/2$ pulse phase (Fig. 6-4) indicate that the induced coherence was parallel to the effective drive field for negative Δ and anti-parallel for positive Δ , consistent with a CPT effect. Negative Δ data depicted in Fig. 6-4 are expressed in terms of transition probability with peak-to-peak variation of about 23%. On the Bloch sphere of Fig. 6-3, this corresponds to an induced polarization of magnitude 0.23 on a scale where all atomic population exclusively in one ground state corresponds to a polarization of magnitude unity.

Fig. 6-5 depicts the measured dark state population induced by resonant Raman pulses for a range of pulse durations. Recalling that the theory predicts a trapped population scaling with the pulse area, the pulse duration is scaled in units of t_π . Similar curves were obtained with Rabi frequencies over a range of 20-100 kHz, which is in accord with the theory. For pulse areas less than 40π , the trapped population increased linearly. Trapping

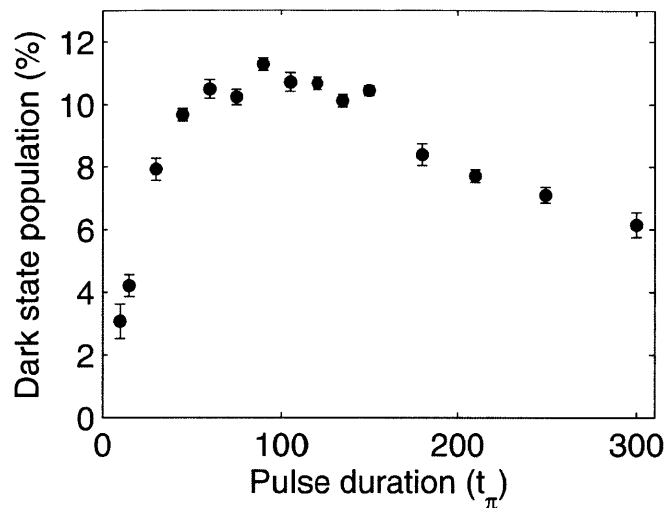


Figure 6-5: Dark state population induced by resonant, Doppler insensitive Raman pulses ($\Delta = -1.25$ GHz).

appeared to saturate at $60 - 80 t_\pi$, and thereafter, losses due to spontaneous emission and weak coupling out of the dark state dominated. A linear fit over the short pulse duration data estimates that a π pulse traps 1.5% of the population for $\Delta = -1.65$ GHz (laser detunings are referenced to the $F = 4 \rightarrow F' = 2$ frequency). Direct measurements of CPT for Raman pulses with pulse areas under 10π were not possible because of inadequate dephasing of the initial ensemble. Nevertheless, as Fig. 6-6 shows, the phase of the observed coherences at all longer pulse durations remained at the expected phase of $\Delta\phi = -\pi/2$, an important necessary condition for identification of the coherence as a CPT effect. Figure 6-7 shows trapped population versus pulse duration curves for several laser detunings, from -1.25 GHz to -3 GHz. Maximum trapping was observed at $\Delta \approx -1.5$ GHz. The theory in Section 6.2 predicts a constant asymptotic dark state polarization, independent of laser detuning, but a trapping rate scaling as $\sim 1/\Delta$. Figure 6-7 shows that induced polarizations over a $2\times$ variation in laser detuning are similar, reflecting only weak dependence on laser detuning (one expects the slope of these curves at short pulse durations to exhibit the $\sim 1/\Delta$ scaling). This discrepancy with the theory is likely a result of more complex dynamics uncaptured by the three-level model. Another possible contribution is the presence of other Raman-resonant frequency pairs produced by phase modulation of the Raman laser. While the two dominant frequencies (in terms of single-photon detuning) become farther detuned, other pairs shift closer to single-photon resonance, and would also induce CPT.

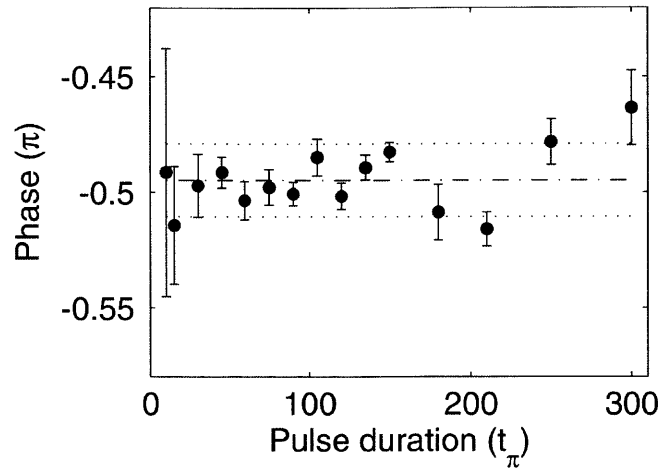


Figure 6-6: Phase of dark state coherences induced by Doppler insensitive Raman pulses. A phase of $-\pi/2$ corresponds to induced polarization parallel to the effective drive field Ω .

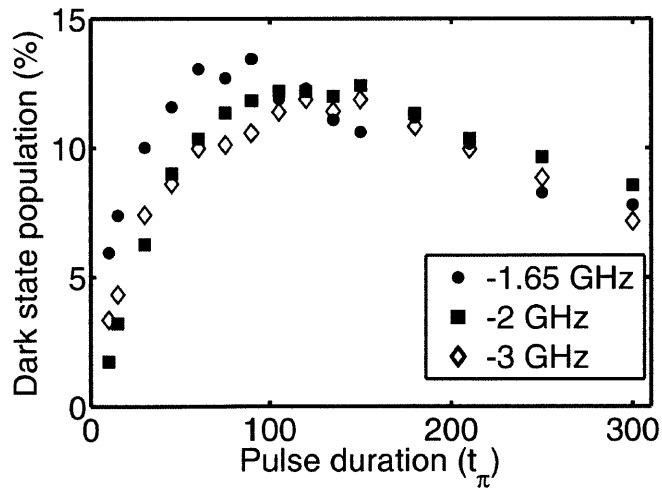


Figure 6-7: Induced dark state population obtained with several Raman laser detunings. The magnitude of trapped population is weakly dependent on Raman laser detuning, although smaller detuning does appear to lead to a larger trapping rate.

Lastly, measurements were made of population differences induced by off-resonant Raman pulses. For the condition of non-zero Raman detuning, the effective drive field vector $\mathbf{\Omega}$ is out of the plane, so that a dark state with a nonzero population difference results. In the experiment, the initial sample of atoms was prepared in the $|F = 3, m_F = 0\rangle$ level ($\mathbf{P} = -\hat{z}$) and subsequently, a coherent superposition of the $|F = 3, m_F = 0\rangle$ and $|F = 4, m_F = 0\rangle$ levels was created with a Raman $\pi/2$ pulse. After a brief dwell time, an off-resonant Raman pulse dephased this initial coherence and induced a dark state polarization. Since the laser frequency difference changed between the first and second pulse, the laser difference phase for the second pulse was shifted such that the initial polarization was dispersed with an average transition probability of 50% (i.e., $\langle P_z \rangle = 0$). This phase offset was experimentally determined for each chosen Raman detuning using a $\pi/2 - \pi^*$ interferometer (π^* denotes an off-resonant π pulse) with the same dwell time between pulses. Fig. 6-8 illustrates the concept of this diagnostic. Finally, the P_z component of the trapped population was measured by reading out the transition probability and comparing to 50%. In order to suppress systematic errors resulting from drifting Raman beam power, the $P_z = 0$ level in the state detection was calibrated at every other measurement by applying a single resonant 15.5π pulse and measuring population transfer. It was also found that the precision of the $\pi/2$ pulse length calibration was required to be within 1% in order to produce a symmetric profile. This calibration was confirmed independently by comparing the phase shifts measured with the $\pi/2 - \pi^*$ interferometer at Raman detunings of equal magnitude but opposite sign. When the observed phase shifts were equal but opposite in sign, the pulse length was correct.

Fig. 6-9 shows the induced population difference P_z for $\Delta = -1.25$ GHz and a second pulse duration of $40t_\pi$. This pulse duration was chosen because the induced polarization grows linearly in this range, as shown above in Fig. 6-5. In agreement with the theory, the profile is antisymmetric about the Raman resonance and the overall sign of P_z is opposite that of the Raman detuning. Extrema were observed at $\delta = \pm\Omega_{\text{eff}}$, as predicted. For $\delta < |\Omega_{\text{eff}}|$, the observed P_z dependence resembles the z -projection of a polarization aligned with the effective drive field and with a magnitude equal to the polarization induced by a resonant Raman pulse (0.19, or population $\approx 9.5\%$, for a 40π pulse). Figure 6-9 also includes a theoretical prediction from a simple extension of the theory presented above, which permits spontaneous emission to uncoupled ($m_F \neq 0$) ground states. An atom that decays to one

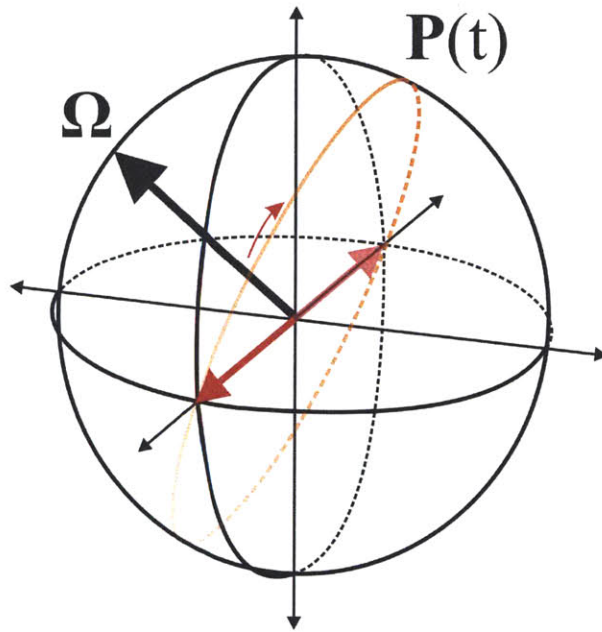


Figure 6-8: Bloch sphere diagram of a $\pi/2 - \pi^*$ sequence, used to calibrate the measurement of CPT effects induced by off-resonant Raman pulses. After the initial polarization is placed in the plane, a π pulse at the generalized (detuning-dependent) Rabi frequency rotates the polarization back into the plane when the drive field is 90° out of phase. At this particular phase, the drive field disperses the initial polarization in a disc so that the average population difference is zero (as opposed to the case of a cone centered about the drive field vector). However, dark state population accumulates along the drive field vector Ω , and leads to a population difference (see data in Fig. 6-9).

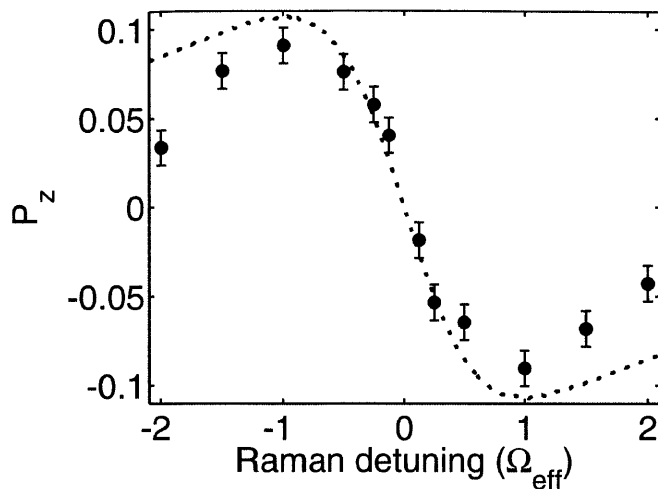


Figure 6-9: Measurements of P_z of dark state population induced by off-resonant Raman pulses. The dashed curve represents a theoretical prediction based on an extension of the three state theory permitting spontaneous decay out of the two coupled ground states.

of these uncoupled states no longer experiences the effects of CPT, and does not contribute to the observed population difference. The model assumed a probability of spontaneous emission to uncoupled levels according to the dipole matrix elements for cesium. At larger Raman detunings, observed CPT effects are smaller than predicted by the three level theory; this discrepancy is expected since the theory does not account for the existence of multiple intermediate states, which would affect the rate of population trapping. Nevertheless, these measurements validate the prediction that CPT induces a polarization along the effective drive field vector.

6.3.2 Doppler Sensitive Raman pulses

The detection of CPT effects with Doppler sensitive Raman pulses required a slightly different method than that used with Doppler insensitive pulses. Fig. 6-10 provides a Bloch sphere picture of the experiment. Initially, atoms were prepared in the $|F = 3, m_F = 0\rangle$ state, and subsequently a equal superposition was created by a microwave $\pi/2$ pulse. Since the wavelength of the microwave transition (≈ 3.3 cm) is large compared to the cloud size (≈ 1 mm), all of the atoms experience a similar phase. After a brief dwell time, a long, resonant Doppler sensitive Raman pulse dispersed the ensemble and induced CPT. The atoms experience a distribution of Raman phases because of their initial spread in position

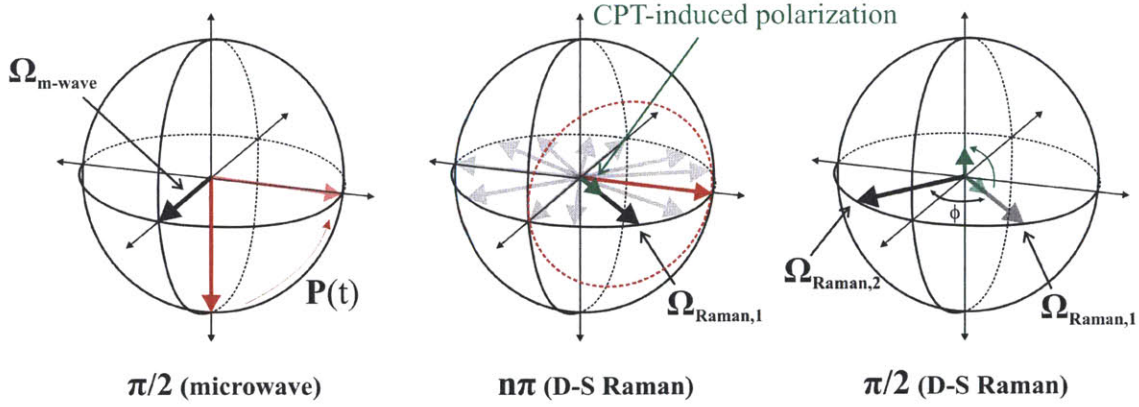


Figure 6-10: Bloch sphere diagram of the pulse sequence for measuring CPT effects induced by Doppler sensitive Raman pulses. First, a microwave pulse creates an equal superposition with approximately the same phase for all atoms (the microwave wavelength is $>10\times$ the cloud size). A Doppler sensitive Raman pulse then disperses the initial ensemble because an effectively random phase is seen by each atom (the effective wavelength is only 426 nm). A dark state coherence is formed at the Raman laser phase, and is read out by a $\pi/2$ pulse.

over many effective wavelengths ($2\pi/|\mathbf{k}_{\text{eff}}| \approx 426$ nm), thoroughly scrambling the phase of the initial coherence with respect to the position-dependent Raman effective drive field Ω . After a very short dwell time (typically 1-2 μs), a Raman $\pi/2$ pulse at variable phase projected the induced polarization onto the z -axis.

Fig. 6-11 shows the profile of dark state population versus pulse duration, for a laser detuning of $\Delta = -1.25$ GHz and a Rabi frequency of 80 kHz. These data resemble the measurements of dark state population for varying Raman pulse duration in the analogous Doppler insensitive experiment (compare with Fig. 6-5). Again, the effect appears to saturate between $60 - 80t_\pi$ and decays at longer pulse durations. While the magnitude of the dark state population appears smaller than what was measured with Doppler insensitive beams, these measurements underestimate the trapped population because the interferometer is only partially overlapping, and consequently exhibits poorer phase contrast (which is the measure for the trapped population). To compensate for this inefficiency, the contrast of a Doppler sensitive $\pi/2 - \pi/2$ interferometer was measured for a range of dwell times. Figure 6-12 shows that less than 30% contrast was obtainable for a ≈ 7 μK cloud. With velocity selection, however, interrogating atoms with a temperature of ≈ 400 nK produced greater than 55% contrast for the same dwell times (shown by the upper curve in Fig. 6-12). In both cases, adjusting the measured dark state CPT population by the two pulse interferometer

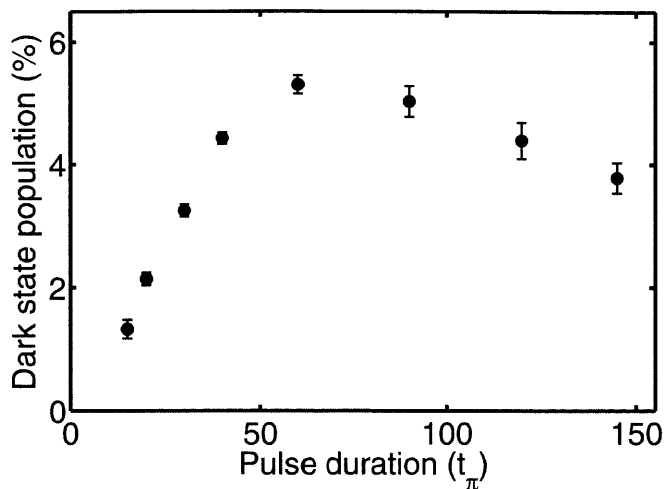


Figure 6-11: Dark state population induced by Doppler sensitive Raman pulses. These values have not been adjusted to compensate for the reduced contrast of the interferometer.

visibility leads to an estimated maximum induced dark state coherence of magnitude 0.18 (9% population), somewhat smaller than the maximum value observed with Doppler insensitive Raman pulses. One also expects to detect less population trapping by Doppler sensitive Raman pulses because of the Doppler broadening of the resonance, which leads to a spread in the effective drive fields across the ensemble. Based on the slope at short pulse durations, one can infer an induced dark state coherence of magnitude 0.0074 (population of 0.37%) for a π pulse. These numerical results are, to some degree, implementation-specific, and that systems with different Raman beam parameters (e.g., phase front quality) or Raman frequency generation methods (e.g., a phase-locked pair of lasers) could observe different dark state populations.

6.3.3 Impact of CPT on a $\pi/2 - \pi - \pi/2$ Interferometer, Summary

Consider a simple estimate of the impact of an induced dark state coherence on a Doppler sensitive $\pi/2 - \pi - \pi/2$ interferometer, which is the most common sequence for acceleration and rotation rate measurements (see Fig. 6-13 for an illustration of this argument). The first Raman pulse induces a small coherence 90° out of phase with the primary coherence created by tipping the initial polarization into the $\mathbf{x} - \mathbf{y}$ plane. The induced coherence is orthogonal to the primary coherence, and effectively shifts the net phase by the ratio of the induced coherence magnitude to that of the primary coherence. The second pulse

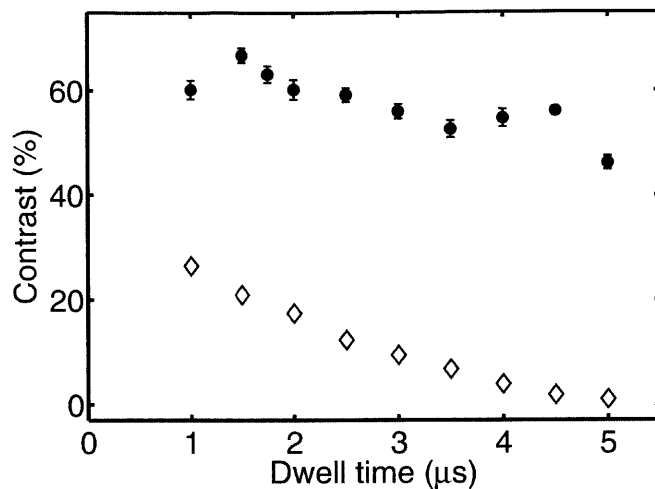


Figure 6-12: Contrast achieved with a Doppler sensitive, non-overlapping $\pi/2 - \pi/2$ interferometer with (circles) and without (diamonds) velocity selection. The contrast of this non-overlapping interferometer indicates the efficiency with which it is possible to measure dark state population induced by Doppler sensitive Raman pulses. Velocity selection clearly suppresses decoherence due to cloud diffusion.

again transfers population to a dark state; however, each atom in the ensemble experiences a different effective drive field phase because of the thermal velocity distribution. The ensemble average of the phase shift induced by the second Raman pulse is then zero. The third pulse also induces a coherence, but for near-resonant Raman pulses it does not affect the final state population since the induced polarization is in the $\mathbf{x} - \mathbf{y}$ plane. Thus, one expects a net phase shift due to population trapped by the first Raman pulse only. Since the experimental results have shown that the magnitude of CPT-induced polarization is roughly independent of Rabi frequency, they can provide an estimate of the phase shift introduced by CPT in an interferometer with cesium. The results in Section 6.3.2 exhibited coherences of magnitude 0.0074 per Doppler sensitive π pulse. Correspondingly, one can infer that a $\pi/2 - \pi - \pi/2$ interferometer should register a phase shift of $\Delta\phi \approx 0.0074/2 \approx 3.7$ mrad phase shift. In a previous high precision cesium gravimeter [25, 26], this phase shift corresponded to a gravity offset of ≈ 1 ng. An error of this magnitude is four times smaller than the claimed experimental error, so a CPT-induced error of the estimated size would not significantly affect their results. In the gravity measurement of this thesis, however, a much smaller inertial phase shift was measured, due to the use of shorter interrogation times. Nevertheless, a systematic phase shift of this magnitude is still not a dominant source of error (in Section

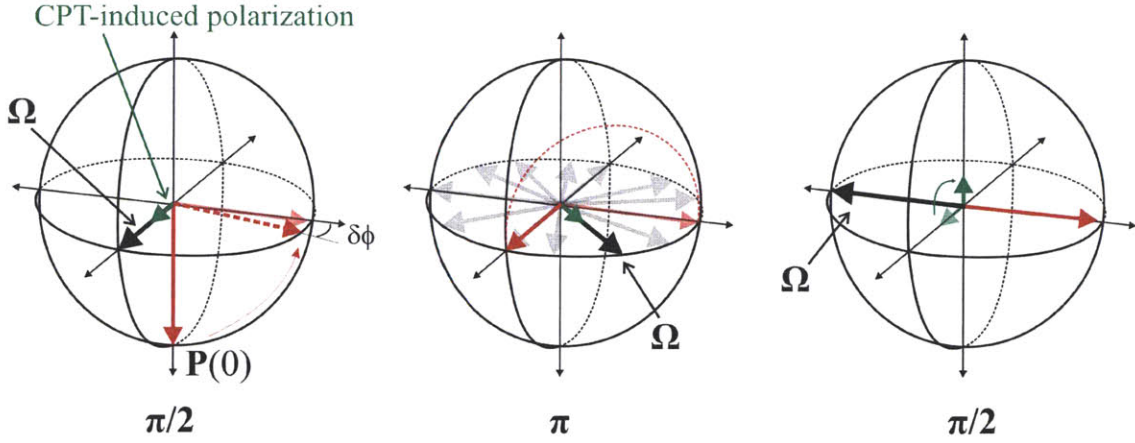


Figure 6-13: Bloch sphere diagram of systematic phase shift, $\delta\phi$, induced by CPT in a $\pi/2 - \pi - \pi/2$ interferometer. The first pulse induces a dark state polarization along the drive field vector, shifting the phase of the initial coherence. The second pulse also creates a dark state polarization, but the average contribution is zero over the ensemble because of the velocity-dependent phase. At the third pulse, the dark state polarization induced by the first pulse can be rotated to form a population difference and therefore register a phase shift. Dark state population trapped by the third pulse (on resonance) does not lead to a population difference.

4.4, AC Stark shifts are cited as the largest source of systematic error). Finally, since the effect is only weakly dependent on Rabi frequency and laser detuning, a Raman beam with well-controlled parameters should produce a stable phase shift, so that the principal effect would likely pertain more to accuracy than stability. For a frequency-stabilized Raman laser, the effect should be stable at the $\sim \mu\text{rad}$ level.

While it would be preferable to directly measure an interferometer phase shift induced by CPT, the current apparatus lacks sufficient stability to resolve this phase offset. In principle, the phase shift could be measured by alternately running $(\pm\pi/2) - \pi - \pi/2$ interferometers and comparing their phases. A deviation of the relative phase from π would be ascribed to a CPT-induced shift.

It is worth noting that a CPT-induced interferometer phase shift would be independent of the Raman beam wavevector \mathbf{k}_{eff} . Therefore, the method of propagation direction reversal, in which the sign of \mathbf{k}_{eff} is alternated from shot to shot, should suppress the resulting bias with averaged measurements because the \mathbf{k}_{eff} -proportional contribution to the signal reverses sign while the CPT interferometer phase shift does not. This method has been used in previous work to suppress phase shifts from AC Stark shifts [34, 102].

The impact of CPT has been discussed in the context of an inertially sensitive $\pi/2 - \pi - \pi/2$ interferometer, but other Raman interferometers should also experience phase shifts arising from this effect. A simple example is a Doppler insensitive Raman $\pi/2 - \pi/2$ clock measurement, in which the first pulse would induce a dark state coherence and offset the phase read out by the second pulse. Moreover, the phase shift due to a detuning in this interferometer is independent of \mathbf{k}_{eff} , thereby precluding the use of propagation direction reversal to suppress the bias.

THIS PAGE INTENTIONALLY LEFT BLANK

Chapter 7

Conclusion

An atom interferometer based on stimulated Raman transitions has been developed for gravimetry using a compact vacuum cell. This work makes progress toward the realization of rapid interrogation atom interferometric inertial sensors for practical inertial navigation applications. High contrast, inertially-sensitive interferometry was demonstrated for interrogation times of $2T < 15$ ms, achieving an inferred acceleration sensitivity of $2 \mu g/\sqrt{\text{Hz}}$ at $2T = 10$ ms (from measured phase SNR, scale factor, and repetition rate). This interferometer was used to measure gravity, and was primarily limited in precision by high frequency vibrations in the laboratory. These interrogation times reflect those expected to be used in practical inertial sensors in dynamic applications.

An improved method for large momentum transfer by sequential Raman pulses was demonstrated using composite Raman pulses. A composite pulse sequence, $\pi/2_{0^\circ} - \pi_{180^\circ} - 3\pi/2_{0^\circ}$, was identified for efficient, broadband population inversion; with this composite pulse, a large area atom interferometer with a relative momentum splitting of up to $9\hbar k_{\text{eff}} \approx 18\hbar k$ ($\approx 9\times$ increase in signal) was modeled and demonstrated. This is the largest momentum transfer reported for an inertially-sensitive atom interferometer based on Raman transitions. Intrinsic sensitivity was enhanced by up to a factor of two, but was limited by defects in the implementation of the composite pulses and the Raman beam phase front quality.

Finally, coherent population trapping (CPT) was identified as a significant systematic effect in Raman pulse atom interferometers, and which was not considered in previous work.

CPT effects were modeled in a three-level atom to provide qualitative predictions for experiments. Experimental measurements resolved dark state coherences and population differences induced by transient CPT effects in both Doppler insensitive and Doppler sensitive Raman pulses. These experiments detected transient CPT effects in cold atoms using atom interferometry, whereas previous work focused on steady-state effects. For inertially-sensitive atom interferometers, milliradian-scale systematic phase shifts due to CPT effects could be suppressed in operation by averaging measurements with opposite Raman beam propagation directions ($\pm \mathbf{k}_{\text{eff}}$).

7.1 Future Steps

As previously mentioned, the measured gravimeter sensitivity of the apparatus is currently limited by vibrations in the laboratory, primarily from floor vibrations and acoustic noise from environmental control systems. Improved stabilization of the Raman beam retroreflector should suppress the effect of these vibrations, but better assessment of intrinsic performance characteristics will likely require a more stable environment (e.g., a pier). Another solution would be to install a second MOT and interrogate both ensembles simultaneously, providing a differential acceleration measurement in which the vibrations are common mode. Once vibrational noise is suppressed, the system will be limited by detection SNR. The current readout SNR is far below the shot noise limit for even the velocity-selected ensembles of 10^6 atoms (SNR limited to 1000). An improved readout that simultaneously imaged both ground state populations would reduce the impact of frequency and amplitude fluctuations of the probe beam. Increasing the experimental repetition rate will also improve the acceleration sensitivity, bandwidth, and dynamic range of the system. This entails increasing the loading rate of the MOT, perhaps by installing a 2D MOT in a differentially-pumped, higher pressure vapor cell. This may not be necessary, however, as a recent demonstration of a similar cold atom gravimeter with repetition rates of over 300 Hz solely relied on recapturing atoms from the previous measurement to reduce the loading time [103].

Improvements can also be made to the implementation of large area atom interferometry with composite Raman pulses. As noted above, the maximum achievable momentum splitting was limited by Raman beam phase front quality and defects in the composite pulses.

These issues could be mitigated with higher quality optics, as well as improvements to the microwave frequency electronics. Together with realistic improvements to the repetition rate, readout SNR, and large area interferometers, the sensitivity of the system could be improved by over an order of magnitude ($<1 \mu g/\sqrt{\text{Hz}}$).

It may also be technologically advantageous to use rubidium rather than cesium, since the 780 nm cooling transition can be generated by frequency-doubling 1560 nm, availing robust, fiber-based telecom electro-optic and laser components [104]. Finally, significant work remains in developing vacuum cells and low or zero power vacuum pumps that can preserve ultra-high vacuum for long lifetimes (many applications demand lifetimes of multiple years). The principal challenge here is minimization of helium diffusion in the cell, which can only be pumped efficiently by ion pumps.

Significant engineering remains in developing high precision atom interferometric inertial sensors that meet the bandwidth, dynamic range, and size, weight, and power requirements of inertial navigation systems. One major thrust for future work involves the integration of multiple atomic sensors to provide a full inertial base (three accelerometers and three gyroscopes). In addition to the challenge of interrogating multiple atom clouds simultaneously, engineering must carefully address how inertial information is to be extracted from the set of interferometer phases, while optimizing the noise statistics. Together with maturation of cold atom sensor technology, development of complete-atom interferometric inertial measurements units may yet revolutionize a broad range of navigation applications.

THIS PAGE INTENTIONALLY LEFT BLANK

Appendix A

Cesium D2 Transition Data

Quantity	Symbol	Value
Atomic number	Z	55
Atomic mass	m	$2.206\,946\,57(11) \times 10^{-25}$ kg
Nuclear spin	I	7/2
Transition frequency	ω_0	$2\pi \times 351.725\,718\,50(11)$ THz
Wavelength (vacuum)	λ	852.347 275 82(27) nm
Lifetime	τ	30.405(77) ns
Natural linewidth	Γ	$2\pi \times 5.234(13)$ MHz
Oscillator strength	f	0.7164(25)
Saturation intensity	I_{sat}	1.1049(20) mW/cm ²
Doppler temperature	T_D	125.61 μ K
Recoil temperature	T_r	198.34 nK
Recoil velocity	v_r	3.5225 mm/s
Two-photon recoil Doppler shift	ω_r	$2\pi \times 8.2653$ kHz
Hyperfine splitting frequency	ω_{HF}	9.192 531 770 GHz (exact)

Table A.1: Relevant constants of ^{133}Cs and the D2 ($6^2S_{1/2} \rightarrow 6^2P_{3/2}$) transition [105].

THIS PAGE INTENTIONALLY LEFT BLANK

Appendix B

Modeling of Large Area Atom Interferometry

In Chapter 5, composite Raman pulses and large area atom interferometers were studied with an analytical model. This chapter summarizes the method for calculating probability amplitudes in multi-pulse sequences. The model is capable of:

- Calculating the phase and contrast for Doppler insensitive and Doppler sensitive interferometers
- Analyzing arbitrary pulse sequences, including sequences with alternating \mathbf{k}_{eff} and composite Raman pulses
- Accounting for finite pulse duration in interferometer phase
- Estimating errors due to power or detuning offsets

The central element of the model is an operator that propagates probability amplitudes through a sequence of Raman pulses, including phases accrued in the periods between pulses. Analysis in [60] derives output probability amplitudes for a Raman pulse, and presents a diagrammatic technique for analyzing interferometer outputs. A Raman pulse, denoted by an operator R_j for the j^{th} pulse, acts on an atom initially in either of the two ground state

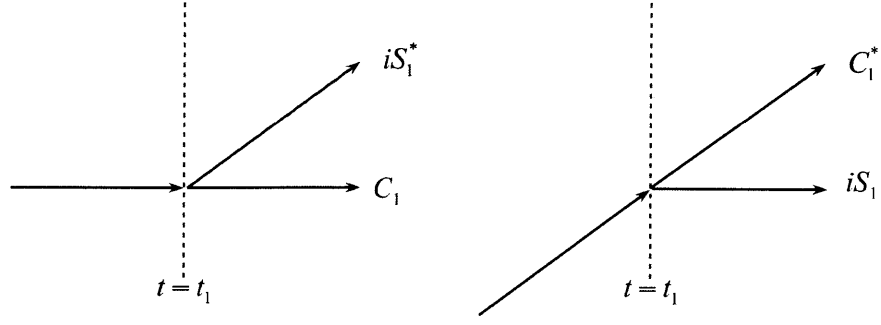


Figure B-1: Diagrammatic representation of the Raman pulse operator acting an initial state purely in the lower ground state (left) and purely in the upper ground state (right).

levels $|g\rangle$ and $|e\rangle$ as (represented graphically in Fig. B-1):

$$R_j|g\rangle = C_j|g\rangle - iS_j^*|e\rangle \quad (\text{B.1})$$

$$R_j|e\rangle = C_j^*|e\rangle - iS_j|g\rangle \quad (\text{B.2})$$

The amplitude factors C_j and S_j are defined as

$$C_j \equiv \cos\left(\frac{\tau_j\Omega_j}{2}\right) + i\cos(\theta_j)\sin\left(\frac{\tau_j\Omega_j}{2}\right) \quad (\text{B.3})$$

$$S_j \equiv e^{i\phi_j}\sin(\theta_j)\sin\left(\frac{\tau_j\Omega_j}{2}\right) \quad (\text{B.4})$$

where Ω_j is the generalized Rabi frequency for pulse j , τ_j is the pulse duration, ϕ_j is the effective laser phase at $t = 0$, and θ is the state space mixing angle:

$$\cos\theta = \frac{\delta_{AC} - \delta}{\Omega}, \quad \sin\theta = \frac{|\Omega_{\text{eff}}|}{\Omega} \quad (\text{B.5})$$

Like the theory presented in Chapter 2, this model neglects spontaneous emission and cross-coupling of the fields to the two optical transitions. The above expressions are arrived at after making the rotating wave approximation and adiabatically eliminating the excited state.

After a Raman pulse, the amplitudes for each state accrue a phase during the dwell period between pulses j and $j + 1$, $\exp(\pm\frac{i}{2}\Phi_{j \rightarrow j+1})$, with the positive phase corresponding to the upper ground state and the negative phase corresponding to the lower state. Figure B-2 diagrams the amplitudes after a second pulse, including the phase introduced by the

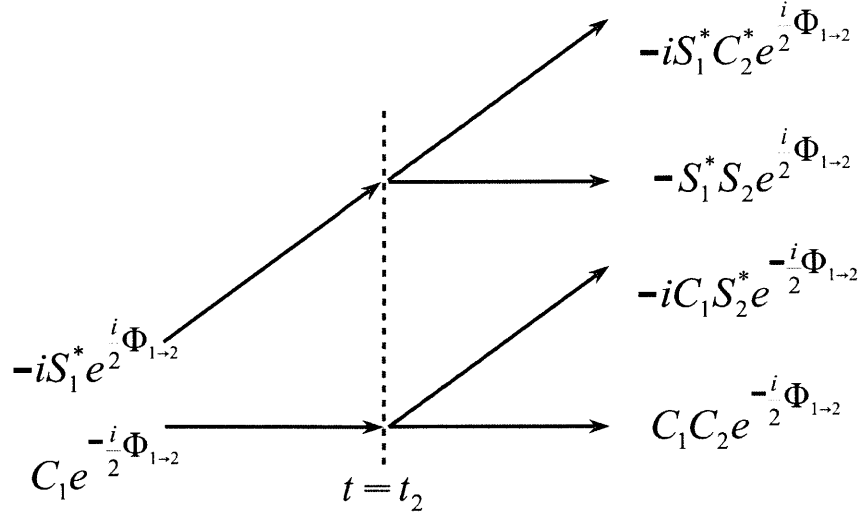


Figure B-2: Diagrammatic representation of probability amplitudes for a two-pulse sequence, assuming the initial state is the lower ground state, $|g\rangle$.

dwell time. The total integrated phase $\Phi_{j \rightarrow j+1}$ is defined as

$$\Phi_{j \rightarrow j+1} \equiv \int_0^{t_j + \tau_j} dt' [\delta_{j+1}(t') - \delta_j(t')] + \int_{t_j + \tau_j}^{t_{j+1}} dt' \delta_{j+1}(t') \quad (\text{B.6})$$

where the Raman laser detuning for pulse j , $\delta_j(t)$, is defined as:

$$\delta_j(t) = [\omega_1(t) - \omega_2(t)]_j - \left[\omega_{HF} + \frac{\hbar k_{\text{eff},j}^2}{2m} + \mathbf{k}_{\text{eff},j} \cdot \hat{e}_z \dot{z}(t) \right] \quad (\text{B.7})$$

This procedure is repeated for an n pulse sequence, creating a vector of 2^n amplitudes. At the conclusion of the sequence, the amplitudes that contribute to interference must be identified. In Doppler insensitive interferometry, this generally includes all amplitudes. For instance, at the end of the two-pulse sequence shown in Fig. B-2, the ground state amplitudes are

$$\Psi_e(t_2 + \tau_2)|_{2\text{-pulse}} = -iC_1 S_2^* \exp\left(-\frac{i}{2} \Phi_{1 \rightarrow 2}\right) - iS_1^* C_2^* \exp\left(\frac{i}{2} \Phi_{1 \rightarrow 2}\right) \quad (\text{B.8})$$

$$\Psi_g(t_2 + \tau_2)|_{2\text{-pulse}} = C_1 C_2 \exp\left(-\frac{i}{2} \Phi_{1 \rightarrow 2}\right) - S_1^* S_2 \exp\left(\frac{i}{2} \Phi_{1 \rightarrow 2}\right), \quad (\text{B.9})$$

from which the probability densities are calculated.

In the case of a Doppler sensitive interferometer, the analysis is more involved. The vector of amplitudes after a $\pi/2 - \pi - \pi/2$ sequence has length eight (shown in Fig. B-3).

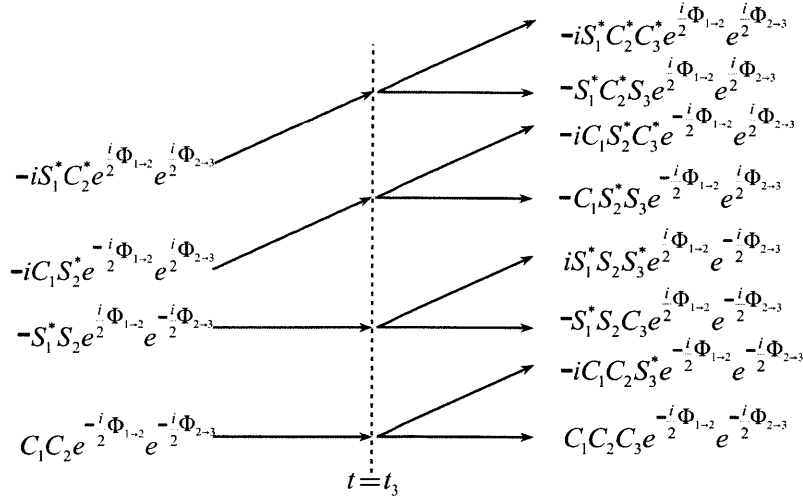


Figure B-3: Diagrammatic representation of probability amplitudes for a three-pulse sequence, assuming the initial state is the lower ground state, $|g\rangle$.

Summing all the amplitude terms for the lower ground state produces exponential terms $\exp\left[\frac{i}{2}(\Phi_{2\rightarrow3} - \Phi_{1\rightarrow2})\right]$ and $\exp\left[\frac{i}{2}(\Phi_{2\rightarrow3} + \Phi_{1\rightarrow2})\right]$. The latter term can be shown to have initial velocity-dependent terms, such as $\mathbf{k}_{\text{eff}} \cdot \hat{e}_z \dot{z}(t=0)T$. The RMS phase for an interferometer with interrogation time $T = 1$ ms and $0.5 \mu\text{K}$ cloud is $\mathbf{k}_{\text{eff}} \cdot \hat{e}_z \sqrt{\dot{z}(t=0)^2}T \approx 10^2$ rad. Therefore, when these amplitudes are averaged over the ensemble, they are heavily suppressed and do not result in visible interference. Probability amplitudes with the difference of the integrated phases, however, give the expected phases derived in Chapter 2, as well as phase terms resulting from finite duration of the light pulses.

For large area interferometer analysis, probability amplitudes were calculated in Mathematica, using this diagrammatic method. Both constant and swept laser frequency difference cases were analyzed for interferometer phase, acceleration scale factor, and contrast. Composite Raman pulses were analyzed as multi-pulse sequences without dwell time periods, using the same approach. All composite Raman pulse detuning profiles and large area interferometer theoretical curves reported in Chapter 5 were produced with this model.

Bibliography

- [1] Christopher Jekeli. Precision free-inertial navigation with gravity compensation by an onboard gradiometer. *Jour. of Guidance, Control, and Dynamics*, 29:704–713, 2006.
- [2] Neil Barbour. Private communication, 2011.
- [3] A. Peters, K.Y. Chung, and S. Chu. High-precision gravity measurements using atom interferometry. *Metrologia*, 38:25–61, 2001.
- [4] T.L. Gustavson, A. Landragin, and M.A. Kasevich. Rotation sensing with a dual atom interferometer Sagnac gyroscope. *Class. Quant. Grav.*, 17:2385, 2000.
- [5] D. S. Durfee, Y. K. Shaham, and M. A. Kasevich. Long-term stability of an area-reversible atom-interferometer Sagnac gyroscope. *Phys. Rev. Lett.*, 97(24):240801, Dec 2006.
- [6] J.B. Fixler, G.T. Foster, J.M. McGuirk, and M.A. Kasevich. Atom interferometer measurement of the Newtonian constant of gravity. *Science*, 315(5808):74–77, 2007.
- [7] A.D. Cronin, J. Schmiedmayer, and D.E. Pritchard. Optics and interferometry with atoms and molecules. *Reviews of Modern Physics*, 81:1051–1129, 2009.
- [8] I. Rabi, J. Zacharias, S. Millman, and P. Kusch. A new method for measuring nuclear magnetic moments. *Phys. Rev.*, 53:318, 1938.
- [9] N. Ramsey. A new molecular beam resonance method. *Phys. Rev.*, 76:996, 1949.
- [10] R. Colella, A.W. Overhauser, and S.A. Werner. Observation of gravitationally induced quantum interference. *Phys. Rev. Lett.*, 34:1472–1474, 1975.

- [11] O. Carnal and J. Mlynek. Young's double-slit experiment with atoms: A simple atom interferometer. *Phys. Rev. Lett.*, 66:2689–2692, 1991.
- [12] D.W. Keith, C.R. Ekstrom, Q.A. Turchette, and D. Pritchard. An interferometer for atoms. *Phys. Rev. Lett.*, 66:2693, 1991.
- [13] M.A. Kasevich and S. Chu. Atomic interferometry using stimulated Raman transitions. *Phys. Rev. Lett.*, 67:181–4, 1991.
- [14] F. Riehle, Th. Kisters, A. Witte, J. Helmcke, and Ch.J. Bordé. Optical Ramsey spectroscopy in a rotating frame: Sagnac effect in a matter-wave interferometer. *Phys. Rev. Lett.*, 67:177–180, 1991.
- [15] P.R. Berman, editor. *Atom Interferometry*. Academic Press, New York, 1997.
- [16] A. Ashkin. Acceleration and trapping of particles by radiation pressure. *Phys. Rev. Lett.*, 24:156–159, Jan 1970.
- [17] A. Ashkin. Atomic-beam deflection by resonance-radiation pressure. *Phys. Rev. Lett.*, 25:1321–1324, Nov 1970.
- [18] A. Ashkin. Trapping of atoms by resonance radiation pressure. *Phys. Rev. Lett.*, 40:729–732, Mar 1978.
- [19] S. Chu, L. Hollberg, J.E. Bjorkholm, A. Ashkin, and A. Cable. Three-dimensional viscous confinement and cooling of atoms by resonance radiation pressure. *Phys. Rev. Lett.*, 55:48–51, 1985.
- [20] E.L. Raab, M. Prentiss, A. Cable, S. Chu, and D.E. Pritchard. Trapping of neutral sodium atoms with radiation pressure. *Phys. Rev. Lett.*, 59:2631–2634, 1987.
- [21] H.J. Metcalf and P. van der Straten. *Laser Cooling and Trapping*. Springer, New York, 2002.
- [22] J. Dalibard and C. Cohen-Tannoudji. Laser cooling below the Doppler limit by polarization gradients: simple theoretical models. *J. Opt. Soc. Am. B*, 6(11):2023–2045, Nov 1989.

- [23] M.A. Kasevich, E. Riis, S. Chu, and R.G. DeVoe. rf spectroscopy in an atomic fountain. *Phys. Rev. Lett.*, 63:612, 1989.
- [24] A. Peters. *High Precision Gravity Measurements Using Atom Interferometry*. PhD thesis, Stanford University, 1998.
- [25] A. Peters, K.Y. Chung, and S. Chu. Measurement of gravitational acceleration by dropping atoms. *Nature*, 400:849–852, Oct 1999.
- [26] H. Müller, A. Peters, and S. Chu. A precision measurement of the gravitational redshift by the interference of matter waves. *Nature*, 463:926–929, 2010.
- [27] T. M. Niebauer, G. S. Sasagawa, J. E. Faller, R. Hilt, and F. Klopping. A new generation of absolute gravimeters. *Metrologia*, 32(3):159, 1995.
- [28] S. Dimopoulos, P.W. Graham, J.M. Hogan, and M.A. Kasevich. Testing general relativity with atom interferometry. *Phys. Rev. Lett.*, 98(11):111102, Mar 2007.
- [29] J. M. McGuirk, G. T. Foster, J. B. Fixler, M. J. Snadden, and M. A. Kasevich. Sensitive absolute-gravity gradiometry using atom interferometry. *Phys. Rev. A*, 65(3):033608, Feb 2002.
- [30] Fundamental Physical Constants from NIST, 2010. <http://physics.nist.gov/cuu/Constants/index.html>.
- [31] G. Biedermann. *Gravity Tests, Differential Accelerometry and Interleaved Clocks with Cold Atom Interferometers*. PhD thesis, Stanford University, 2007.
- [32] X. Wu. *Gravity Gradient Survey with a Mobile Atom Interferometer*. PhD thesis, Stanford University, 2009.
- [33] T.L. Gustavson, P. Bouyer, and M.A. Kasevich. Precision rotation measurements with an atom interferometer gyroscope. *Phys. Rev. Lett.*, 78:2046, 1997.
- [34] K. Takase. *Precision Rotation Rate Measurements with a Mobile Atom Interferometer*. PhD thesis, Stanford University, 2008.

- [35] J. K. Stockton, K. Takase, and M. A. Kasevich. Absolute geodetic rotation measurement using atom interferometry. *Phys. Rev. Lett.*, 107:133001, Sep 2011.
- [36] M.A. Kasevich. Mobile Atomic Gravity Gradiometer Prototype Instrument (MAG-GPI): Final Report. Technical Report AFRL-VS-TR-2002-1645, Air Force Research Laboratory, 2002.
- [37] Q. Bodart, S. Merlet, N. Malossi, F. Pereira Dos Santos, P. Bouyer, and A. Landragin. A cold atom pyramidal gravimeter with a single laser beam. *Appl. Phys. Lett.*, 96(13):134101, 2010.
- [38] G. Stern, B. Battelier, R. Geiger, G. Varoquaux, A. Villing, F. Moron, O. Carraz, N. Zahzam, Y. Bidel, W. Chaibi, F. Pereira Dos Santos, A. Bresson, A. Landragin, and P. Bouyer. Light-pulse atom interferometry in microgravity. *Eur. Phys. J. D*, 53:353–357, 2009.
- [39] R. Geiger, V. Ménotet, G. Stern, N. Zahzam, P. Cheinet, B. Battelier, A. Villing, F. Moron, M. Lours, Y. Bidel, A. Bresson, A. Landragin, and P. Bouyer. Detecting inertial effects with airborne matter-wave interferometry. *Nature Comm.*, 2:474, 2011.
- [40] F. Lienhart, S. Boussem, O. Carraz, N. Zahzam, Y. Bidel, and A. Bresson. Compact and robust laser system for rubidium laser cooling based on the frequency doubling of a fiber bench at 1560 nm. *Appl. Phys. B*, 89:177–180, 2007.
- [41] T. Müller, M. Gilowski, P. Berg, Ch. Schubert, T. Wendrich, W. Ertmer, and E.M. Rasel. A compact dual atom interferometer gyroscope based on laser-cooled rubidium. *Eur. Phys. J. D*, 53:273–281, 2009.
- [42] T. Müller, T. Wendrich, M. Gilowski, C. Jentsch, E.M. Rasel, and W. Ertmer. Versatile compact atomic source for high-resolution dual atom interferometry. *Phys. Rev. A*, 76:063611, 2007.
- [43] B. Canuel, F. Leduc, D. Holleville, A. Gauguier, J. Fils, A. Viridis, A. Clairon, N. Dimarcq, Ch.J. Bordé, A. Landragin, and P. Bouyer. Six-axis inertial sensor using cold atom interferometry. *Phys. Rev. Lett.*, 97:010402, 2006.

- [44] M.A. Kasevich and B. Dubetsky. *Kinematic sensors employing atom interferometer phases*. U. S. Patent Office, 2008. Patent number 7,317,184.
- [45] J. M. McGuirk, M. J. Snadden, and M. A. Kasevich. Large area light-pulse atom interferometry. *Phys. Rev. Lett.*, 85(21):4498–4501, Nov 2000.
- [46] H. Müller, S.-w. Chiow, Q. Long, S. Herrmann, and S. Chu. Atom interferometry with up to 24-photon-momentum-transfer beam splitters. *Phys. Rev. Lett.*, 100(18):180405, May 2008.
- [47] S. w. Chiow, T. Kovachy, H.-C. Chien, and M.A. Kasevich. *102hk* Large Area Atom Interferometers. *Phys. Rev. Lett.*, 107:130403, Sep 2011.
- [48] G.J. Dick. Local oscillator induced instabilities in trapped ion frequency standards. In *Proceedings of the 19th Annual Precise Time and Time Interval Applications and Planning Meeting*, pages 133–147, 2006.
- [49] D. Mueller, P. Schwindt, R. Grow, D.Z. Anderson, and E.A. Cornell. Guiding neutral atoms around curves with lithographically patterned current-carrying wires. *Phys. Rev. Lett.*, 83:5194, 1999.
- [50] Y. Shin, C. Sanner, G.-B. Jo, T.A. Pasquini, M. Saba, W. Ketterle, and D.E. Pritchard. Interference of Bose-Einstein condensates split with an atom chip. *Phys. Rev. A*, 72:021604, 2005.
- [51] Y.-J. Wang, D.Z. Anderson, V.M. Bright, E.A. Cornell, Q. Diot, T. Kishimoto, M. Prentiss, R.A. Saravanan, S.R. Segal, and S. Wu. An atom Michelson interferometer on a chip using a Bose-Einstein condensate. *Phys. Rev. Lett.*, 94:090405/1–4, 2005.
- [52] G.-B. Jo, Y. Shin, S. Will, T. A. Pasquini, M. Saba, W. Ketterle, D. E. Pritchard, M. Vengalattore, and M. Prentiss. Long phase coherence time and number squeezing of two Bose-Einstein condensates on an atom chip. *Phys. Rev. Lett.*, 98:030407, Jan 2007.

- [53] S. Wu, E. Su, and M. Prentiss. Demonstration of an area-enclosing guided-atom interferometer for rotation sensing. *Phys. Rev. Lett.*, 99:173201, 2007.
- [54] D.M. Farkas, K.M. Hudek, E.A. Salim, S.R. Segal, M.B. Squires, and D.Z. Anderson. A compact, transportable, microchip-based system for high repetition rate production of Bose-Einstein condensates. *Appl. Phys. Lett.*, 96(9):093102, 2010.
- [55] M. Fattori, C. D’Errico, G. Roati, M. Zaccanti, M. Jona-Lasinio, M. Modugno, M. Inguscio, and G. Modugno. Atom interferometry with a weakly interacting Bose-Einstein condensate. *Phys. Rev. Lett.*, 100:080405, Feb 2008.
- [56] J. Alnis, A. Matveev, N. Kolachevsky, Th. Udem, and T. W. Hänsch. Subhertz linewidth diode lasers by stabilization to vibrationally and thermally compensated ultralow-expansion glass Fabry-Pérot cavities. *Phys. Rev. A*, 77(5):053809, May 2008.
- [57] B. Young, M.A. Kasevich, and S. Chu. *Atom Interferometry*, chapter 9, pages 363–406. Academic Press, New York, 1997.
- [58] K. Moler, D.S. Weiss, M. Kasevich, and S. Chu. Theoretical analysis of velocity-selective Raman transitions. *Phys. Rev. A*, 45(1):342–348, Jan 1992.
- [59] M. Kasevich and S. Chu. Measurement of the gravitational acceleration of an atom with a light-pulse atom interferometer. *Appl. Phys. B*, 54:321–332, 1992.
- [60] Richard Stoner, David Butts, Joseph Kinast, and Brian Timmons. Analytical framework for dynamic light pulse atom interferometry at short interrogation times. *J. Opt. Soc. Am. B*, 28(10):2418–2429, Oct 2011.
- [61] L. Allen and J.H. Eberly. *Optical Resonance and Two-Level Atoms*. Dover Publications, New York, 1987.
- [62] David L. Butts, Joseph M. Kinast, Krish Kotru, Antonije M. Radojevic, Brian P. Timmons, and Richard E. Stoner. Coherent population trapping in Raman-pulse atom interferometry. *Phys. Rev. A*, 84:043613, Oct 2011.
- [63] Claude Cohen-Tannoudji, Bernard Diu, and Franck Laloë. *Quantum Mechanics*, volume 1, chapter 4. Wiley-VCH, Germany, 2005.

- [64] K. Bongs, R. Launay, and M.A. Kasevich. High-order inertial phase shifts for time-domain atom interferometers. *Appl. Phys. B*, 84:599–602, 2006.
- [65] A. Gauguet, T. E. Mehlstäubler, T. Lévèque, J. Le Gouët, W. Chaibi, B. Canuel, A. Clairon, F. Pereira Dos Santos, and A. Landragin. Off-resonant Raman transition impact in an atom interferometer. *Phys. Rev. A*, 78(4):043615, Oct 2008.
- [66] Richard P. Feynman and Albert R. Hibbs. *Quantum Mechanics and Path Integrals*. Dover Publications, New York, 2010.
- [67] Pippa Storey and Claude Cohen-Tannoudji. The Feynman path integral approach to atomic interferometry. A tutorial. *J. Phys. II France*, 4(11):1999–2027, 1994.
- [68] J. M. Hogan, D. M. S. Johnson, and M. A. Kasevich. Light-pulse atom interferometry. In E. Arimondo, W. Ertmer, W. P. Schleich, & E. M. Rasel, editor, *Atom Optics and Space Physics, Proc. of the International School of Physics “Enrico Fermi”*, page 411, 2009.
- [69] Charles Antoine. Rotating matter-wave beam splitters and consequences for atom gyrometers. *Phys. Rev. A*, 76:033609, Sep 2007.
- [70] Charles Antoine. Matter wave beam splitters in gravito-inertial and trapping potentials: generalized ttt scheme for atom interferometry. *Appl. Phys. B*, 84:585–597, 2006.
- [71] Janez Šetina. Private communication, 2011.
- [72] Ken Takase, John K. Stockton, and Mark A. Kasevich. High-power pulsed-current-mode operation of an overdriven tapered amplifier. *Opt. Lett.*, 32(17):2617–2619, Sep 2007.
- [73] M. Kasevich. *Atom Interferometry in an Atomic Fountain*. PhD thesis, Stanford University, 1992.
- [74] I. Dotsenko, W. Alt, S. Kuhr, D. Schrader, M. Müller, Y. Miroshnychenko, V. Gomer, A. Rauschenbeutel, and D. Meschede. Application of electro-optically generated light fields for Raman spectroscopy of trapped cesium atoms. *Applied Physics B: Lasers and Optics*, 78:711–717.

- [75] David L. Butts, Joseph M. Kinast, Brian P. Timmons, and Richard E. Stoner. Light pulse atom interferometry at short interrogation times. *J. Opt. Soc. Am. B*, 28(3):416–421, Mar 2011.
- [76] G. W. Biedermann, X. Wu, L. Deslauriers, K. Takase, and M. A. Kasevich. Low-noise simultaneous fluorescence detection of two atomic states. *Opt. Lett.*, 34(3):347–349, Feb 2009.
- [77] P. Bouyer, T. L. Gustavson, K. G. Haritos, and M. A. Kasevich. Microwave signal generation with optical injection locking. *Opt. Lett.*, 21(18):1502–1504, Sep 1996.
- [78] P. Cheinet, B. Canuel, F. Pereira Dos Santos, A. Gauguier, F. Yver-Leduc, and A. Landragin. Measurement of the sensitivity function in a time-domain atomic interferometer. *IEEE Trans. on Instrum. and Meas.*, 57(6):1141–1148, 2008.
- [79] E.L. Hahn. Spin echoes. *Phys. Rev.*, 80:580–594, 1950.
- [80] Holly K. Cummins, Gavin Llewellyn, and Jonathan A. Jones. Tackling systematic errors in quantum logic gates with composite rotations. *Phys. Rev. A*, 67(4):042308, Apr 2003.
- [81] L. M. K. Vandersypen and I. L. Chuang. NMR techniques for quantum control and computation. *Rev. Mod. Phys.*, 76(4):1037–1069, Jan 2005.
- [82] Worawarong Rakreungdet, Jae Hoon Lee, Kim Fook Lee, Brian E. Mischuck, Enrique Montano, and Poul S. Jessen. Accurate microwave control and real-time diagnostics of neutral-atom qubits. *Phys. Rev. A*, 79(2):022316, Feb 2009.
- [83] Sheng-wei Chiow, Sven Herrmann, Steven Chu, and Holger Müller. Noise-immune conjugate large-area atom interferometers. *Phys. Rev. Lett.*, 103(5):050402, Jul 2009.
- [84] P. Cladé, S. Guellati-Khélifa, F. Nez, and F. Biraben. Large momentum beam splitter using Bloch oscillations. *Phys. Rev. Lett.*, 102(24):240402, Jun 2009.
- [85] Malcolm H. Levitt and Ray Freeman. NMR population inversion using a composite pulse. *Journal of Magnetic Resonance*, 33(2):473–476, 1979.

- [86] Ray Freeman, Stewart P. Kempell, and Malcolm H. Levitt. Radiofrequency pulse sequences which compensate their own imperfections. *Journal of Magnetic Resonance*, 38(3):453 – 479, 1980.
- [87] R. Tycko. Broadband population inversion. *Phys. Rev. Lett.*, 51:775–777, Aug 1983.
- [88] S. Guérin, V. Hakobyan, and H. R Jauslin. Optimal adiabatic passage by shaped pulses: Efficiency and robustness. *Phys. Rev. A*, 84:013423, Jul 2011.
- [89] Malcolm H. Levitt. Composite pulses. *Progress in Nuclear Magnetic Resonance Spectroscopy*, 18(2):61 – 122, 1986.
- [90] A. J. Shaka, James Keeler, Tom Frenkiel, and Ray Freeman. An improved sequence for broadband decoupling: WALTZ-16. *Journal of Magnetic Resonance*, 52(2):335 – 338, 1983.
- [91] A. J. Shaka, P. B. Barker, and R. Freeman. Experimental demonstration of wideband spin inversion. *Journal of Magnetic Resonance*, 67(3):580 – 584, 1986.
- [92] S. Wimperis. Broadband, narrowband, and passband composite pulses for use in advanced NMR experiments. *Journal of Magnetic Resonance, Series A*, 109(2):221 – 231, 1994.
- [93] A. J. Shaka, James Keeler, and Ray Freeman. Evaluation of a new broadband decoupling sequence: WALTZ-16. *Journal of Magnetic Resonance*, 53(2):313 – 340, 1983.
- [94] A J Shaka and Alexander Pines. Symmetric phase-alternating composite pulses. *Journal of Magnetic Resonance*, 71:495–503, 1987.
- [95] G. Alzetta, A. Gozzini, L. Moi, and G. Orriols. An experimental method for the observation of R.F. transitions and laser beat resonances in oriented Na vapour. *Il Nuovo Cimento*, 36B(1):5–20, 1976.
- [96] E. Arimondo and G. Orriols. Nonabsorbing atomic coherences by coherent two-photon transitions in a three-level optical pumping. *Lettere al Nuovo Cimento*, 17(10):333–338, 1976.

- [97] H.R. Gray, R.M. Whitley, and Jr. C.R. Stroud. Coherent trapping of atomic populations. *Opt. Lett.*, 3(6):218–220, 1978.
- [98] J. Kitching, S. Knappe, M. Vukicevic, L. Hollberg, R. Wynands, and W. Weidmann. A microwave frequency reference based on VCSEL-driven dark line resonances in Cs vapor. *IEEE Trans. on Instrum. and Meas.*, 49(6):1313–1317, 2000.
- [99] Marlan O. Scully and Michael Fleischhauer. High-sensitivity magnetometer based on index-enhanced media. *Phys. Rev. Lett.*, 69(9):1360–1363, Aug 1992.
- [100] E. Arimondo. Coherent Population Trapping in Laser Spectroscopy. In E. Wolf, editor, *Progress in Optics*, volume 35, pages 257 – 354. Elsevier, 1996.
- [101] R. Loudon. *The Quantum Theory of Light*. Oxford Science Publications, New York, 1990.
- [102] D.S. Weiss, B.C. Young, and S. Chu. Precision measurement of \hbar/m_{Cs} based on photon recoil using laser-cooled atoms and atomic interferometry. *Appl. Phys. B*, 59:217–256, 1994.
- [103] H. J. McGuinness, A. V. Rakholia, and G. W. Biedermann. High data-rate atom interferometer for measuring acceleration. *ArXiv e-prints*, September 2011. 1109.4610, quant-ph.
- [104] O. Carraz, F. Lienhart, R. Charrire, M. Cadoret, N. Zahzam, Y. Bidet, and A. Bresson. Compact and robust laser system for onboard atom interferometry. *Appl. Phys. B*, 97:405–411, 2009.
- [105] Daniel A. Steck. Cesium D Line Data, Dec. 2010. Available online at <http://steck.us/alkalidata> (Rev. 2.1.4).